THÈSE

En vue de l'obtention du

DOCTORAT DE L'UNIVERSITÉ DE TOULOUSE

Délivré par *l'Université Toulouse III - Paul Sabatier*
Discipline ou spécialité : *NanoPhysique*

Présentée et soutenue par *Abdul Waheed Anwar*
Le *27 Janvier 2011*

Titre : *Investigation of doping and photoexcitation in carbon nanotubes using Raman spectroscopy*


JURY

Pr. Gérard MARIN (IPREM - Université de Pau)	*Rapporteur*
Pr. Philippe DEMONT(CIRIMAT – UPS Toulouse)	*Examinateur*
Pr. Andrei SAPELKIN (Physics Department - QMUL UK)	*Examinateur*
Pr. Wolfgang BACSA (UPS et CEMES Toulouse)	*Directeur de thèse*

Ecole doctorale : *Ecole Doctorale Sciences de la Matière, Toulouse*
Unité de recherche : *Centre d'Elaboration de Matériaux et d'Etudes Structurales*
Directeur(s) de Thèse : *M. Wolfgang BACSA(UPS et CEMES) & M. Pascal PUECH(UPS et CEMES)*
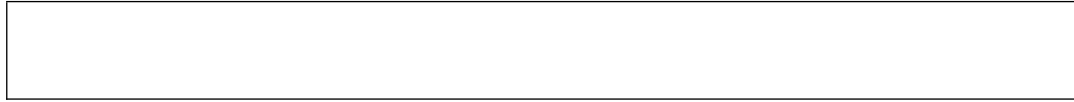
Dedication

Dedicated to my daughter AYESHA.......

Acknowledgment

I am really grateful to my thesis director Prof. Wolfgang Bacsa and co-director Dr. Pascal Puech for their full support, guidance, encouragement and sincerity which help me all the way to complete my PhD work. Both Wolfgang Bacsa and Pascal Puech guided me in understanding the carbon nanotubes and Raman spectroscopy right from the first day when I joined the PhD programme. I always enjoyed their suggestions and advices which helped me to understand and resolve the challenges in my research work.

My sincere thanks go to the carbon group incharge, Pr. Marc Monthioux, who has been the source of inspiration for me. I am thankful to the director of CEMES, Pr. Jean-Pierre Launay, and all the members of his secretariat, for providing me the chance to join the CEMES for my PhD and helping me in administrative procedures to complete my thesis.

I am also thankful to Dr. Andrei Sapelkin from the Queen Mary University of London for performing high pressure Raman experiments and sharing time from his very busy schedule. I feel my pleasure to show my gratitude to Dr. Ahmad Jawad Ghandour for his support and scientific discussions during my stay in London.

I would also like to acknowledge Dr. Jacques Teddy from group of Prof. Philip SERP (Laboratoire de Chimie de Coordination Toulouse) for providing the nitrogen doped carbon nanotubes samples and information about their synthesis, TEM analysis, XPS results and elemental analysis.

I feel pleasantly thankful to Dr. Revathi Bacsa for her caring attitude, moral support and useful suggestions. Many thanks to Antoine Zwick , Frédérique Neumayer and Sebastien Moyano for providing technical support for Raman experiments in CEMES. I am obliged to my colleagues of carbon group Mourad Berd, Jun Shen, Victoria Tishkova Leoni, Pierre-Ivan Reynal, Laure Noé, Math-

ieu Delmas and David Neumeyer. Thanks to all fellows of the laboratory for the good times in CEMES

It will not be possible for me to accomplish this work without the full support from my family and parents. My wife Henna and daughter Ayesha in Pakistan endured my absence from home with great patience during my studies and researches in France for long long four years from 2006 to 2010. I owe my thanks to my parents, sisters, brother and my friends for their support and prayers.

Finally, I am really grateful to Higher Education Commission (HEC) of Pakistan for the scholarship for financial support. I give full credit to the former chairman of HEC, Prof. Dr. Atta-ur-Rahman who started the foreign scholarship programme for Pakistani students.

Toulouse, Abdul Waheed Anwar

Abstract

This work explores photoexcitation, doping and bundling of carbon nanotubes using Raman spectroscopy. The electronic density of states of quasi-one dimensional carbon nanotubes contains a series of van Hove singularities. These van Hove singularities are the cause of strong optical transitions in the visible spectral range. Resonant excitation leads to strong absorption and efficient heating. The properties of carbon nanotubes and carbon nanofibers are influenced by doping. Doping by charge transfer or by substitution modifies the Fermi level and consequently influences the electronic responses. Raman spectroscopy is a non-invasive characterization technique suitable for the study of carbon nanotubes and is used to study phonons in doped carbon nanotubes.

Differences in the spectral shift of the Raman D and G bands, corresponding to anharmonic effects, are observed when heating carbon nanotubes through intense photon irradiation and by varying the temperature in a thermostat. These spectral changes in D mode are attributed to modifications of the defect induced double resonance Raman process due to the variation of the electronic band structure by excitons creation. It is found that the Raman intensity for double wall carbon nanotubes increases superlinearly in the red spectral region and sublinearly in the ultra violet spectral region and is suggested due to excitons involvement.

The investigation of the influence of doping and photoexcitation on the Raman G and D band on different types of carbon nanotubes and nanofibers show that Raman spectroscopy can be used to differentiate doping and can be used as a diagnostic tool. It is found that the number of defects which broaden the spectral bands limit spectral interpretation. A clear influence on the electronic states has been observed when doping or photo exciting carbon nanotubes. The parameters of D and G spectral bands were used to correlate

with nitrogen doping. The spectral bands broaden and up shifts for nitrogen doped multi walled carbon nanotubes (MWCNT). Doping with sulphuric acid upshifts the G mode frequency. The up shift for sulphuric acid doped double wall carbon nanotubes (DWCNT) synthesized from catalytic chemical vapor deposition method (CCVD) is attributed to charge transfer and strain in the lattice. The G band frequency also increases with higher hydrostatic pressure. We have combined sulphuric acid doping and high pressure Raman spectroscopy to investigate the properties of DWCNT synthesized from CCVD and obtained from transformation of peapods. The outer pressure coefficient for peapod transformed DWCNT is larger as compared to DWCNT using the CCVD method. The DWCNT doped with different concentrations of sulphuric acid are explored under high pressure suggesting an effect of the molecular ordering around carbon nanotubes at higher acid concentrations.

Raman spectra of individual double wall carbon nanotubes on silica show a splitting of the G band due to contributions of the inner and outer tube when using a excitation energy in resonance with the inner metallic tube and outer semiconducting tube. The spectral splitting indicates strong coupling while a previous report (Nanoletters 8, 3879, 2008) shows uncoupled inner and outer tubes. The spectral line widths are comparable to what has been observed for individual single wall carbon nanotubes (SWCNT) or graphene. The spectral position of the inner tube is consistent with previous extrapolations from measurements under high pressure and on chemically doped double wall tubes. Bundling of DWCNT leads to heterogeneous increase of the G band line width. Increased laser power shifts the G band of the outer tube to higher energies and modifies its line shape.

Résumé

Ce travail porte sur la photoexcitation, le dopage et l'agglomération des nanotubes de carbone en utilisant la spectroscopie Raman. La densité d'états électroniques des nanotubes de carbone, qui sont des structures quasi-unidimensionnelles, contient une série de singularités dites de van Hove. Ces singularités de van Hove sont la cause de transitions optiques fortes dans le domaine spectral visible. L'excitation résonante conduit à une absorption forte et un échauffement important. Les propriétés des nanotubes des carbone et des nanofibres des carbone sont influencés par le dopage. Le dopage par transfert de charge ou par substitution modifie le niveau de Fermi et change donc la réponse électronique. La spectroscopie Raman est une technique de caractérisation non destructive appropriée pour l'étude des nanotubes de carbone et est utilisée pour étudier les phonons dans les nanotubes de carbone dopés.

Des différences dans le décalage spectral des bandes Raman D et G, correspondant aux effets anharmoniques, sont observées lors d'un chauffage des nanotubes de carbone par irradiation photonique intense ou en faisant varier la température d'un thermostat. Les modifications spectrales du mode D sont attribués à des modifications du processus de double résonance Raman en raison de la variation de la structure de bande électronique provoquée par la création des excitons. Il se trouve que l'intensité Raman pour les nanotubes des carbone double parois augmente super linéairement pour une excitation dans le rouge et sous linéairement pour une excitation dans l'ultraviolet à cause de la participation des excitons.

Les paramètres des bandes spectrales D et G ont été utilisées pour déterminer le dopage à l'azote. Les bandes spectrales s'élargissent et se décalent vers les hautes fréquences pour les nanotubes de carbone multiparois dopé à l'azote (MWCNT). Le dopage à l'acide sulfurique induit une augmentation de la fréque-

nce du mode G. Le changement pour l'acide sulfurique dopé des nanotubes de carbone double parois (DWCNT) synthétisé à partir de la méthode de dépôt chimique en phase vapeur catalytique (CCVD) est attribuée à transfert de charge et la déformation dans le réseau. La bande G augmente aussi avec la haute pression hydrostatique. Nous avons combiné le dopage acide sulfurique et de haute pression hydrostatique observés par spectroscopie Raman pour étudier les propriétés des DWCNT synthétisés à partir de la méthode de dépôt chimique catalytique en phase vapeur et ceux obtenus par la transformation des peapods. Le coefficient de pression du tube extérieur pour les DWCNT transformés par Peapods est plus grand que pour leur homologues provenant de la méthode CCVD. Les DWCNT dopés avec différentes concentrations d'acide sulfurique ont été testés sous haute pression hydrostatique suggérant l'effet de l'ordre des molécules autour des nanotubes de carbone à des concentrations élevées.

Les spectres Raman de DWCNT individuel sur silice montre un dédoublement de la bande G en raison de contributions du tube interne et du tube externe pour une énergie d'excitation en résonance avec le tube métallique interne et externe semi-conducteurs tube. La séparation spectrale indique un couplage fort différent des observations précédentes (Nanoletters 8, 3879, 2008) qui montrent des tubes découplés. Les largeurs des raies spectrales sont comparables à ce qui a été observé pour un nanotube de carbone simple paroi ou du graphène. La position spectrale du tube interne est conforme aux précédentes extrapolations obtenues à partir des mesures sous haute pression et par dopage chimique. L'agglomération des DWCNT conduit à une augmentation hétérogène de la largeur de la bande G. Une augmentation de la puissance du laser déplace la bande G du tube extérieur à des énergies plus élevées et modifie sa forme de raie.
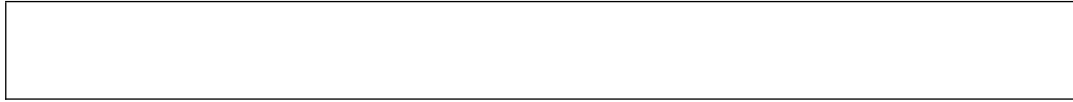
Contents

List of Tables

List of Figures

Carbon Nanotubes: Structure, Properties And Applications

1.1 Introduction

A great progress [1–3] has been made in synthesis, separation, purification and applications of carbon nanotubes since their discovery by Sumio Iijima in 1991 [4]. Nanotubes as one of the most studied material has played an effective role in nanotechnology revolution. One reason for continuous increase of interest is due to broad range of promising applications such as in electronics, renewable energy, medicine, display devices, quantum computing and composite materials [5]. Small in size, less power consumption, light weight and high performance gives the nanotubes based devices a leading edge to devices made of other materials [6]. Along with the attractive potential applications, nanotubes are also a test ground for basic science. Hand in hand comparing between experiment and theory is effectively used to understand their properties [7]. In this chapter we explain the basic theoretical background of carbon nanotubes and their properties. Different synthesis methods and applications of carbon nanotubes are briefly discussed.

1.2 Different Forms of Carbon

Carbon is a remarkable material showing a variety of stable forms such as graphite, diamond, carbon fibers, fullerene and carbon nanotubes. In general carbon materials can be divided into bulk carbon and nano structured carbon. Carbon materials are unique in many ways. Carbon has an atomic number 6 and its ground state electronic configuration is $1s^2$, $2s^2$, $2p^2$. The four valence

electrons can have several hybridizations. In carbon based materials, due to hybridization of valence orbitals, different electronic configurations are possible. The atomic orbitals of carbon can hybridize as sp^1, sp^2 or sp^3 to form molecular orbitals with carbon atoms or with atoms of different elements. It can exist as 0-D, 1-D, 2-D or 3-D as fullerenes, nanotubes, graphene, graphite or diamond respectively.

The three main allotropes of carbon are graphite, diamond, and amorphous carbon. All forms of carbon are highly stable and high temperature is required to react even with oxygen. There is large variation of physical properties for different allotropes of carbon. For example, graphite is a very good electrical conductor while undoped highly crystalline diamond is a insulator. Diamond is a very hard material, while graphite is very soft along the C axis.

Carbon nanostructures can be considered as composed structures of nanometer dimensions. The discovery of Buckminster fullerene C_{60} in 1985 by Kroto [8] has been an important step in finding new carbon nano structures. Fullerenes, carbon nanocones, carbon nanohorns, nanoscale carbon toroidal structures, helicoidal tubes, carbon nanotubes, carbon nanoparticles, graphene, porous carbons and carbon nanofibers are different types of nano structured carbon materials. All the carbon nano structures which have been discovered upto now are constructed from sp^2 bonded hexagonal graphene layers.

Among the carbon nanostructures, carbon nanotubes and graphene are the most popular nanomaterials [4, 9]. Single wall carbon nanotubes which are made of one atomic layer thick carbon hexagonal structures can be semiconducting or metallic depending on their diameter or chirality. Approximately one third of the tubes are metallic and two third are semiconducting considering all cases as equiprobable [10]. The unusual electronic properties of carbon nanotubes lead to new exciting 1-D physics. Semiconductor and metallic tubes perhaps could be joined to construct heterojunction. The properties of the heterojunction could be modified by introducing changes in the junction region [11]. The elastic properties, their very high modulus values are of great interest [12]. The different techniques for the synthesis of carbon nanotubes are pulsed laser vaporization, arc discharge and chemical vapor deposition.

1.2.1   Graphite and graphene

The graphite crystal structure consist of honeycomb lattice of carbon atoms as shown in figure 1.1. The planes of carbon are stacked in an ABAB sequence. A and B atomic sites on adjacent layers are on top of one another while the A' and B' atomic sites in one plane are over the unoccupied centers of the consecutive

layers. Carbon atoms are sp^2 hybridized in the honeycomb lattice. Three strong in-plane bonds are formed by carbon atoms with its nearest neighbors with 2s, $2p_x$ and $2p_y$ orbitals [13]. The distance between two neighboring carbon atoms(a_{c-c}) in the plane is 0.142 nm. The in-plane lattice constant(a_0) is 0.246 nm and interplanar distance is 0.334 nm.
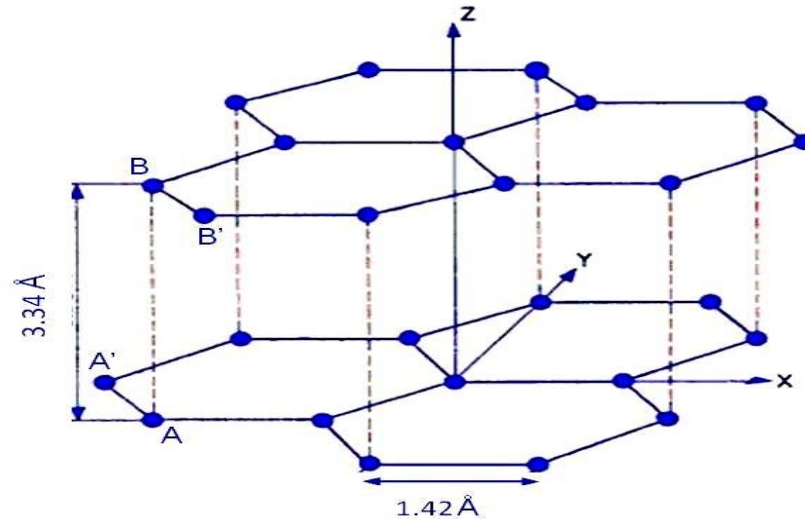
Figure 1.1: *Structure of graphite. The planes of carbon are stacked in an ABAB sequence. The distance between two neighboring carbon atoms (a_{c-c}) in plane is 0.142nm. The interplanar distance is 0.334 nm [14].*

Disorder tends to have a small effect on the in-plane lattice constant. This is mainly due to strong in-plane C-C bond. However disorder affects interplanar distance because of weak interplanar interactions. In-plane substitution is difficult due to the strong in-plane bonds and consequently impurities are found preferentially in interstitial sites between the planes. Weak disorder produces faults in ABAB stacking and the interlayer distance increases due to faults in ABAB stacking order. The upper limiting value of interplanar distance is 0.344 nm after which the graphene layers in graphite becomes uncorrelated resulting in independent two dimensional honeycomb structures.

This uncorrelated graphene layer structure is called turbostratic graphite. The turbostratic graphite behaves as zero gap semiconductor. With the decrease of interplanar correlation, the Brillouin zone of graphite is changed to a Brillouin zone of 2-D graphene sheet [13].

Graphite can also be prepared synthetically. Twinning planes and screw dislocations defects along with chemical impurities like iron and other transition metals are common in natural graphite. Synthetic graphite examples are Kish graphite (single crystal graphite) and highly ordered pyrolytic graphite

(HOPG). Kish graphite is synthesized on the surface of large carbon content iron melts and separated as crystal from these solutions. The size of Kish graphite flakes is generally large compared to natural flakes of graphite. The HOPG is made by pyrolysis of hydrocarbons at temperature higher then 2000 °C and then further heated at higher temperatures. The structural order and C axis alignment of HOPG can be changed by varying the processing parameters like residence time at high temperature treatment, heat treatment temperature and stress applied in the course of the heat treatment [13].
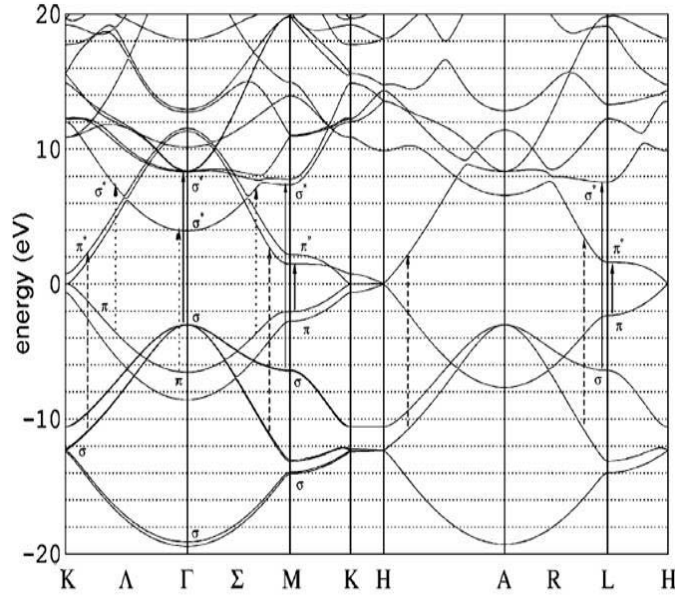
Figure 1.2: *Kohn-Sham band structure of graphite along high-symmetry directions in the Brillouin zone. Arrows denote interband transitions. The Fermi energy, E_F, is taken as the reference energy. $\Gamma K = 1.70 \mathring{A}^{-1}$ and $\Gamma M = 1.47 \mathring{A}^{-1}$. Symmetry points A, L, and H define the plane which is parallel to G-M-K and passes from the zone edge. Therefore the KH segment is parallel to the c axis [15].*

Graphene is a flat sheet of sp^2 bonded carbon atoms in the form of a two dimensional honeycomb crystal lattice of one atom thickness. Graphene is an isolated atomic plane of graphite. Graphene is a basic building block for graphitic materials of all dimensions. It can be modified into 0-D fullerenes, rolled into 1-D nanotubes or stacked into 3-D graphite. In graphene, the carbon-carbon bond length is 0.142 nm. Intrinsic graphene is a semi-metal or zero-gap semiconductor. The electron mobility at room temperature for graphene has very high values which are as high as 15000 cm^{2}V^{-1}s^{-1} [9, 16].

In 2004 physicists from University of Manchester and Institute for Microelectronics Technology, Russia, developed a method to isolate individual graphene

sheets. They used the Scotch tape for isolation of graphene plans by mechanical exfoliation [17]. They split the graphite crystals into thinner sheets by repeatedly using the Scotch tape. The tape with attached thin optically transparent flakes was dissolved in acetone to retrieve the monolayers on Si wafer. Individual monolayers were traced by using the optical microscope. This technique was simplified by avoiding the floating of graphene in solution. This is known as Scotch tape or drawing method. The flakes present on a suitable substrate like a Si wafer can be visually recognized by a noticeable optical contrast [18].
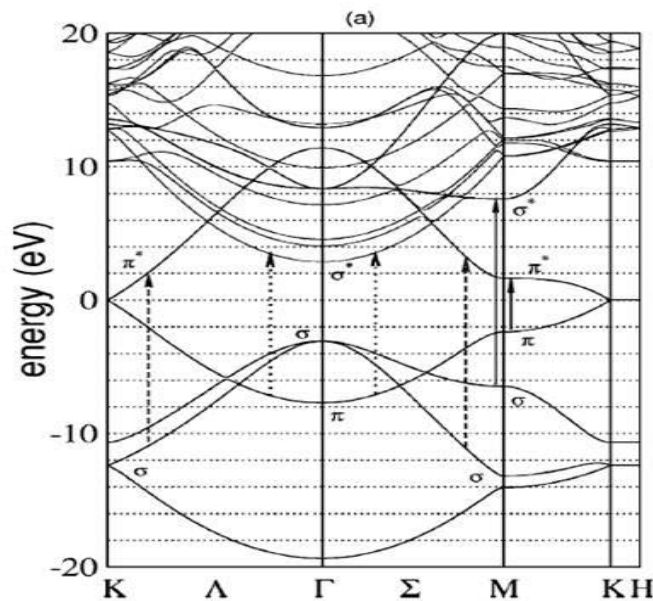
Figure 1.3: *Kohn-Sham band structure of graphene-sheet geometries with $2c/a_{(hex)}$ along high-symmetry directions in the Brillouin zone [15].*

Epitaxial growth is another way of graphene production. In this method, silicon carbide is heated to high temperature greater then 1100 °C, later it is reduced to graphene. Many important properties like electronic band structure were revealed by the graphene produced by SiC. Very large mobilities independent of temperature have been observed in SiC epitaxial graphene but still much lower than mobilities in suspended graphene produced by drawing method. The weak van der Waals forces are responsible for the coupling of layers in multilayered graphene stack. In some cases these forces do not affect the electronic properties of the individual graphene sheet in the stack but in some cases properties are affected and they behave as layers in graphite. Theoretically this effect is explained by the symmetry of interlayer interactions.

The figure 1.4 on left shows the honeycomb lattice of graphene. The graphene sheet consist of sp^2 hybridized carbon atoms in the form of honeycomb lattice.

The atoms arranged in plane have 120° angle in three bonding directions. The unit cell of graphene has two carbon atoms and is shown as shaded area in the left diagram of figure 1.4. The direct lattice vectors are $\vec{a}_1$ and $\vec{a}_2$. The right diagram shows the reciprocal lattice of graphene. The first Brillouin zone or the unit cell of reciprocal lattice is shaded and high symmetry points are labeled as K', K and M. The basis vectors of reciprocal lattice are $\vec{b}_1$ and $\vec{b}_2$. The reciprocal lattice vector is related with direct lattice vector as $\vec{a}_i.\vec{b}_j = 2\pi\delta_{ij}$ where $\delta_{ij} = 1$ if i=j and $\delta_{ij} = 0$ if i≠j.
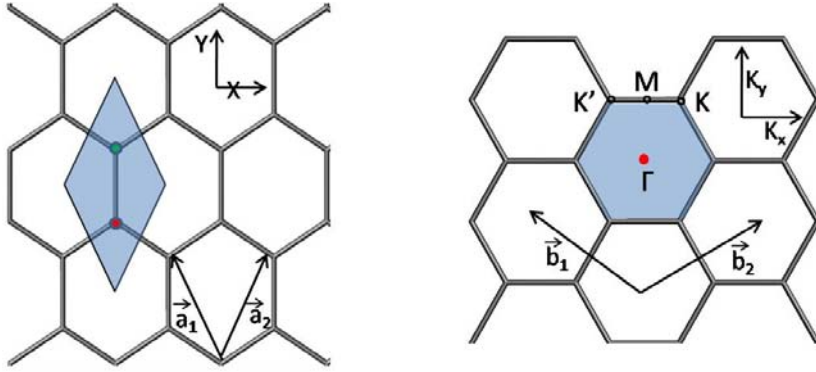
Figure 1.4: *The section of honeycomb graphene sheet. Left figure is for direct lattice. The shaded area represent the unit cell of graphene. The right figure is for reciprocal lattice of graphene. The shaded hexagon represent the first Brillouin zone. $\vec{b}_1$ and $\vec{b}_2$ are basis vectors for reciprocal lattice [19].*

$$\vec{a}_1 = -\frac{a_\circ}{2}\hat{x} + \frac{\sqrt{3}a_\circ}{2}\hat{y} \qquad \vec{a}_2 = \frac{a_\circ}{2}\hat{x} + \frac{\sqrt{3}a_\circ}{2}\hat{y} \qquad (1.1)$$

where $a_\circ = |\ \vec{a}_1\ | = |\ \vec{a}_2\ | = 1.42\sqrt{3} = 2.46$Å is the lattice constant for graphene unit cell.

$$\vec{b}_1 = -\frac{2\pi}{a_\circ}\hat{k}_x + \frac{2\pi}{a_\circ\sqrt{3}}\hat{k}_y \qquad \vec{b}_2 = \frac{2\pi}{a_\circ}\hat{k}_x + \frac{2\pi}{a_\circ\sqrt{3}}\hat{k}_y \qquad (1.2)$$

where b = $|\vec{b}_1| = |\vec{b}_2| = \frac{4\pi}{a_\circ\sqrt{3}}$ is the reciprocal lattice constant for graphene unit cell.

Γ is the point in reciprocal lattice where momentum state $(\vec{k}) = \vec{0}$. Point M is at the midpoint of boundary segment of first Brillouin zone. At point M, $\vec{k} = \frac{2\pi}{a_\circ\sqrt{3}}\hat{k}_y$. The value of $|\ \vec{k}\ |$ at the points K and K' is $\frac{4\pi}{3a_\circ}$. The figure 1.5 represent the energy dispersion of graphene near the Fermi level of first Brillouin zone.

The energy values of valence and conduction band are shown by the allowed energy values for corresponding $\vec{k}$. The valence and conduction band meet at the K and K' points of the first Brillouin zone. Out of four electrons of the valence band of carbon atom, three are sp^2 hybridized and one is unhybridized. As for two atoms per unit cell of graphene, the two unhybridized electrons go for π bonding perpendicular to the plan of graphene plane and available for conduction. These two electrons in the valence band makes the graphene a zero gap semiconductor.
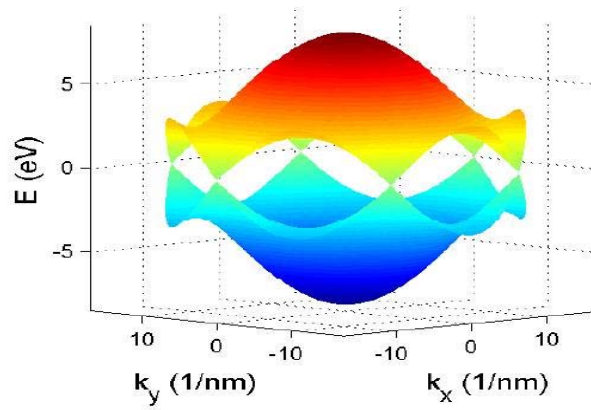
Figure 1.5: *Graphene band structure. The energy in eV is along vertical axis and $\hat{k}_x$ and $\hat{k}_y$. The values of energy is plotted for $\mid \vec{k} \mid < \frac{4\pi}{3a_\circ}$. The valence and conduction band meet at the K and K' points of the first Brillouin zone [19].*

The energy dispersion relation for graphene by tight binding with overlap integral equal to zero is given as [10]

$$E_{g2D}(k_x, k_y) = \pm t\sqrt{1 + 4\cos(\frac{k_x a_\circ}{2})\cos(\frac{k_y a_\circ \sqrt{3}}{2}) + 4cos^2(\frac{k_x a_\circ}{2})} \qquad (1.3)$$

In equation 1.3, t (-2.7eV) is the transfer integral between the carbon atoms [20]. In Brillouin zone at Γ point($\vec{k} = \vec{0}$), the separation between conduction and valence band is 6t. For M point($\vec{k} = \frac{2\pi}{a_\circ\sqrt{3}}\hat{k}_y$), the energy gap is by 2t. For K point, the value of $E_{g2D}(-\frac{2\pi}{3a_\circ}, \frac{2\pi}{a_\circ\sqrt{3}}) = 0$ showing that the conduction and valence band touch at K points. This makes the graphene a zero band gap semiconductor.

1.2.2 The Structure of Single Wall Carbon Nanotubes

The single wall carbon nanotube is a rolled seamless cylinder of a rectangular strip of monolayer graphene. The rectangular strip is shown in figure 1.6 as the shaded region. The carbon nanotube is formed when the shaded region is rolled into a cylinder.
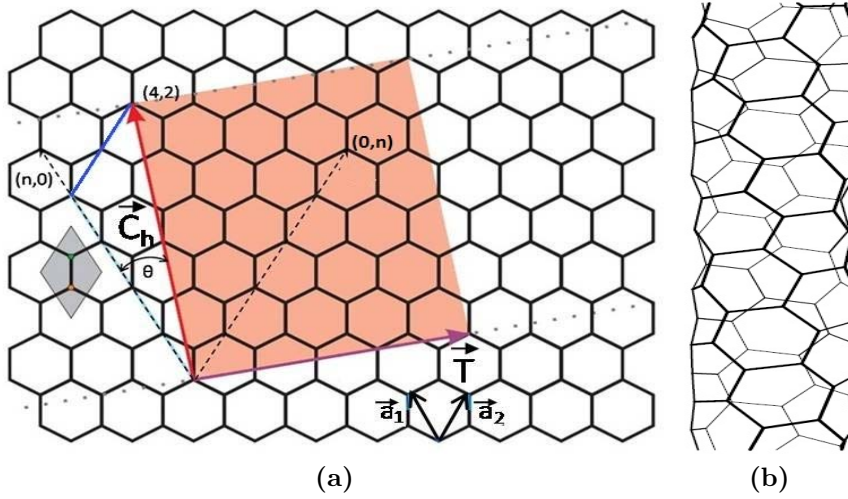
Figure 1.6: *(a)The honeycomb graphene sheet. Carbon nanotube is formed when the shaded region is rolled into a cylinder. The shaded region is defined by the chiral vector $\vec{C}_h$ and translation vector $\vec{T}$. The unit cell of carbon nanotube is defined by the shaded rectangle. (b)The (4,2) carbon nanotube created by rolling up a graphene sheet around the $4\vec{a}_1 + 2\vec{a}_2$ vector [19]*

The shaded region is defined by the chiral vector $\vec{C}_h$ and translation vector $\vec{T}$. The unit cell of carbon nanotube is defined by the shaded rectangle. $\vec{C}_h$ is called the chiral vector and is perpendicular to nanotube axis. The chiral vector $\vec{C}_h$ is obtained by the linear combination of the lattice vectors $\vec{a}_1$ and $\vec{a}_2$ [10].

$$\vec{C}_h = n_1\vec{a}_1 + n_2\vec{a}_2 \tag{1.4}$$

where $n_2 \leq n_1$

$$\mid \vec{C}_h \mid = a_\circ\sqrt{n_1^2 + n_2^2 + n_1 n_2} \tag{1.5}$$

In above equation n_1 and n_2 are integers and are called chiral indices (or Hamada indices). $\vec{T}$ vector is parallel to nanotube axis and perpendicular to $\vec{C}_h$ vector. $\vec{T}$ is the translation vector which connects the origin to the

first equivalent site on the honeycomb lattice. Unit cell of carbon nanotube is obtained by rolling the shaded rectangle formed by $\vec{C}_h$ and $\vec{T}$ on the graphene sheet. $\mid \vec{C}_h \mid$ becomes the circumference of the nanotube.

$$\vec{T} = t_1 \vec{a}_1 + t_2 \vec{a}_2 \qquad (1.6)$$

where t_1 and t_2 are integers and do not have common devisor other than unity (greatest common devisor (gcd)$(t_1, t_2) = 1$). The values of t_1 and t_2 can be find by the following equations

$$t_1 = \frac{2n_2 + n_1}{d_R} \qquad t_2 = -\frac{2n_1 + n_2}{d_R} \qquad (1.7)$$

Where $d_R = gcd(2n_2 + n_1, 2n_1 + n_2)$. The chiral angle θ is the angle between the basis vector $\vec{a}_1$ and chiral vector $\vec{C}_h$. The chiral angle is given as

$$\cos(\theta) = \frac{n_1 + 2n_2}{2\sqrt{n_1^2 + n_2^2 + n_1 n_2}} \qquad (1.8)$$

$$or \qquad \theta = \arctan\frac{\sqrt{3}n_1}{n_1 + 2n_2} \qquad (1.9)$$

Carbon in nanotubes and graphene are sp^2 bonded and so it is appropriate to compare the many physical and electronic properties of nanotubes with graphene [10]. The structure and electronic properties of carbon nanotube depends upon how the graphene sheet is rolled. The total number of hexagons in the unit cell of carbon nanotube N is given by

$$N = \frac{\mid \vec{C}_h \times \vec{T} \mid}{\mid \vec{a}_1 \times \vec{a}_2 \mid} \qquad (1.10)$$

where $\mid \vec{C}_h \times \vec{T} \mid$ determines the area of carbon nanotube unit cell and $\mid \vec{a}_1 \times \vec{a}_2 \mid$ is the area of one unit cell of graphene. Graphene has two carbon atom per unit cell. For N number of unit cells in graphene, the total number of carbon atoms in the unit cell of CNT is 2N. The three types of nanotubes defined by chiral indices and chiral angle are as (n$_1$,0) for zigzag($\theta = 0°$) , (n_1, n_1) for armchair($\theta = 30°$) and (n_1, n_2) with n$_1 \neq$ n$_2$ for chiral tubes($0° < \theta < 30°$). The diameter of the tube is calculated from the magnitude of chiral vector as

$$d_t = \frac{\mid \vec{C}_h \mid}{\pi} = \frac{a_\circ \sqrt{n_1^2 + n_2^2 + n_1 n_2}}{\pi} \qquad (1.11)$$

The rolling of 2-D graphene sheet into 1-D carbon nanotubes can change the zero band gap energy depending upon the chiral indices and chiral angle. Rolling of graphene sheet into cylindrical structures introduces additional quantization of the band structure of graphene. The cylindrical shape of graphene results in the phase accumulation as integral multiple of 2π for the electrons along the circumference. The two vectors resembling to $\vec{C}_h$ and $\vec{T}$ of graphene are $\vec{K}_\perp$ and $\vec{K}_\parallel$ respectively. The component of $\vec{k}$ along the $\vec{T}$, $\vec{K}_\parallel$ is along the nanotube axis. The component of $\vec{k}$ along the $\vec{C}_h$, $\vec{K}_\perp$ is perpendicular to the nanotube axis. The relation of $\vec{K}_\perp$ and $\vec{K}_\parallel$ with $\vec{C}_h$ and $\vec{T}$ can be represented as

$$\vec{K}_\perp.\vec{C}_h = 2\pi, \quad \vec{K}_\perp.\vec{T} = 0 \tag{1.12}$$

$$\vec{K}_\parallel.\vec{C}_h = 0, \quad \vec{K}_\parallel.\vec{T} = 2\pi \tag{1.13}$$

The above equations can be used to find the expressions for $\vec{K}_\perp$ and $\vec{K}_\parallel$.
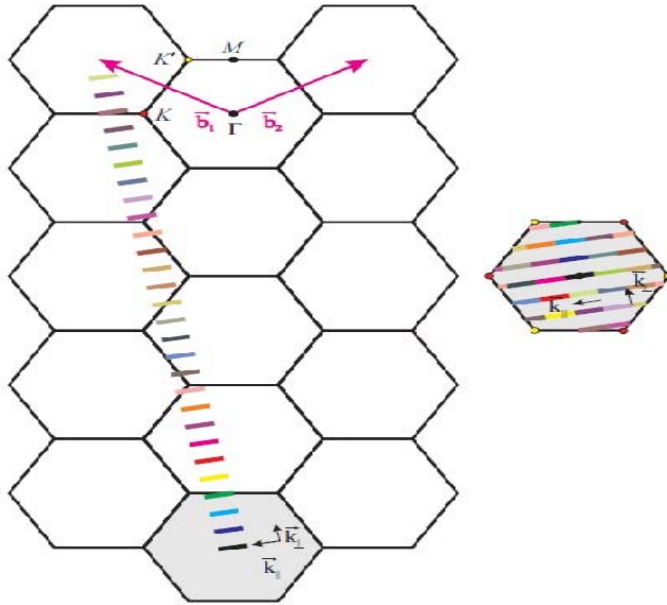
Figure 1.7: *The allowed $\vec{k}$ states for SWCNT(4,2) are shown as colored parallel lines. On the left figure the $\vec{b}_1$ and $\vec{b}_1$ are the reciprocal lattice vectors of graphene. The shaded region is the Brillouin zone of graphene. The 28 1-D Brillouin zones of CNT of of length $\mid \vec{K}_\parallel \mid$ spaced by $\mid \vec{K}_\perp \mid$ are shown as colored lines. Figure in the right shows that all the ID Brillouin zones are translated into graphene Brillouin zone [19].*

$$\vec{K}_\perp = \frac{1}{2}\left(\frac{a_\circ}{\pi d_t}\right)^2 \left[(2n_1 + n_2)\vec{b}_1 + (2n_2 + n_1)\vec{b}_2\right] \tag{1.14}$$

$$\vec{K}_\parallel = \frac{1}{N}(n_2\vec{b}_1 - n_1\vec{b}_2) \tag{1.15}$$

The magnitudes of vectors $\vec{K}_\perp$ and $\vec{K}_\parallel$ are given as

$$\mid \vec{K}_\perp \mid = \frac{2\pi}{\mid \vec{C}_h \mid} \tag{1.16}$$

$$\mid \vec{K}_\parallel \mid = \frac{2\pi}{\mid \vec{T} \mid} \tag{1.17}$$

The two vectors $\vec{K}_\perp$ and $\vec{K}_\parallel$ define the reciprocal unit cell of carbon nanotube in 2-D. The electron wave vector $\vec{k}$ can be expressed as $\vec{k} = p\vec{K}_\perp + q\vec{K}_\parallel$. As the electron wave function along the circumference must be multiple of 2π with $\vec{K}_\perp.\vec{C}_h = 2\pi$ so p must be an integer value. For every value of p there will be 1-D Brillouin zone having length $\mid \vec{K}_\parallel \mid$ parallel to nanotube axis. Figure 1.7 represents the Brillouin zones of carbon nanotube of chiral indices(4,2). The length of all the parallel lines representing the Brillouin zones of carbon nanotubes is $\frac{2\pi}{|\vec{T}|}$ and the width is $\mid \vec{K}_\perp \mid$. The hexagon at the bottom center on left figure is the Brillouin zone of graphene. Single wall carbon nanotubes can be classified as metallic or semiconductors depending upon how the electrons allowed $\vec{k}$ states interact with graphene band structure. If the Brillouin zones of carbon nanotubes intersect the K and K' points of graphene Brillouin zone then the tubes are metallic having zero band gap. If quantized Brillouin zones of tube do not intersect the K and K' points of graphene Brillouin zone then the tubes are semiconductors having non zero band gap.

The allowed energies for carbon nanotubes are the intersection of $\vec{k}$ states of tubes with graphene band. This intersection is like a cone intersected by a plane giving conic section of allowed states. For semiconducting tubes, the conic section is of hyperbola type and the allowed $\vec{k}$ states do not cross the Dirac points of graphene. For the metallic tubes the allowed $\vec{k}$ states passes through the points of the cone and so the degeneracy of two intersecting lines.

The 1-D energy dispersion relation is given as

$$E_\mu(k) = E_{g2D}\left(k\frac{K_\parallel}{|K_\parallel|} + \mu K_\perp\right) \tag{1.18}$$

where μ = 0,........,N-1 and $-\frac{\pi}{T} < k < \frac{\pi}{T}$.

The energy dispersion relation for armchair (n_1,n_1) SWCNT can be calculated by applying the periodic boundary condition in the circumferential direction

$$n_1\sqrt{3}k_{y,q} = 2\pi q \qquad (1.19)$$

where q = 1,.....,$2n_1$. Replacing the value of $k_{y,q}$ from equation (1.19) in equation (1.3) gives the energy dispersion relation for armchair carbon nanotubes

$$E^a(k) = \pm t\sqrt{1 + 4\cos(\frac{ka_\circ}{2})\cos(\frac{q\pi}{n_1}) + 4cos^2(\frac{ka_\circ}{2})} \qquad (1.20)$$

with $(-\pi < ka_\circ < \pi)$ and q = 1,.....,$2n_1$.

The energy dispersion relation for zigzag $(n_1,0)$ SWCNT can be calculated by applying the periodic boundary condition in the circumferential direction

$$n_1 k_{x,q} = 2\pi q \qquad (1.21)$$

where q = 1,.....,$2n_1$. Replacing the value of $k_{x,q}$ from equation (1.21) in equation (1.3) gives the energy dispersion relation for armchair carbon nanotubes

$$E^z(k) = \pm t\sqrt{1 + 4\cos(\frac{ka_\circ\sqrt{3}}{2})\cos(\frac{q\pi}{n_1}) + 4cos^2(\frac{ka_\circ}{2})} \qquad (1.22)$$

with $(\frac{-\pi}{\sqrt{3}} < ka_\circ < \frac{\pi}{\sqrt{3}})$ and q = 1,.....,$2n_1$.

The band gap energy of the semiconducting tubes are inversely proportional to diameter of the tubes. The band gap of semiconducting tubes can be calculated by [10, 21]

$$E_{11}^{SC} = \frac{2ta_{C-C}}{d_t} \qquad (1.23)$$

or

$$E_{11}^{SC} = \frac{0.78}{d_t} \qquad (1.24)$$

Where a_{C-C} = 0.144 nm is the nearest neighbor distance between two carbon atoms, d_t is the diameter of the tube and t ($\approx$ -2.7 eV) is the transfer integral obtained by the tight binding calculations.

The electrical properties of carbon nanotubes are defined by the density of states (DOS). The density of states refers to the number of quantum states per unit energy. The density of states indicates how densely packed quantum states in a particular system. The the density of states can be determined by energy values as a function of wave vector. The density of states is calculated

by knowing the total number of available states for a period of energy values with the limit of change in energy reaches to zero. Density of states at energy E for one dimensional system is given as

$$n(E) = \frac{2}{q|k_\parallel|} \sum_i \int \mathrm{d}k_\parallel \delta(k_\parallel - k_i) \left| \frac{\partial E^\pm(k_\perp, k_\parallel)}{\partial k_\parallel} \right|^{-1} \tag{1.25}$$

where k_i is given by $E - E^\pm(k_\perp, k_\parallel) = 0$ and $q|k_\parallel| = 4\pi^2 d/\sqrt{3}a_\circ^2$ is the total Brillouin zone area of nanotube. The inverse partial derivative is given as

$$\left| \frac{\partial E^\pm(k_\perp, k_\parallel)}{\partial k_\parallel} \right|^{-1} = \frac{\sqrt{3}}{2} a_\circ t \frac{|E^\pm|}{\sqrt{(E^\pm)^2 - E_v^2}} \tag{1.26}$$

where $\gamma_\circ$ is called is the C-C interaction energy constant(tight binding integral).

$$n(E) = \frac{4a_\circ}{\pi^2 dt} \sum_{v=-\infty}^{\infty} \frac{|E^\pm|}{\sqrt{(E^\pm)^2 - E_v^2}} \tag{1.27}$$

The density of states can be derived by $\left| \frac{\partial E^\pm(k_\perp, k_\parallel)}{\partial k_\parallel} \right|^{-1}$. This shows that when $\left| \frac{\partial E^\pm(k_\perp, k_\parallel)}{\partial k_\parallel} \right|$ will be minimum, the DOS will be maximum and reaches to infinity for $\left| \frac{\partial E^\pm(k_\perp, k_\parallel)}{\partial k_\parallel} \right| = 0$. In figure 1.8, the band structure of semiconducting and metallic SWCNT are shown on the left side and corresponding densities of states are shown on the right part of the figure. For semiconducting CNT, the DOS is zero as no allowed values of energies exist near the Fermi level and reaches to very high value at the minimum value of conduction band and at the maximum value of valence band across the band gap. For metallic CNT, the density of states is constant close to the Fermi level as $\left| \frac{\partial E^\pm(k_\perp, k_\parallel)}{\partial k_\parallel} \right| = constant$ near the Fermi level.
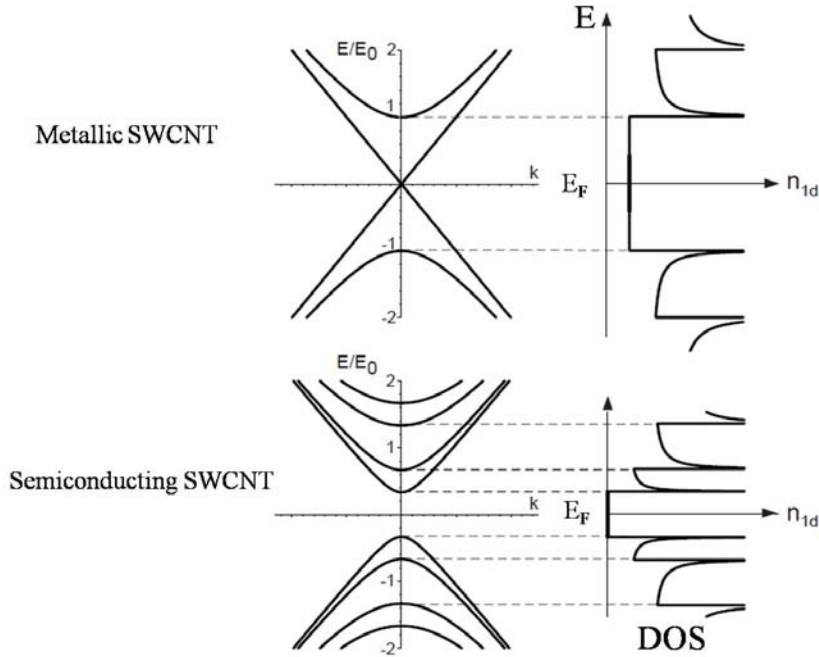
Figure 1.8: *Approximate one-dimensional band structure of carbon nanotubes (left) and corresponding density-of-states (right). There are two kind of nanotubes: metallic and semiconducting. A tube is metallic, if (m-n) ∈ 3**Z**. The band gap E_g of a semiconducting tube is inversely proportional to the diameter and equal to $E_g = 2E_0/3$, where $E_0 = 2\hbar v_F/d$ [22].*

The optical properties of single wall carbon nanotubes depend upon the allowed electronic transitions between van Hove singularities (vHs) in the density of states. The van Hove singularities (vHs) arose from the one dimensional (1-D) structure of SWCNT. The transition energies E_{ii} can be represented as E_{11}^{SC}, E_{22}^{SC}, E_{11}^{M} where superscript SC is for semiconducting, M is for metallic SWCNT and index i indicates the vHs in the valence and conduction bands above and below the Fermi level.

The transition energies can be calculated by joint density of states(JDOS). The figure 1.9 shows the JDOS for semiconducting and metallic SWCNT.

$$JDOS = \frac{2}{q|k_\parallel|} \sum_i \int dk_\parallel \delta(k_\parallel - k_i) \left| \frac{\partial(E^- - E^+)}{\partial k_\parallel} \right|^{-1} \qquad (1.28)$$

with E^- and E^+ associated to same quantum number.
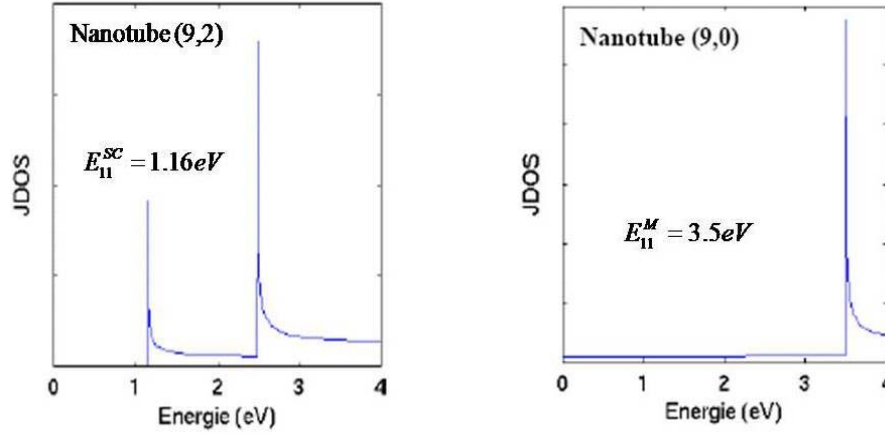
Figure 1.9: *The joint density of states (JDOS) as a function of energy of semiconducting (9,2) and metallic nanotube (9,0) [23]*

Metallic carbon nanotubes shows finite density of states at Fermi level while semiconducting tubes have finite density of states starting from $\frac{E_{gap}}{2}$ above and below the Fermi level. The conductance (G) of the 1-D conductor [24, 25] is given as

$$G = \frac{e^2}{h} \sum_i T_i(E_F) \tag{1.29}$$

where $T_i(E_F)$ is the transmission probability in the ith channel and $\frac{e^2}{h} (\cong 39\mu S)$ is a quantum of conductance. Each band is degenerate and for each channel two opposite spin electrons are allowed. The maximum theoretical conductance for small length metallic single wall carbon nanotubes has been calculated is $\frac{4e^2}{h} (\cong 155\mu S)$ [26, 27].

SWCNT are of two types, chiral tubes and achiral tubes. Chiral nanotubes have spiral symmetry and the mirror image does not fall on itself where as for achiral tubes, the mirror image falls on itself [28–32]. The achiral tubes are further divided into two categories, armchair and zigzag. The rolling of graphene sheet changes the physical and electronic properties of graphene layer. Different ways of wrapping gives different electronic properties. The electron wave functions changes with folding of the graphene plane into cylinders. The tube wrapping depends on the periodic boundary conditions and influences the electron propagation. This makes the SWCNT either semiconducting or metallic due to band gap variation from 0 eV to about 2 eV.

The optical response of carbon nanotubes is high due to the one dimensional confinement of electronic structure having van Hove singularities [33]. The optical response in all optical spectroscopies can be represented by Kataura plot [34] as shown in figure 1.10. The points in Kataura plot represents the transition energies as a function of nanotube diameter. Each point is for one particular

SWCNT having chiral indices (n_1, n_2). Grey lines are a guide to the eyes for a group of SWCNT with $2n_1+n_2$=constant. Open, filled, and dotted circles stand for E_{ii} for semiconducting type 1 $[(2n_1 + n_2)\text{mod}3 = 1]$, type 2 $[(2n_1 + n_2)\text{mod}3 = 2]$ and metallic SWCNT $[(2n_1 + n_2)\text{mod}3 = 0]$ respectively) [35]. The E_{11}^{SC} and E_{22}^{SC} are for first and second transition energies for semiconducting tubes and are related to strongly bounded excitons [36]. The E_{11}^{M} is for lowest values of transition energies for metallic SWCNT. The E_{33}^{SC} and E_{44}^{SC} are for 3rd and fourth transition energies for semiconducting tubes and are related to weakly bounded excitons [35].
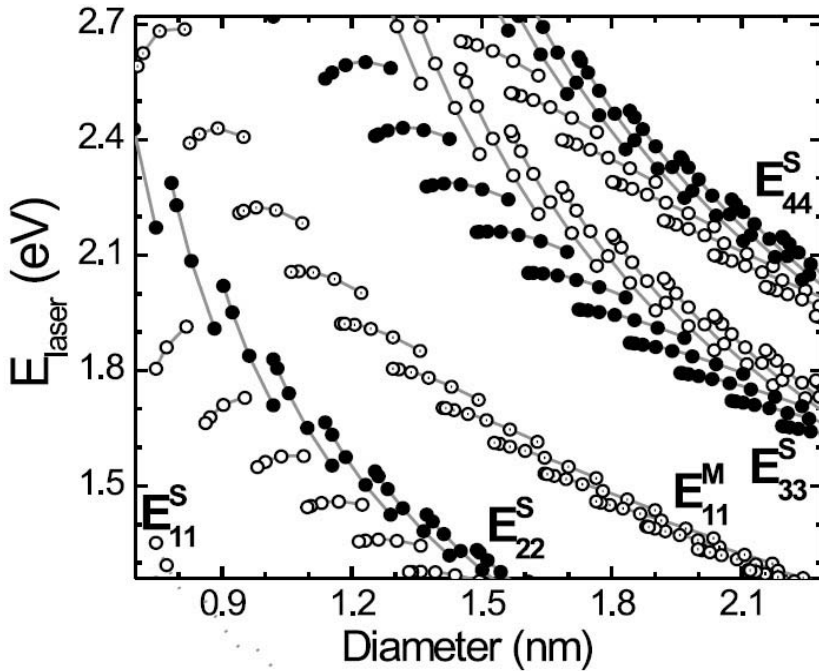
Figure 1.10: *The optical transition energies (dots) as a function of SWCNT diameter. Grey lines are a guide to the eyes for a group of SWCNT with $2n_1 + n_2$=constant. Open, filled, and dotted circles stand for E_{ii} for semiconducting type 1 $[(2n_1 + n_2)\text{mod}3 = 1]$, type 2 $[(2n_1 + n_2)\text{mod}3 = 2]$ and metallic SWCNT $[(2n_1 + n_2)\text{mod}3 = 0]$ respectively [35].*

The transition energies shown in Kataura plot can be traced by the expression

$$E_{ii}(p, d_t, \theta) = a\frac{p}{d_t}\left[1 + b log\left(\frac{c}{p/d_t}\right)\right] + \frac{\beta_p \cos(3\theta)}{d_t^2} + \frac{\gamma_p}{d_t} \qquad (1.30)$$

where p is the transition index ranging from 1 to 5 for E_{11}^{SC}, E_{22}^{SC}, E_{11}^{M}, E_{33}^{SC}, E_{44}^{SC} and E_{55}^{SC} respectively, d_t is the tube diameter, θ the chiral angle, a=1.049eV nm, b=0.456, c=0.812 nm^{-1} constant values, β_p a correction due to the chirality for upper and lower branches and $\gamma_p = 0.305 \pm 0.004$ a correction associated to

exciton localization for p > 3. The β_p values reported for the lower (upper) E_{ii} branches are -0.07(0.05), -0.19(0.14), -0.19(?), -0.42(0.42), and -0.4(0.4) for p = 1, 2, 3, 4, and 5, respectively [35].

1.2.3 Double and Multiwall Carbon Nanotubes

Double wall carbon nanotubes are composed of two coaxial graphene monolayers having different structural and electronic characteristics. Double wall tubes can be considered as the simplest form of multiwall nanotubes [37]. The synthesis of double wall tubes when using the CCVD method produces also single wall and triple wall carbon nanotubes tubes.

The first observation of double wall carbon nanotubes was reported by Dai et al [38]. They indicated the presence of a small quantity of double wall along with single wall tubes. Hafner et al showed that the double wall tubes production was related to the type of the catalyst [39]. Peigney et al improved the synthesis parameters for the growth of double wall tubes [40].

The double wall carbon nanotube provides unique opportunity to investigate the interaction between the concentric walls of CNT. The inner tube is shielded by the outer tube and have diameter comparable to the SWCNT. In DWCNT only the outer tube interacts with the environment. The environment can influence the electronic states. For example if the double wall tube is placed on substrate, the external tube interacts with the substrate. The coupling with the environment depends on whether the outer tube is semiconducting or metallic.

DWCNT can be grown by two methods: *1-* By the transformation of peapods [41]. Double-wall carbon nanotubes are synthesized in quantitative amount from the chains of C_{60} molecules in the interior of single-wall carbon nanotubes. First the C_{60} molecules are injected inside the single wall carbon nanotubes by vapor phase reaction. The C_{60} molecules inside the SWCNT remain inert up to 800 °C. Further heating up to 1200 °C convert the individual C_{60} molecules into chain and eventually the C_{60} molecules are converted into a tubular form. In this case, the inner tube is formed in the presence of an already present outer tube. *2-* Through the catalytic chemical vapor deposition method [42]. In CCVD method, the inner and outer tubes of DWCNT are formed at the same time.

One of the interesting finding is that the diameter of the inner tube is often smaller compared to the smallest diameter of single wall tubes. Double wall tubes exhibit in general a higher mechanical stability compared to SWCNT. The inner tube is protected from the the environment due to shielding of outer tube. The DWCNT properties are suitable for sensors and activators [43, 44].

It is the discovery of multiwall carbon nanotubes in 1991 by S. Iijima which created the scientific excitement for carbon nanotubes [4]. Multiwall carbon nanotubes are made of multiple wrapped layers (concentric tubes) of graphene [28].

The distance between two consecutive layers in multiwall carbon nanotubes is 0.34 nm which is close to the distance between graphene planes in graphite [10, 45]. The outer shell diameter of MWCNT can be greater then 30 nm [46]. Mainly, the number of walls defines the specific surface area along with some contribution from inner tube diameters. Coaxially oriented multi layers are intrinsically disordered as it is not possible to have simultaneous compatible epitaxy [47]. Experimentally, in multiwall tubes, the inter layer correlations are like the characteristics of turbostratic graphite in which the ABAB stacking pattern is disturbed [48]. There are many unique properties of multiwall tubes. Higher chemical reactivity has been experimentally observed for conformationally strained carbon atoms in multiwall tubes. Controlled removal of one shell of multi wall carbon nanotubes tube at a time is possible by the bias voltage through the shell [49]. This can be used to construct devices with metallic or semiconducting outer shells. Hydrothermal synthesis produce tubes with water filling that can be good model for investigating 1-D nano fluids and can be used as nanoreactors [50]. Direct fiber can be produced from the hot reactor plume or from the primordial soot [51, 52] or by twisting the vertically aligned multiwalls grown on a substrate as carpet type array [53, 54].

Carbon nanofibers are closely related to ordinary micron-sized carbon fibers. These fibers constitute a web of ultrathin monomolecular carbon fibers, each less than 0.1μm diameter: hence, follows the prefix nano, which refers to a typical diameter of several tens of nanometers. Such fibers are characterized by an extraordinarily high tensile modulus and tensile strength [55]. Other important properties of carbon nanofibers are their high electrical conductivity, extremely high corrosion resistance, invariability of mechanical properties over a very wide temperature range (from cryogenic temperatures to more than 1000 °C), and excellent compatibility with living tissues [56].

Nanofibers can have a tubular structure like micron sized vapor grown carbon fibers. Carbon nanofibres are synthesized by the catalytic decomposition of certain hydrocarbons on metal particles at temperatures from 400°C to 800 °C [57]. They composed of graphite platelets stacked in different ways with respect to the fibre axis. These structures can be called tubular, platelet or herringbone. These graphite platelets are stacked with an interlayer gap of 0.34 nm. An important feature of fiber structures is the large number of edges due the stacking of the graphene sheets, which leads to the sites for chemical or physical interaction. An unexpected observation about the carbon nanofibres,

is that these are ordered crystalline solids and can exhibit large surface areas, 300 to 700 m^2/g. The length of carbon nanofibres may vary from 5 to 100 μm and diameter from 5 to 100 nm [58]. The modification of the morphological structure, the extent of crystallinity and the orientation with respect to fiber axis is made by the choice of the catalyst, the amount of hydrocarbon and hydrogen in reactant mixture and reaction mixture.

1.3   Potential Applications of Carbon Nanotubes

Almost two decades of extensive research investigation, quasi one dimensional carbon nanotubes have shown a great promise in many domains like molecular electronics, energy storage, sensors, displays, nanoprobes and composite [5, 59, 60]. This is due to their remarkable physical properties which are the combined effects of dimensions, surface morphology and structure of carbon nanotubes. Since from the discovery, there is great deal of refinement in the synthesis and purification methods to produce high quality carbon nanotubes on a large scale suitable for different applications. The extensive studies of carbon nanotubes around the world has increased the understanding of CNT. This understanding has made the carbon nanotubes as front line material and lead it to more attractive for applications [6]. Carbon nanotubes applications can be divided into three regimes: applications which are already materialized and available in market, near future applications and applications which will be realized after many years.

Electron sources are important in research and in daily life. Carbon nanotubes can be used as electron source in two different ways. These two aspects are as single and multiple electron beam sources. The possible example of single beam source for high coherent electron beam is a single CNT as a field emission electron gun in an electron microscope. In flat panel displays, continuous or patterned film of nanotubes are the source of multiple independent electron beams. Cold electron emitters by field emission have exhibited great potential for large number of applications. The multiwall carbon nanotubes as cold electron source in prototype cathode ray tube demonstrated long life of MWCNT, stable electron emission and good emission stability [61]. Samsung has already demonstrated the 4.5 inch diode flat panel display fabricated with SWCNT [62]. In comparison to SWCNT, double wall tubes and multiwall tubes have higher structural stability, lower threshold voltage and higher emission current [63, 64]. Relatively low cost large area field emission displays can be fabricated from double wall carbon nanotubes or by thin multiwall nanotubes.

Efficiency of field emission by CNT can be enhanced by doping in carbon

nanotubes. Boron doped MWCNT have exhibited the higher field emission in comparison to pristine MWCNT [65]. Similarly nitrogen doped carbon nanotubes have also demonstrated the excellent field emission properties having low thresh hold voltage and higher current densities [66, 67].

Carbon nanotubes have high aspect ratio because of nanometer scale diameter and micrometer scale length. The small tip radius of carbon nanotubes are considered good for electron field emitters [68, 69]. This makes carbon nanotubes compatible as probe tips for scanning probe microscopes [30]. The main advantage of carbon nanotube probe is that it is very robust. The high aspect ratio of carbon nanotube helps to analyze the cracks or wear and tear in microelectronic circuits [70, 71]. The smaller radius of carbon nanotubes tips can scan the material with higher resolution [72]. The nanotubes are flexible and can be elastically buckled which can help to avoid the damage to biological and organic samples by restricting the application of maximum force [72]. There is less thermal vibrations for multiwall carbon nanotubes tips compared to tips made of single wall carbon nanotubes [73].

Carbon nanotubes have very large charge mobility 10^5 cm^2/Vs [74]. This leads carbon nanotubes as a material of choice for nanoelectronics, as it is unaffected by electro migration [75, 76] and having ballistic transport [27, 77]. The sorting and separation of SWCNT having different electronic and structural properties has enabled the researchers and scientist to make field effect transistors and interconnects [78, 79]. The field effect transistors made by SWCNT is promising for future nano size electronics [6]. The initial work on carbon nanotubes transistors has indicated that for semiconducting SWCNT, the channel conductance can be changed of the orders of magnitude 10^{15} by gate voltage just like MOSFET [80, 81]. CNT based power transistors have indicted 200 times higher current bearing capacity and 20 times low switching resistance then general power MOSFET.

On nanometer scale, the interconnects made of copper has surface and grain boundary scattering along with surface roughness which increases the resistivity of copper [82]. This limits the use of copper as interconnects on small scale. Metallic carbon nanotubes can also act interconnects and exhibit ballistic transport of electrons and have capacity to conduct very large current densities [83]. Bundles of parallel closely packed metallic carbon nanotubes or defect free large multiwall carbon nanotubes are suggested to be used as interconnects. The closely packed parallel tubes reduce the contact resistance and lower the capacitance which is high for [84].

Carbon nanotubes can act as nonvolatile memory due to the mechanical flexibility and electrical conductivity. Nanterro Inc. is fabricating a bistable memory which can be stimulated electrostatically [85]. It is expected that these

memory devices can be operated with high switching speed and at low voltages for millions of cycles. Single wall carbon nanotubes are applied to fabricate mechanically resilience and transparent thin film transistors [86]. These devices have exhibited good electrical properties along with very minute resistances, large optical transparency, mechanical resilience and high mobilities.

Large power consumption with the large amount of heat dissipation is one of the major challenge in the high performance microprocessors today. Individual nanotubes have already exhibited highest axial thermal conductivity. This high axial thermally conductivity of nanotubes can be used onchip thermal management. High cooling efficiency can be obtained in silicon chips with aligned MWCNT [87].

Electrical, optical, mechanical and electrochemical properties of carbon nanotubes can be used in carbon nanotube based sensors. Therefore, many studies have proposed CNT as the sensing material for pressure, gas, flow, thermal, optical, mass, position, stress, strain, biological, and chemical sensors [88]. Carbon nanotubes based sensors have the advantage that they are much smaller than MEMS sensors, use less power and have low sensitivity to variations in temperature [89].

The change in the resistance of SWCNT grown on membranes of suspended square poly silicon is indicated with the application of pressure. After the removal of pressure, poly silicon membrane came to its position prior to application of pressure. It is indicated in the study that hydrostatic pressure can result in radial deformation. The radial change result in electrical transition of nanotubes. Metal to semiconductor transition induced by pressure in armchair single wall nanotube has been reported. This pressure dependence changes can be used for designing of carbon nanotubes as tuneable pressure sensors [90].

The investigations by Kong et al have shown that [91] there is a sharp change in the resistance of SWCNT with the interaction of gaseous molecules like oxygen, nitrogen dioxide and ammonia. The response of nanotube based gas sensor is faster than solid state sensors and also has high sensitivity. In another study by Modi et al [92], it is reported that conduction in carbon nanotubes is very sensitive to variation in gas flow velocity, moisture and temperature. The capacitance of SWCNT is also reported having high sensitivity to broad range of vapors. This can be used to develop low power and fast adsorption based chemical sensors [93].

The carbon nanotubes composites are light, flexible, stiffer, stronger with higher thermal and electrical conductivities than other materials being in use now a days. Few of carbon nanotube composite applications are stated below.

In automobiles, the carbon nanotubes are used for fuel lining. Carbon nan-

otubes in the lining can prevent the static electricity which further reduces the risk of explosion [94]. Carbon nanotubes are also added to the skeleton of automobiles. Computer processors use thermal grease to conduct the heat away. The conductivity of the grease is increased by mixing the carbon nanotubes in the grease. This increases the rate of heat conduction from the processor [95]. Polymers are in general insulators. The thermal insulation of polymers is reduced by adding carbon nanotubes in the polymers. So the polymer composites having carbon nanotubes inside become conductors [96]. Sporting equipment made of carbon nanotubes composites are more strong and robust. The mixing of nanotubes also help to reduce vibrations in the sporting equipment. Robust and light weight textile structures can be made carbon nanotubes or carbon nanotube composites. The woven carbon nanotubes can be used as cables [97].

Bibliography

[1] P. Eklund *et al.*, Panel report, World Technology Evaluation Center, Inc., 4800 Roland Avenue Baltimore, Maryland (2007) (unpublished).

[2] M. T. Byrne and Y. K. Gunko, Advanced Materials **22**, 1672 (2010).

[3] N. Karousis, N. Tagmatarchis, and D. Tasis, Chemical Reviews (2010).

[4] S. Iijima, Nature **354**, 56 (1991).

[5] R. H. Baughman, A. A. Zakhidov, and W. A. de Heer, Science **297**, 787 (2002).

[6] M. Endo, M. S. Strano, and P. M. Ajayan, in *Potential Applications of Carbon Nanotubes*, Vol. 111 of *Topics in Applied Physics* (2008),

[7] O. Meinckea *et al.*, Polymer **45**, 739 (2004).

[8] H. W. Kroto *et al.*, Nature **318**, 162 (1985).

[9] A. K. Geim and K. S. Novoselov, Nature Mater **6**, 183 (2007).

[10] R. Saito, M. S. Dresselhaus, and G. Dresselhaus, *physical Properties of Carbon Nanotubes* (Imperial College Press, 203 Electrical Engineering Building Imprial College London SW7 2BT, 1998).

[11] L. Chico *et al.*, Physical Review Letters **76**, 971 (1996).

[12] G. Cao, Y. Tang, and X. Chen, Proceedings of the Institution of Mechanical Engineers, Part N: Journal of Nanoengineering and Nanosystems **219**, 73 (2005).

[13] M. S. Dresselhaus, G. Dresselhaus, and P. C. Eklund, *Science of Fullerenes and Carbon Nanotubes* (1995)

[14] http://drajput.com/notes/carbon_materials/carbon_materials_graphite.php.

[15] A. G. Marinopoulos, L. Reining, A. Rubio, and V. Olevano, Physical Review B **69**, 245419 (2004).

[16] E. H. Hwang, S. Adam, and S. D. Sarma, Physical Review Letter **98**, 186806 (2007).

[17] K. S. Novoselov *et al.*, Science **306**, 666 (2004).

[18] K. S. Novoselov *et al.*, in *Two-dimensional atomic crystals*, Proceeding of National Academy of Sciences of the United State of America (2005),

[19] L. A. K. Donev, Ph.D. thesis, Faculty of the Graduate School of Cornell University, (2009).

[20] S. Reich, J. Maultzsch, C. Thomsen, and P. Ordejon, Physical Review B **66**, 035412 (2002).

[21] J. W. G. Wilder *et al.*, Nature **391**, 59 (1998).

[22] C. Schonenberger, Bandstructure of Graphene and Carbon Nanotubes: An Exercise in Condensed Matter Physics, (2000).

[23] J. Maultzsch *et al.*, Physical Review B **72**, 205438 (2005).

[24] *Electron Transport in Mesoscopic Systems*, edited by S. Datta (Cambridge University Press, New York, 1995).

[25] M. Bockrath *et al.*, Nature **397**, 598 (1999).

[26] J. Kong *et al.*, Physical Review Letters **87**, 106801 (2001).

[27] A. Javey *et al.*, Nature **424**, 654 (2003).

[28] J. E. Fischer, in *Nanotubes and Nanofibers*, *Advanced Materials Series*, edited by Y. Gogotsi (Taylor and Francis Group, 6000 Broken Sound Parkway NW, Suite 300 Boca Raton, FL 33487-2742, (2006)).

[29] M. O. Connell, in *Carbon Nanotubes: Properties and Applications* (2006),

[30] M. Meyyappan, in *Carbon Nanotubes: Science and Applications* (2005),

[31] M. S. Dresselhaus, G. Dresselhaus, and P. C. Eklund, *Science of Fullerences and Carbon nanotubes* (Academic Press, New York, (1996)).

[32] M. Dresselhaus, G. Dresselhaus, and P. Avouris, *Carbon nanotubes: synthesis, structure, properties, and applications.* (Springer-Verlag, Germany, (2001)).

[33] A. Jorio *et al.*, MRS Bulletin **29**, 276 (2004).

[34] H. Kataura *et al.*, Synthetic Metals **103**, 2555 (1999).

[35] P. T. Araujo *et al.*, Physical Review Letters **98**, 067401 (2007).

[36] M. S. Dresselhaus, G. Dresselhaus, R. Saito, and A. Jorio, Annual Review of Physical Chemistry **58**, 719 (2007).

[37] R. R. Bacsa *et al.*, New Journal of Physics **5**, 131.1131.9 (2003).

[38] H. Dai *et al.*, Chemical Physics Letters **260**, 471 (1996).

[39] J. H. Hafner *et al.*, Chemical Physics Letters **296**, 195 (1998).

[40] A. Peigney, C. Laurent, F. Dobigeon, and A. Rousset, Journal of Materials Research **12**, 613 (1997).

[41] S. Bandow *et al.*, Chemical Physics Letters **337**, 48 (2001).

[42] E. Flahaut, R. Bacsa, A. Peigney, and C. Laurent, Chemical Communications **12**, 1442 (2003).

[43] T. Natsuki, T. Hayashi, and M. Endo, Applied Physics A: Materials Science and Processing **83**, 13 (2006).

[44] T. Natsuki, N. Fujita, Q. Q. Ni, and M. Endo, Journal of Applied Physics **106**, 084310 (2009).

[45] *The Science and Technology of Carbon Nanotubes*, edited by K. Tanaka, T. Yamabe, and K. Fukui (Elsevier Science Ltd, The Boulevard, Langford Lane Kidlington, Oxford OX5 1GB, UK, (1999)).

[46] X. K. Wang *et al.*, in *Carbon Nanotubes* (1996), 1 ed.,

[47] *Understanding Carbon Nanotubes From Basics to Applications*, *The Lecture Notes in Physics*, edited by A. Loiseau *et al.* (Springer Heidelberg, Physics Editorial Department I Tiergartenstrasse 17 69121 Heidelberg/Germany, (2005)).

[48] J. G. Lavin *et al.*, Carbon **40**, 1123 (2002).

[49] L. Qiuhong and W. Taihong, Science in China Ser. E Technological Science **47**, 1 (2004).

[50] Y. Gogotsi, J. A. Libera, A. G. Yazicioglu, and C. M. Megaridis, Applied Physics Letter **79**, 1021 (2001).

[51] H. W. Zhu *et al.*, Science **296**, 884 (2002).

[52] Y. L. Li, I. A. Kinloch, and A. H. Windle, Science **304**, 276 (2004).

[53] M. Zhang, K. R. Atkinson, and R. H. Baughman, Science **306**, 1358 (2004).

[54] K. Hata *et al.*, Science **306**, 1362 (2004).

[55] C. Weia and D. Srivastava, Applied Physics Letters **85**, 2208 (2004).

[56] D. Mendoza, Optical Materials **29**, 122 (2006).

[57] B. Louisa *et al.*, Catalysis **45**, 75 (2007).

[58] N. M. Rodriguez, A. Chambers, R. Terry, and K. Baker, Langmuir **11**, 3862 (1995).

[59] B. I. Yakobson and R. E. Smalley, American Scientist **85**, 324 (1997).

[60] P. M. Ajayan, Chemical Review **99**, 1787 (1999).

[61] Y. Saito, S. Uemura, and K. Hamaguchi, Japan Journal Applied Physics **37**, 346 (1998).

[62] W. B. Choi *et al.*, Applied Physics Letter **75**, 3219 (1999).

[63] Y. W. Son, S. Oh, J. Ihm, and S. Han, Nanotechnology **16**, 125 (2005).

[64] K. Seko, J. Kinoshita, and Y. Saito, Japan Journal of Applied Physics **44**, 743 (2005).

[65] J. C. Charlier *et al.*, Nano Letter **2**, 1191 (2002).

[66] M. Doytcheva *et al.*, Chemical Physics Letter **396**, 126 (2004).

[67] D. Golberg *et al.*, Applied physics. A, Materials science and processing **76**, 499 (2003).

[68] W. A. D. Heer, A. Chatelain, and D. Ugarte, Science **270**, 1179 (1995).

[69] Q. H. Wang *et al.*, Applied Physics Letters **70**, 3308 (1997).

[70] H. Dai *et al.*, Nature **384**, 147 (1996).

[71] G. Nagy *et al.*, Applied physics letters **73**, 529 (1998).

[72] S. S. Wong, J. D. Harper, P. T. J. Lansbury, and C. M. Lieber, Journal of American Chemical Society **120**, 603 (1998).

[73] C. V. Nguyen *et al.*, Applied Physics Letters **81**, 901 (2002).

[74] P. G. Collins, M. S. Arnold, and P. Avouris, Science **292**, 706 (2001).

[75] P. L. McEuen, M. S. Fuhrer, and H. K. Park, IEEE Transaction Nanotechnology **1**, 78 (2002).

[76] F. Kreup *et al.*, IEDM 683 (2004).

[77] C. Dekker, Physics Today **52**, 22 (1999).

[78] M. S. Arnold *et al.*, Nature Nanotechnology **1**, 60 (2006).

[79] G. Y. Zhang, Science **314**, 974 (2006).

[80] S. J. Tans, A. R. M. Verschueren, and C. Dekker, Nature **393**, 49 (1998).

[81] R. Martel *et al.*, Applied Physics Letter **73**, 2447 (1998).

[82] S. M. Rossnagel and T. S. Kaun, Journal of Vacuum Science and Technolology B **22**, 240 (2004).

[83] W. Liang *et al.*, Nature **411**, 649 (2001).

[84] A. R. Naeemi, R. Sarvari, and J. D. Meindl, IEEE Electron Device Letter **26**, 84 (2005).

[85] http://www.nantero.com/.

[86] Q. Cao *et al.*, Advanced Materials **18**, 304 (2006).

[87] K. Kordas *et al.*, Applied Physics Letter **90**, 123105 (2007).

[88] N. Sinha, J. Ma, , and J. T. W. Yeow, Journal of Nanoscience and Nanotechnology **6**, 573 (2006).

[89] R. J. Grow *et al.*, Applied Physics Letters **86**, 093104 (2005).

[90] J. Wu *et al.*, Physical Review B **69**, 153406 (2004).

[91] J. Kong *et al.*, Science **287**, 622 (2000).

[92] A. Modi *et al.*, Nature **424**, 171 (2003).

[93] E. S. Snow *et al.*, Science **307**, 1942 (2005).

[94] P. J. F. Harris, International Materials Reviews **49**, 31 (2004).

[95] B. H. Thang *et al.*, *International workshop on advanced material for new and renewable energy 2009*

[96] K. I. Winey, T. Kashiwagi, and M. Mu, MRS bulletin **32**, 348 (2007).

[97] N. M. Pugno, Journal of Physics: Condensed Matter **18**, 1971 (2006).

Chapter 2

Raman Spectroscopy of Carbon Nanotubes

Light is scattered by molecules and solids either elastically or inelastically. The inelastically scattered light is tiny fraction of the elastically scattered light. The inelastic scattering of light was first observed by Sir Chandrasekhra Venkata Raman in 1928. He was awarded the Nobel prize in 1930 for his contribution to inelastic light scattering. Raman used sunlight as a light source and used his eyes as a detector. Raman scattering is now used as an analytical technique for the characterization of materials. Raman spectroscopy is used in condensed matter physics and in chemistry for the study of vibrational and rotational modes. Dedicated instruments were developed to filter the elastically scattered light. The invention of lasers made this technique particularly useful. Similarly the technology of detectors has been progressed from photographic plates to photomultipliers and charge coupled detectors (CCDs). CCDs are now one of the most commonly used detectors in Raman spectroscopy [1, 2]. Advances in lasers, advanced optical components, such as volume-phase holographic filters and high performance array detectors, have made modern Raman instruments highly sensitive for routine analysis [3]. The objective of this chapter is to introduce the application of Raman spectroscopy on carbon nanotubes. For this purpose we shall discuss the theory of Raman scattering, Raman spectroscopy of different forms of carbon and construction and working of Raman spectrometers. The Raman spectroscopy of different forms of carbon includes the graphite, graphene, single wall carbon nanotubes, double wall carbon nanotubes and multiwall carbon nanotubes.

2.1 Raman spectroscopy

Raman spectroscopy is applied to explore the structural properties by observing vibrational modes of the material. Raman scattering is a process where photons interact with the material that means photons are absorbed and emitted (2 photons process). The emitted light is either elastically (Rayleigh) or inelastically scattered (Raman).
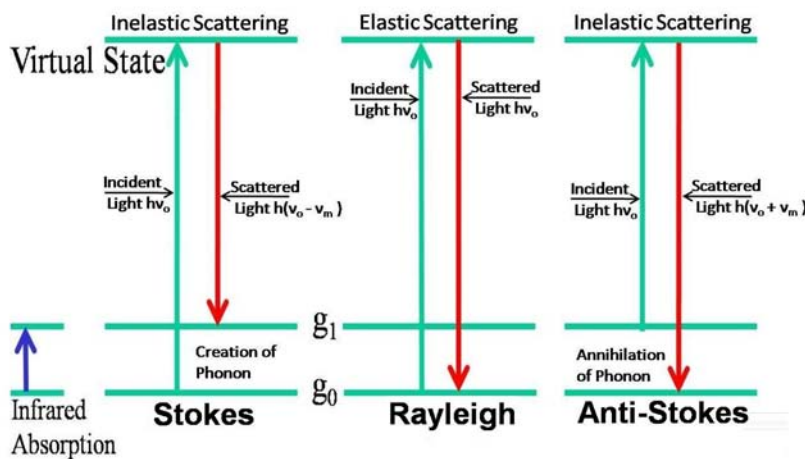
Figure 2.1: *Schematic of energy level diagram for infrared absorption, Rayleigh (elastic) scattering and Raman scattering. The frequency of the incoming light is ν_o. Rayleigh scattering has no change in energy of the emitted photon while in Raman scattering the scattered light has either frequencies ν_o - ν_m or ν_o + ν_m denoted by Stokes and antiStokes scattering respectively.*

When an atom absorbs photons, it will move to an virtual state (intermediate state corresponding to a characteristic eigenstate). These virtual states are not real (eigenstates: correspond to specific n or l state). The virtual states has short life time compared actual eigenstates. The life time of virtual state increases as it is closer to the eigen state.

Light is inelastically scattered due to the change of the polarizability of the molecule induced by the vibration. The incoming light polarizes the medium. The induced dipole depend on the polarizability which is described by a tensor. One component is associated with incident photon and second component corresponds to the scattered photon. The radiation emitted by the induced dipole moment contains the Rayleigh scattered radiation and Raman scattered radiation. The Rayleigh scattered light has a frequency equal to the frequency of the incoming radiation. The Raman scattered light is shifted in frequency from the frequency of incoming radiation and is much less intense. The shift in

energy with respect to the energy of the incident light is equal to the value of vibrational energy either gained or lost by the medium. The schematic energy level diagram of infrared absorption, Rayleigh scattering and Raman scattering are shown in figure 2.1.

The initial state g_o is the zeroth vibrational level of the ground electronic state and g_1 is the first vibrational level of the ground electronic state. Vibrational energy gain or loss by the molecule from the incident radiation gives rise two types of Raman scattering, Stokes or antiStokes respectively. The Stokes and antiStokes scattering are well differentiated in the figure 2.1.

The theoretical description of the Raman process is as follows. The frequency of the incident radiation is ω_o and ω_m is the vibrational frequency of the molecule. The frequencies of less intense Raman scattered light for Stokes and antiStokes are ω_o - ω_m and $\omega_o + \omega_m$ respectively. Rayleigh scattered light is intense and has the frequency ω_o. The electric field component of the laser beam is

$$E = E_o \cos(\omega_o t) \tag{2.1}$$

Where E_o is the amplitude of the electric field. A electric dipole moment P is induced when a molecule is irradiated and is given as

$$P = \alpha E = \alpha E_o \cos(\omega_o t) \tag{2.2}$$

Where the proportionality constant α is the polarizability of the molecule. So

$$\begin{bmatrix} P_x \\ P_y \\ P_z \end{bmatrix} = \begin{bmatrix} \alpha_{xx} & \alpha_{xy} & \alpha_{xz} \\ \alpha_{yx} & \alpha_{yy} & \alpha_{yz} \\ \alpha_{zx} & \alpha_{zy} & \alpha_{zz} \end{bmatrix} \begin{bmatrix} E_{ox} \cos(\omega_o t) \\ E_{oy} \cos(\omega_o t) \\ E_{oz} \cos(\omega_o t) \end{bmatrix}$$

The displacement of the atoms of the vibrating molecule is written as

$$s = s_o \cos(\omega_m t) \tag{2.3}$$

Where s_o is the amplitude of vibration and ω_m is the vibrational frequency of the molecule. α is a linear function of s for small vibration amplitudes and it can be written as

$$\alpha = \alpha_o + \left(\frac{\partial \alpha}{\partial s} \right)_o s + \cdots \tag{2.4}$$

α_o is the polarizability at the equilibrium position and $(\frac{\partial \alpha}{\partial s})_o$ is the rate of change of polarizability function of s. Taking the value of α from equation (2.4) and putting in equation (2.2), the equation for the dipole moment P is

$$P \approx \alpha_o E_o \cos(\omega_o t) + \left(\frac{\partial \alpha}{\partial s} \right)_o s E_o \cos(\omega_o t) \tag{2.5}$$

Now putting the value of s(from equation (2.3)) in equation (2.5)

$$P \approx \alpha_o E_o \cos(\omega_o t) + \left(\frac{\partial \alpha}{\partial s}\right)_o s_o E_o \cos(\omega_o t) \cos(\omega_m t)$$

$$P \approx \alpha_o E_o \cos(\omega_o t) + \frac{1}{2}\left(\frac{\partial \alpha}{\partial s}\right)_o s_o E_o[\cos(\omega_o + \omega_m)t + \cos(\omega_o - \omega_m)t] \quad (2.6)$$

The first term in the equation (2.6) shows that one term corresponds to Rayleigh scattered radiation of frequency ω_o. The second and third terms represent the antiStokes and Stokes Raman scattering at frequency $\omega_o + \omega_m$ and $\omega_o - \omega_m$ respectively. The factor $(\frac{\partial \alpha}{\partial s})_o$ indicates that only those vibrations are Raman active for which $(\frac{\partial \alpha}{\partial s})_o \neq 0$. So only those modes of vibrations give the Raman scattered light for which a polarizability change is associated. The intensity of the Stokes signal is higher compared to the intensity of the antiStokes signal. The reason for a higher Stokes signal is that the population of g_0 level is much larger than the population of the g_1 level according to Maxwell-Boltzman distribution which gives the population at different energy levels.

2.2 Resonance Raman Spectroscopy(RRS)

In resonance Raman spectroscopy, the energy of the incident laser or scattered light coincides with the real electronic transition energy of the molecule. The molecules are excited to, or near to real electronic states in resonance Raman scattering compared to simple Raman spectroscopy where the excitation involves virtual states. Tunable lasers can be used to find the excitation energies in resonance with the real electronic excited states. The intensity of the Raman scattered signal is much enhanced in resonance Raman spectroscopy (RRS). The intensity of Raman signal is

$$I \propto \alpha^2 \qquad (2.7)$$

where α is the molecular polarizability and ω_o is the incident radiation frequency. The Kramer-Heisenberg-Dirac expression for polarizability using quantum mechanical approach is given as

$$\alpha_{kj} \propto \sum_r \left[\frac{\langle f|\alpha_k|r\rangle\langle r|\alpha_j|i\rangle}{\omega_{ir} - \omega_o - j\Gamma_r} + \frac{\langle r|\alpha_k|i\rangle\langle f|\alpha_j|r\rangle}{\omega_{ir} + \omega_o - j\Gamma_r}\right] \qquad (2.8)$$

Where the subscript k and j are incident and scattered polarization directions. Initial, intermediate(virtual) and final vibronic states in the above

equations are represented by i, r and f respectively. $\jmath\Gamma_r$ is the damping factor and is inversely proportional to life time of the virtual vibronic state r. From equation (2.8), the denominator of the first term shows that resonance condition is achieved when $\omega_{ir} - \omega_o = 0$. The second term in the expression can be neglected due to the addition of frequencies ω_{ir} and ω_o This means when the intensity will be maximum when the excitation frequency will be equal to the electronic transition frequency. Scattering is illustrated in figure 2.2
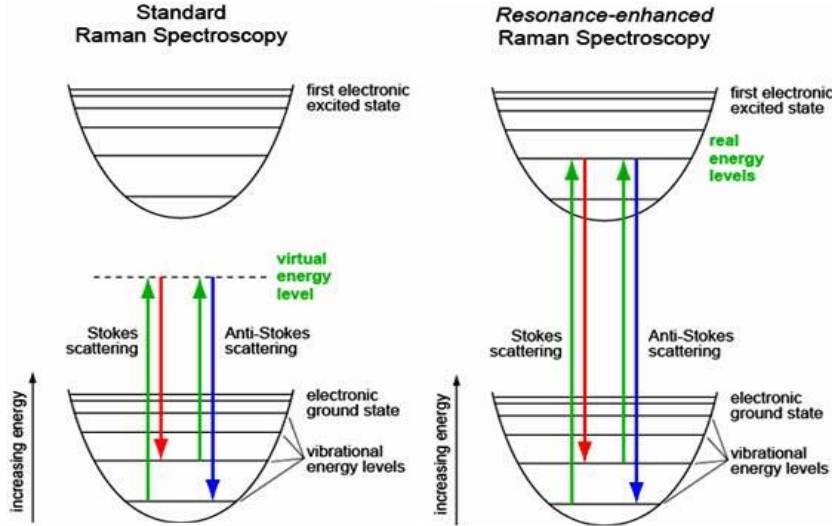
Figure 2.2: *The figure on left represents the normal Raman scattering by exciting the electrons to virtual states. The figure on the right is for resonance Raman spectroscopy showing that excitation of electrons to real states [4]*

.

The real advantage of RRS compared to normal Raman scattering is the large increase in the intensity of Raman peaks. This permits to use lower concentration of samples for RRS than normal Raman spectroscopy. The major disadvantages associated with RRS are the possibility of the appearance of fluorescence and photo degradation of the sample because of the increased energy of absorbed radiation. Using RRS it is possible to observe an individual carbon nanotube.

2.3   Raman Intensity

The Raman process involves the creation of a phonon in the Stokes process or the annihilation of a phonon in antiStokes process. The population of phonons in the lattice at the thermal equilibrium is [5]

$$n_o(\omega_m, T) = [exp(\hbar\omega_m/kT) - 1]^{-1} \tag{2.9}$$

Where ω_m is the phonon frequency, k is the Boltzman's constant and T is the lattice temperature. The intensity of Stokes part of Raman scattered light is given by

$$\frac{dI_S}{d\Omega} = K\omega_o\omega_S^3 \frac{n_S(T)}{n_L(T)}\sigma_S(T)V_S(T)[n_o(\omega_m, T) + 1] \tag{2.10}$$

Where the subscripts L and S stands for laser and Stokes respectively. V is the effective volume, n represents the refractive index, K is the constant and σ is the Raman cross section proportional to α^2. Similar equation for antiStokes intensity can be given by replacing $n_o + 1$ by n_o in equation(2.10).

$$\frac{dI_{AS}}{d\Omega} = K\omega_o\omega_{AS}^3 \frac{n_{AS}(T)}{n_L(T)}\sigma_{AS}(T)V_{AS}(T)[n_o(\omega_m, T)] \tag{2.11}$$

The differential intensity per unit solid angle Ω given by equation(2.10) and(2.11) is inside the crystal. The intensity outside the crystal can be calculated by integrating the equations (2.10) and (2.11) and by replacing

$$K\frac{n_S(T)}{n_L(T)} = K'\frac{[1 - R_S(T)][1 - R_L(T)]}{n_S(T)n_L(T)} \tag{2.12}$$

and

$$V_S(T) \approx [\alpha_L(T) + \alpha_S(T)]^{-1} \tag{2.13}$$

where R is the reflectivity and α is the absorption coefficient. Hence the intensity for stokes Raman scattered light is given as

$$I_S = K'\omega_o\omega_S^3 \frac{\sigma_S(T)[1 - R_S(T)][1 - R_L(T)]}{n_S(T)n_L(T)[\alpha_L(T) + \alpha_S(T)]} \times [n_o(\omega_m, T) + 1] \tag{2.14}$$

and for antiStokes it is given as

$$I_{AS} = K'\omega_o\omega_{AS}^3 \frac{\sigma_{AS}(T)[1 - R_S(T)][1 - R_L(T)]}{n_{AS}(T)n_L(T)[\alpha_L(T) + \alpha_{AS}(T)]} \times [n_o(\omega_m, T)] \tag{2.15}$$

In the above equations, the spectrometer throughput correction can be included which is wavelength dependent and depends on the experimental system used.

2.4 Spectrometer Dilor XY and Renishaw

*1- **Dilor:*** The figure 2.3 shows the schematic diagram of micro-Raman DILOR XY. The light source for the excitation of sample is a Krypton-Argon laser. Laser power can be reduced by using filters. This spectrometer allows to take backscatter measurements in which the incident beam is focused by the objective of magnification 40 or 100 with an Olympus microscope and the incident

beam is normal to the sample surface resulting in the scattering of Raman photons in all directions. Only the backscattered photons are collected by the microscope objective and then focused on the entrance slit S_1 a first monochromator. This first monochromator is composed of two holographic gratings (g_1 and g_2) with grooving density 1800 lines/mm and is used to eliminate the Rayleigh component (the laser beam). Finally, the scattered beam is dispersed by the spectrometer grating g_3 and then collected by a liquid nitrogen cooled multichannel CCD detector (Charged Coupled Device).
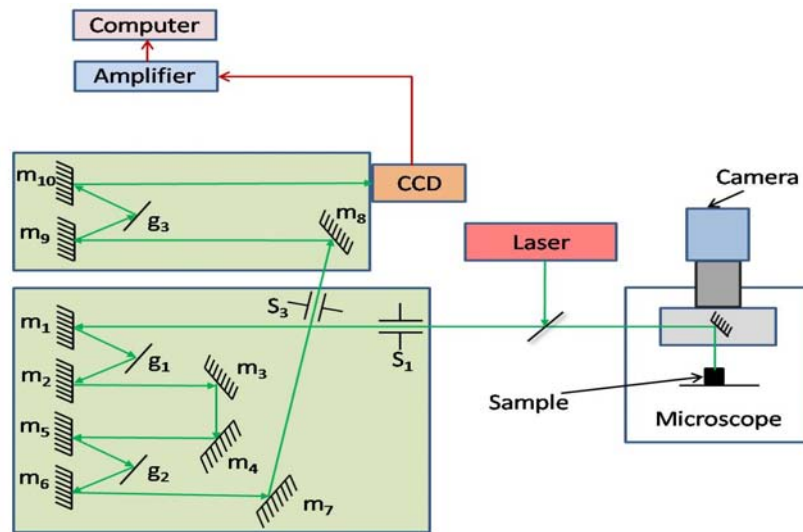
Figure 2.3: *Schematic diagram of DILOR XY spectrometer*

*2- **Renishaw:*** The light source used for sample excitation in Renishaw spectrometer at Queens Marry University of London (QMUL) is a $\leq$60 mW He-Ne laser with a wavelength of 632.8 nm. The excitation source used in Renishaw spectrometer at CEMES Toulouse is $\leq$100 mW Argon laser having wavelength 514 nm.

The light emitted by the source enters the system from the back and incidents on the first steering mirror (B) which guides the light towards the first objective (x 4 objective) of the beam expander (C). The divergent light, is then received by objective and a parallel beam comes out of the back of the objective. Then, the light incidents on the holographic notch (in QMUL) filter (F) by the second steering mirror (D) and the fixed pre-filter mirror (E). Now, the holographic notch filter uses as a reflecting mirror, by which the incident beam is reflected to the microscope 45° reflecting mirror (G), and then focused on the sample using an objective (H). After hitting of light on the sample, the back-scattered light will be collected by the same objective, and directed to the holographic notch filter. Here the notch filter will allow only the light above

the $\sim$200 cm^{-1} from the source light, to pass through [6]..

The light passing the filter is focused through a pre-slit lens (I) on a horizontal slit (J) from where through a collimating lens (K), incident on a triangular mirror (M). The triangular mirror directs the light onto a 1800 lines/mm diffraction grating (L) from where, by using the other side of the triangular mirror, it is passed through a focusing lens (N) and focused onto a 400 x 600 pixel CCD detector (O) which is cooled by Peltier effect.
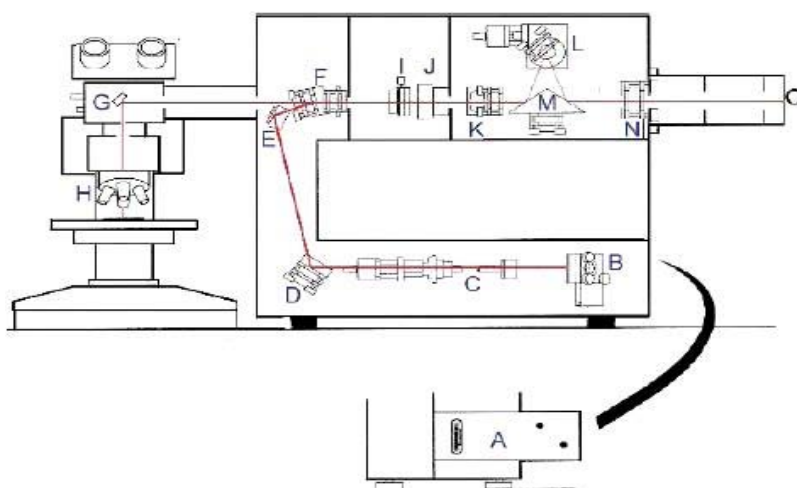
Figure 2.4: *Schematic drawing of the Renishaw Raman microscope system taken from the Renishaw imaging microscope User Guide. A is the source of light, B, D, E, G and M are reflecting mirrors, C is a motorized beam expander, F is the holographic notch filter, I is the pre-slit lens, J is the horizontal narrow slit, L is the grating and O is the CCD chip [6].*

2.5 Raman spectroscopy of different forms of carbon

Raman spectroscopy is unique to the nanostructured carbon materials and is successfully applied to differentiate different sp^2 carbon nanostructures (graphite, graphene, fullerenes, and carbon nanotubes). The investigations of nanostructured carbon materials with Raman spectroscopy helped to explore many fundamental aspects of their electronic and vibrational properties [7].

2.6 Raman Spectroscopy of Graphite

Here we present the very brief overview of the Raman spectra of graphite. First we introduce the space group, point group and symmetries associated with the

graphite and latter we shall discuss the Raman bands present in the spectra of graphite. Particularly the origin of defect induced D band with double resonance process will be illustrated.

Graphite is constructed from layers of carbon atoms. The unit cell contains four atoms distributed in two layers. The two planes are linked by translation or by C_6 a rotation around the six fold symmetry axis followed by a translation perpendicular to the graphite planes. The space group of graphite is $P6_3$/mmc (D_{6h}^4) and its isogonal point group is D_{6h}. The physical properties of graphite can essentially be understood by a single hexagonal plane of carbon atoms (graphene). The weak interaction between the layers [8] decouples the planes to a large degree. Graphene has only one Raman active mode: E_{2g}. There are two E_{2g} Raman-active modes at the Γ point of the Brillouin zone for a graphite crystal (42 cm^{-1} and 1582 cm^{-1}). Figure 2.5 shows the different graphene and graphite modes. There are also non Γ phonons (near high symmetry points K and M) in the Raman spectra of graphite.
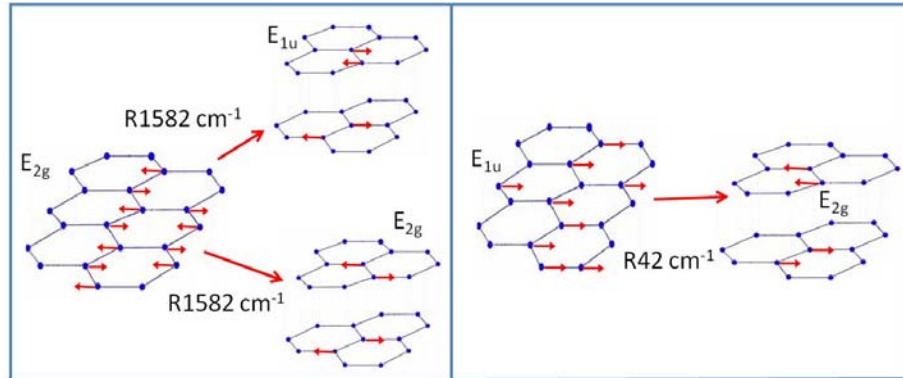
Figure 2.5: *Phonon eigenvectors of graphene and graphite [8].*

Figure 2.6(a) shows the Raman spectrum of well-ordered defect-free graphite. The first-order E_{2g} optical mode called G (C-C stretching mode) mode is at 1582 cm^{-1}. The second-order spectrum of graphite is quite interesting. The frequency of the 2G peak (close to 3200 cm^{-1}) is, as experimentally observed, higher than the two times of G band frequency. The 2G mode is in fact linked with the over bending of the longitudinal optical phonon branches of graphite. This shows that the LO branch is maximum not at the Γ point of the Brillouin zone [8]. Another interesting band which appear near 2700 cm^{-1} is called the 2D band.
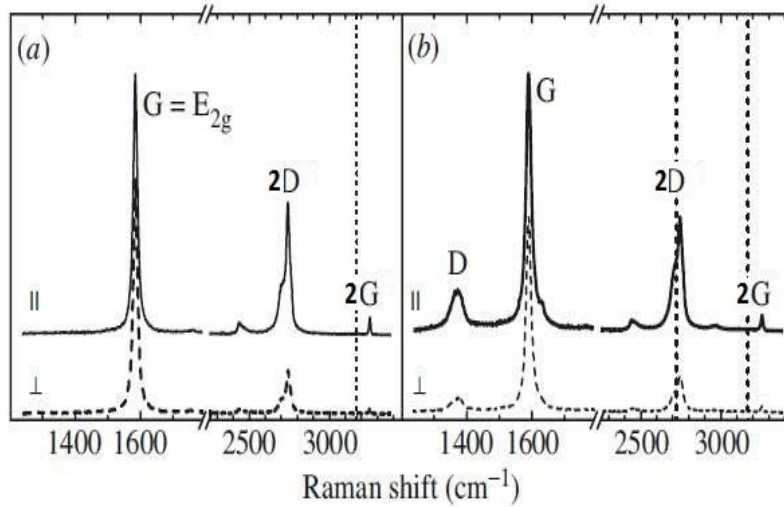
Figure 2.6: *In figure(a) first and second-order Raman spectrum of a perfect Kish graphite. The first-order spectrum shows a single line at 1582 cm^{-1}. In figure(b) Raman spectrum of disordered graphite. There is an additional line at 1370 cm^{-1} and a high-energy shoulder at the E_{2g} in figure(b). Solid (dashed) lines are for parallel (perpendicular) polarization of the incoming and outgoing light [8].*

Figure 2.6(b) shows the Raman spectrum of disordered graphite. A defect induced D mode appears near 1370 cm^{-1} in the first order spectrum. The second order spectra is not much affected by disorder or defects. The 2D band position is near twice the D band frequency. So the 2D band can be assigned as a second order D band.
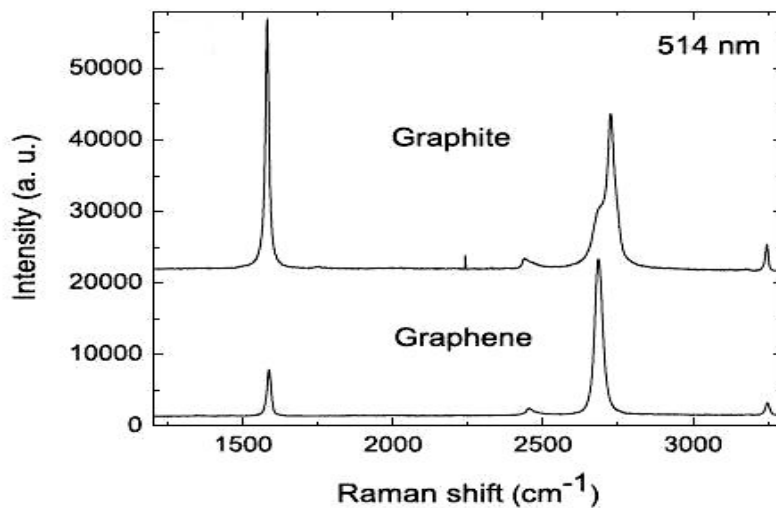
Figure 2.7: *The Raman spectra of graphite and graphene [9].*

The D band is dispersive meaning the frequency upshifts with increasing

laser excitation energy. The shift is linear over a wide range of excitation energies (near IR to near ultraviolet (UV)) having slope between 40 and 50 cm^{-1} eV [8]. The 2D band also upshifts with increasing laser excitation energy. The upshift with excitation energy for the 2D band is twice the upshift of the D band. This confirms that the 2D band is a overtone band of D band. [8].

The origin of the D band can be explained by double resonance which is unique to the electronic band structure of graphite and other sp^2 bonded carbon. The double resonance in Raman scattering is due to the combination of the phonon dispersion and electronic band structure. To explain the defect induced Raman scattering process in graphite, we need to look at the optical transitions in the visible range.
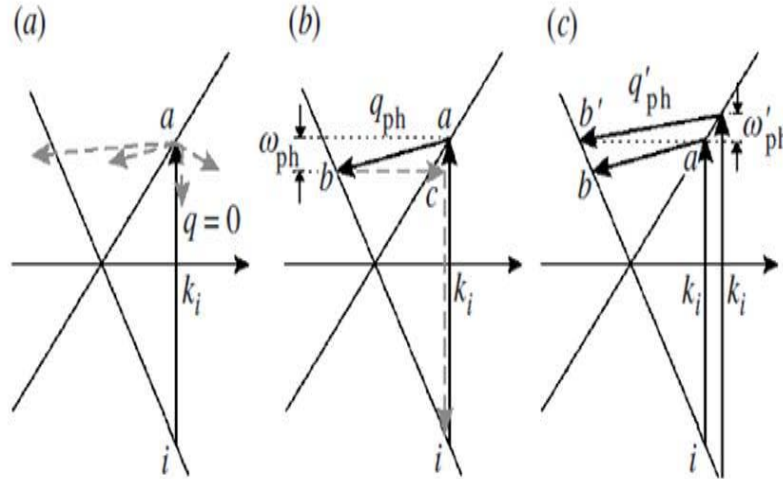
Figure 2.8: *Double resonance scattering for D mode [8].*

In the figure 2.8(a) two linear electronic bands are shown which are intersecting each other at the Fermi level. The incident photon of energy E$_1$ excites an electron from state i of the valence band to a state a of the conduction band. The eigen energies of the electrons are E$_a^e$ and E$_i^e$ in the conduction and valence band respectively. The excited electron scattered by phonons of wave vector q is indicated by dashed arrow in figure 2.8(a). The scattering probability is high (resonant scattering) when the phonon scatters the electron into another real electronic state b as shown in figure 2.8(b). A defect in the structure can elastically scatters the electron back. This is shown by a dashed arrow from state b to state c in figure 2.8(b). The scattered photon is emitted by recombination of electron-hole pair and has the energy (figure 2.8(b)) $E_2 = E_1 - \hbar\omega_{ph}$ where ω_{ph} is the energy of the phonon and $E_1 = E_a^e - E_i^e$. This process including the scattering on defects is called double resonant Raman process.

With the increase of laser energy, the energy and momentum of the photo excited electron increases, the double resonant phonon energy shifts to larger values as represented in figure 2.8(c) which shows the double resonant scattering process for two different excitation energies. The D band is independent of the type of disorder [8].

The Raman spectra of the D mode calculated by Thomsen and Reich [10] using double resonant Raman process is in an excellent agreement with experimentally measured values [11]. This shows that double resonant Raman scattering process explains the excitation energy dependence of Raman D mode [8].

2.7 Raman Spectroscopy of Single Wall Carbon Nanotubes

The phonon dispersion relations and phonon density of states for SWCNT can be derived from those of the 2D graphene sheet [12]. Raman spectroscopy is the frequently used for the characterization of carbon nanotubes [12–15]. Analysis of Raman spectra and the resonance conditions give information about the phonon energy, electronic states and electron phonon coupling. The unusual optical and spectroscopic characteristics observed in single wall carbon nanotubes are mainly due to the one-dimensional confinement of electronic and phonon states which results in van Hove singularities (vHSs) in the nanotube density of states [12, 15].
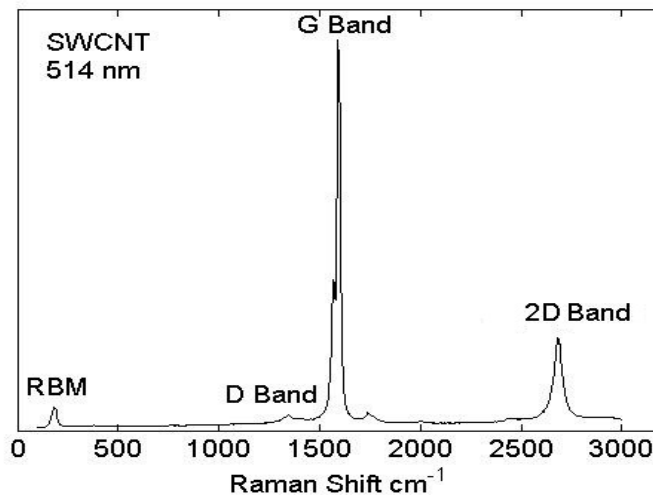
Figure 2.9: *Raman spectrum of a SWCNT at 514 nm laser excitation wavelength.*

A typical Raman spectra of single wall carbon nanotubes is shown in the

figure 2.9. The spectra can be divided into different regions. In the low energy region from 50 cm^{-1} upto 400 cm^{-1} one finds the radial breathing modes (RBM). RBM band is observed when the electronic transition energy of carbon nanotube is in resonance with the excitation energy of the excitation laser. The high energy region between 1200 cm^{-1} and 1650 cm^{-1} contains the D band and the graphite mode (G band). The Raman bands in region from 2500 cm^{-1} to 3200 cm^{-1} are due to combinations of the D and G bands.
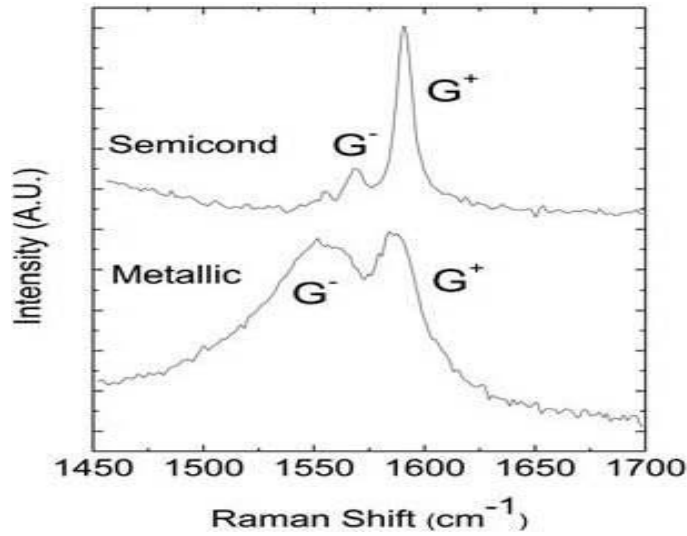
Figure 2.10: *G mode Raman spectra of semiconductor and metallic SWCNT [15].*

The nature of single wall carbon nanotubes either metallic or semiconductor can be determined by observing the G band shape (figure 2.10) of the Raman spectra. The diameter of the SWCNT can be determined by Raman spectroscopy by observing the RBM frequency.

The RBM frequency is inversely proportional to the diameter of the tube. The relation between RBM frequency and diameter can be written as

$$\omega_{RBM} = \frac{C_1}{d} + C_2 \tag{2.16}$$

where C_1 and C_2 are two constants. The different values C_1 and C_2 taken from the literature are shown in the figure 2.11 [16–20].

Carbon nanotubes appear in different diameters and are often bundled. When SWCNT in bundles are excited by different laser excitation wavelengths, the different tubes are in resonance.
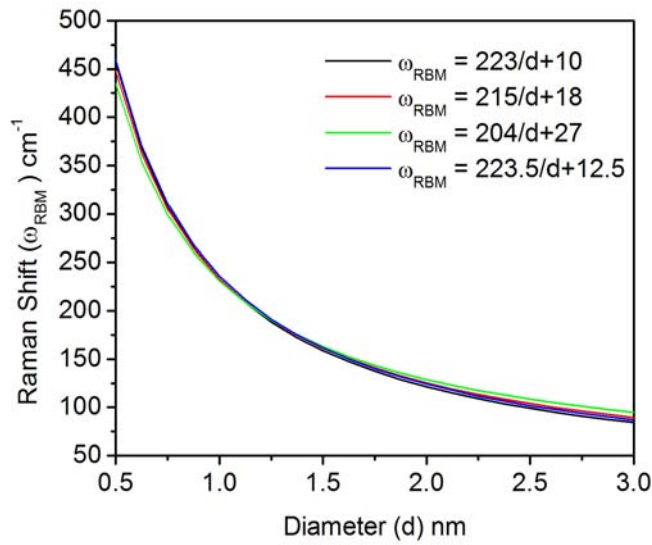
Figure 2.11: *RBM frequency as a function of diameter with different formulas [21].*

In figure 2.12 shows the raman spectra excited with 76 different laser energies ranging between 1.52 and 2.71 eV in the low energy frequency range of SWCNT (Hipco) wrapped with sodium dodecyl sulfate (SDS) molecules dispersed in aqueous solution. Each peak in the figure 2.12 correspond to carbon nanotube type (n_1,n_2) in resonance with a specific E_{laser} excitation frequency.
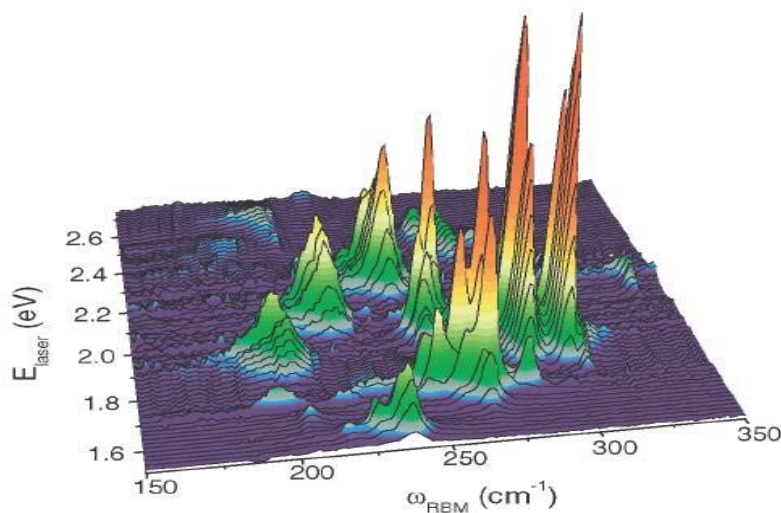
Figure 2.12: *RBM Raman measurements of HiPco SWNTs dispersed in SDS aqueous solution, measured with 76 different laser lines E_{laser} [22].*

The D mode mode has same origin in CNT as in graphite. Defects in carbon nanotubes can be due to the formation of pentagone-heptagone (Stone walls) pairs, impurities in the tube wall or because of the finite length of CNT. The possible defect structures can be classified into four main groups: topological (introduction of ring sizes other than hexagons), rehybridization (ability of carbon atom to hybridize between sp^2 and sp^3), and incomplete bonding defects (vacancies, dislocations) and doping with other elements [23]. In general the increase of defects concentration increases the intensity of the D mode. It has been observed that the D band position is dependent upon the diameter of the nanotube [24].

The high energy modes called G band, lies in the 1550 cm^{-1} to 1600 cm^{-1}. The G band is composed of more than one band which correspond to tangential and longitudinal vibrations of carbon atoms as shown in figure 2.13. For SWCNT, the unique feature of the G band is the characteristic band shape which is different for semiconducting and metallic nanotubes.
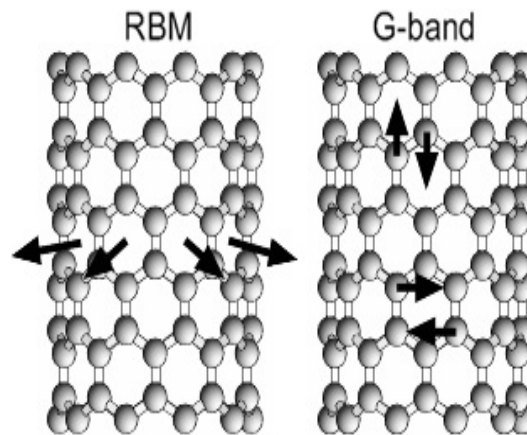
Figure 2.13: *Schematic diagram showing the atomic vibrations for the RBM and G band modes [25].*

G mode has two components G^- and G^+ for SWCNT. For semiconducting SWCNT the G^- and G^+ have Lorentzian line shape while for metallic tubes, the G^- has a very broad Breit-Wigner-Fano line shape while the G^+ is Lorentzian. By observing the G band shape of SWCNT one can in principle recognize whether the tube is semiconducting or metallic as shown in in figure 2.10. It has been observed that a lower frequency G^- peak depends upon the diameter of the tube whereas the G^+ does not depend upon diameter [26].

Furthermore it has been found that the shift of G mode with temperature can be used to estimate the temperature [27]. Charge transfer on the carbon nanotubes can also be observed by frequency shifts of G mode [28, 29]. Higher

order Raman bands with less intensity can be observed for individual SWCNT. These Raman bands are attributed to combinations of zone-center and pairs of zone-edge optical phonons [30]. Multiphonon Raman peaks of SWCNT excited with 473 having frequency shifts higher than $1000\,\mathrm{cm}^{-1}$ are observed and shown in table 2.1.

Table 2.1: *Assignment of the Raman modes from the SWCNT in terms of combinations of G and even number of D-band phonons [30].*

Number	Experimental shift cm^{-1}	Raman mode
1	2710	2D
2	3182	2G
3	4296	G + 2D
4	4828	3G
5	5340	4D
6	5891	2G + 2D
7	6220	4G
8	6920	G + 4D
9	7432	3G + 2D
10	8400	2G + 4D

2.8   Raman Spectroscopy of Double Wall Carbon Nanotubes

Figure 2.14 shows the Raman spectra of double wall carbon nanotubes. Due to the weak interlayer interactions between the two coaxial tubes no new modes are expected and the band intensities are dominated by the selection rules for individual single wall carbon nanotubes. The RBM modes of double wall tubes consist of two Raman bands corresponding to the breathing mode of each tube. There is a small shift due to chirality and inter layer interactions of two concentric tubes which depends on diameter. However these effects are small and the diameter calculated by lower frequency peak RBM is approximately equal to the diameter measurements by high resolution transmission electron microscopy (HRTEM). In principle for a given outer tube several inner tubes are possible for variable interlayer spacing (0.37-0.41 nm) [31].

For DWCNT, the G band is broad compared to SWCNT and it was first assumed that it is simply the addition of SWCNT contributions. In DWCNT the G band is not the same as in SWCNT. Considering the G^- and G^+ bands of SWCNT, it was expected that the G band of DWCNT should have four peaks and the composition should be two peaks for inner tube (G_i^- and G_o^+) and two for outer (G_o^- and G_o^+). However, the experimental findings indicated

that interpretation of DWCNT based on SWCNT is inconsistent. Chemical doping experiments of DWCNT by Chen *et al.* [32] and high pressure Raman spectroscopy experiments by Puech *et al.* [33, 34] have shown that the G band is composed of at least two separated bands. These two bands are attributed to the inner and outer tubes of DWCNT. The frequency of the inner tube is at 1581 cm^{-1} and the frequency of the outer tube is higher and close to 1592 cm^{-1}. The frequency of the inner tube is less sensitive to external perturbations than the frequency of the outer tube [35]. High pressure Raman spectroscopy experiments revealed that the pressure transmission on the inner tube is delayed for DWCNT from peapods as compared for DWCNT grown with the CCVD method when pressure is increased [33].
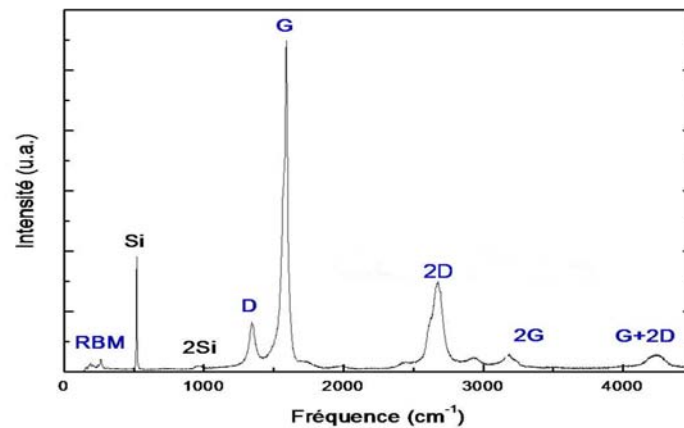
Figure 2.14: *Raman spectra of double wall carbon nanotubes showing Raman active modes in different frequency regions.*

The DWCNT synthesized by CCVD and peapods show differences in the 2D band. The 2D band for DWCNT grown form peapods has two separated contributions due to inner and outer tubes while the 2D band for DWCNT grown with the CCVD method shows only one band with a shoulder similar to what is observed for graphite. Thus the analysis 2D mode features can explain the atomic correlation of inner and outer tube of DWCNT synthesized from CCVD and peapods transformation [31].

2.9   Raman Spectroscopy of Multiwall Carbon Nanotubes

Multiwall carbon nanotubes has several coaxial SWCNT. The concentric tubes leads to a large diameter of outer tube and small diameter for inner most single wall carbon nanotube [15]. The Raman spectra of MWCNT is different from Raman spectra of SWCNT while the difference between Raman spectra

of MWCNT and graphite is not obvious. This similarity for MWCNT and graphite Raman spectra is because of several concentric assembly of tubes. However some times RBM mode is observed for very narrow diameter inner tube if resonance conditions are very good [36, 37]. Clear and strong radial breathing mode are seen for inner most tube of narrow diameter less then 1 nm synthesized by using hydrogen gas in the arc discharge process [38].
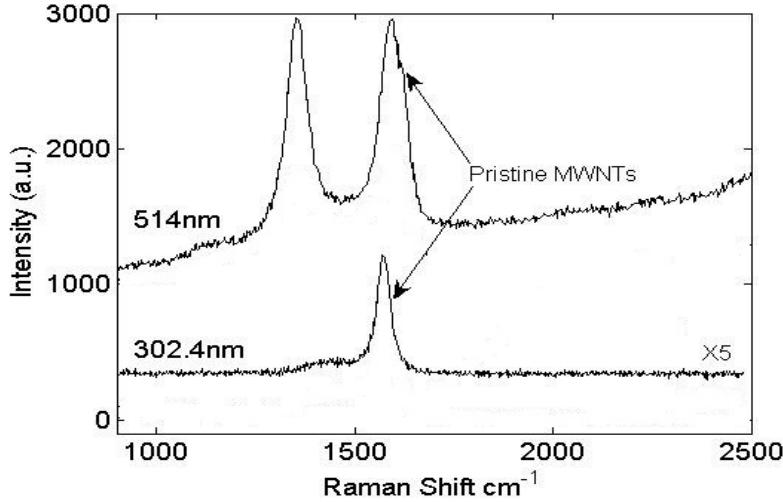
Figure 2.15: *Raman spectra of MWCNT at 514nm and 302.4nm.*

The Raman spectra of MWCNT with visible and ultraviolet laser excitation are shown in figure 2.15. The intensity of G band is considerably reduced for 302.4 nm and D band is almost absent. The intensity of G mode for MWCNT is low compared to SWCNT with the elimination of splitting due to distribution of diameter and assembly of tubes. Vidano *et al.* [39] has reported that D band frequency of different kinds of carbon materials strongly depends on the laser excitation energy (E_{laser}) and upshifts linearly with increasing laser excitation energy. The frequency shift coefficient is $\frac{\partial \omega_D}{\partial E_{laser}} \simeq 50 cm^{-1}/eV$. The D band frequency shift coefficient is also found independent of materials for different graphitic materials [11]. The quality of crystal structure in carbon nanotubes is used to observe with ratio of integrated intensities of D band and G band (I_D/I_G). Lower the I_D/I_G higher will be the quality of graphite lattice of nanotubes. The I_D/I_G ratio depends on the laser excitation energy [40]. The value of I_D/I_G is also found proportional to $(E_{laser})^{-4}$ by assuming the value of I_G independent of laser energy [41].

Bibliography

[1] J. H. Giles, D. A. Gilmore, and M. B. Denton, Journal of Raman Spectroscopy **30**, 767 (1999).

[2] M. B. Denton *et al.*, Australian Journal of Chemistry **56**, 117 (2003).

[3] S. C. Denson, C. J. S. Pommier, and M. B. Denton, Journal of Chemical Education **84**, 67 (2007).

[4] http://www.semrok.com/.

[5] G. E. Jellison, D. H. Lowndness, and R. F. Wood, Physical Review B **28**, 3272 (1983).

[6] A. J. Ghandour, Ph.D. thesis, Department of physics Queen Mary, University of London, (2009).

[7] M. S. Dresselhaus *et al.*, Nano Letters **10**, 751758 (2010).

[8] S. Reich and C. Thomsen, Philosphical Transaction Royal Society London A **362**, 2271 (2004).

[9] A. C. Ferrari *et al.*, Physical Reveiw Letters **97**, 187401 (2006).

[10] C. Thomsen and S. Reich, Physical Review Letters **85**, 5214 (2000).

[11] Y. Wang, D. C. Alsmeyer, and R. L. McCreery, Chemical Mater **2**, 557 (1990).

[12] R. Saito, M. S. Dresselhaus, and G. Dresselhaus, *physical Properties of Carbon Nanotubes* (Imperial College Press, 203 Electrical Engineering Building Imprial College London SW7 2BT, 1998).

[13] L. Alvarez *et al.*, Physical Review B **63**, 153401 (2001).

[14] H. Kuzmany, R. Pfeiffer, M. Hulman, and C. Kramberger, Philosophical Transactions: Mathematical, Physical and Engineering Sciences **362**, 2375 (2004).

[15] M. S. Dresselhaus, G. Dresselhaus, R. Saito, and A. Jorio, Physics Reports **409**, 47 (2005).

[16] S. Rols *et al.*, Physical Review Letter **85**, 5222 (2000).

[17] R. A. Jishi, L. Venkataraman, M. S. Dresselhaus, and G. Dresselhaus, Chemical Physics Letters **209**, 77 (1993).

[18] A. M. Rao *et al.*, Science **275**, 187 (1997).

[19] J. C. Meyer *et al.*, Physical Review Letter **95**, 217401 (2005).

[20] S. M. Bachilo *et al.*, Science **298**, 2361 (2002).

[21] A. Bassil, Ph.D. thesis, Univesité Paul Sabatier de Toulouse, (2006).

[22] C. Fantini *et al.*, Physical Review Letter **93**, 147406 (2004).

[23] J.-C. Charlier, Accounts Of Chemical Research **35**, 1063 (2002).

[24] A. G. S. Filho *et al.*, Physical Review B **63**, 241404 (2001).

[25] A. Jorio *et al.*, New Journal of Physics **5**, 117 (2003).

[26] M. S. Dresselhaus *et al.*, Carbon **40**, 2043 (2002).

[27] P. Puech *et al.*, Physical Review B **79**, 085418 (2009).

[28] I. O. Maciel *et al.*, Nano Letters **9**, 2267 (2009).

[29] M. Freitag, J. Tsang, and P. Avouris, physica status solidi (b) **245**, 2216 (2008).

[30] F. Wang *et al.*, Physical Review Letter **98**, 047402 (2007).

[31] W. Ren and H. M. Cheng, in *Nanoscale Phenomena*, Vol. 2 of *Lecture Notes in Nanoscale Science and Technology* (2008),

[32] G. Chen *et al.*, Physics Review Letters **90**, 257403 (2003).

[33] P. Puech *et al.*, Physical Review B **78**, 045413 (2008).

[34] P. Puech *et al.*, Physics Review Letters **93**, 095506 (2004).

[35] S. Yuan *et al.*, Nano Letters **9**, 383 (2009).

[36] J. M. Benoit *et al.*, Physical Review B **66**, 073417 (2002).

[37] Y. Zhao, B. I.Yakobson, and R. E. Smalley, Physics Review Letters **88**, 185501 (2002).

[38] X. Zhao *et al.*, Chemical Physics Letter **361**, 169174 (2002).

[39] R. P. Vidano, D. B. Fischbach, L. J. Willis, and T. M. Loehr, Solid State Communications **39**, 341 (1981).

[40] J. Kastner *et al.*, Chemical Physics Letters **221**, 53 (1994).

[41] K. Sato *et al.*, Chemical Physics Letters **427**, 117 (2006).

Chapter 3

Photoexcited Carbon Nanotubes

The photoexcitation of carbon nanotubes combined with Raman spectroscopy can be applied to investigate the temperature induced changes in optical and electronic properties. Photoexcitation can increase the temperature and leads to thermal expansion. As a result vibrational frequencies are influenced by temperature change. This means temperature change can be observed by spectral changes of vibrational bands. This is particularly useful for nanotubes where it is difficult to measure temperature due to their small size. In this chapter we explore laser heating effects on different types of double wall carbon nanotubes by using Raman Stokes and antiStokes spectra at several excitation wavelengths. The effect of laser power change is also studied on DWCNT which have been freeze dried.

3.1 The Effect of Temperature On Phonons: A literature Review

The vibrational amplitude of the atoms or molecules become large with the increase of the material temperature. At larger amplitudes the oscillator deviates from a simple harmonic motion. Deviation from simple harmonic motion is then called anharmonicity and the harmonic oscillator becomes anharmonic oscillator. For anharmonic oscillators, the force and the displacement are not linearly related and the oscillation frequency changes with change in amplitude. The anharmonicity can be calculated by perturbation theory. Anharmonicity induces a modification of the frequency. Temperature induced frequency shifts measure the anharmonicity [1]. Temperature changes the phonon population leading to lattice parameter variations attributed to anharmonicity [1]. The

temperature dependent variations in the half width at half maximum of the Raman band can be attributed to optical phonon decay into two or three acoustic phonons.

The temperature dependent Raman spectra of diamond, single crystalline graphite and highly oriented pyrolytic graphite has been studied in great detail in the past [2–6]. The temperature variation also leads to changes of the elastic modulus. Lattice expansion with increasing temperature leads generally to a decrease of the elastic modulus [7]. The shift in phonon modes by thermal expansion of crystal is a volume effect. In general, the phonon mode shift can be expressed as

$$d\omega = \left(\frac{\partial \omega}{\partial T}\right)_V dT + \left(\frac{\partial \omega}{\partial V}\right)_T \left(\frac{\partial V}{\partial T}\right)_P dT \qquad (3.1)$$

Both volume and temperature effects cause a change in the Raman band position. Diamond, graphite and carbon nanotubes, have a high thermal conductivity and do not show considerable in-plane thermal expansion [8, 9]. The changes in phonon frequencies by temperature influences the electronic properties and electron phonon coupling. Thus thermal Raman shifts of carbon nanotubes reflect also the effect of temperature on electronic properties. Experimental [10, 11] and theoretical [12, 13] studies have shown the influence of temperature on the band gap of semiconducting carbon nanotubes.

According to the Grüneisen model, the relative frequency change $(\Delta\omega/\omega)$ is directly proportional to the relative volume change $(\Delta V/V)$

$$\frac{\Delta\omega}{\omega} = -\frac{\Delta V}{V} \times \gamma \qquad (3.2)$$

or

$$-\frac{\Delta\omega}{\omega} \times \frac{V}{\Delta V} = \frac{d\ln\omega}{d\ln V} = \gamma \qquad (3.3)$$

where γ is called Grüneisen constant. However, it has also been reported that with temperature variations, the ratio of the relative change in frequency to the relative change in volume is not equal to γ [14].

Table 3.1: *The temperature coefficients for D, G, and 2D bands for for different forms of carbon. The numbers in square brackets are the references in the bibliography. The thermal coefficient reported for diamond are 0.012 [2] and 0.007 [3].*

Material	$(d\omega/dT)_D$	$(d\omega/dT)_G$	$(d\omega/dT)_{2D}$
	(cm^{-1}/K)	(cm^{-1}/K)	(cm^{-1}/K)
Graphite		-0.022 [15]	
		-0.030 [16]	
	-0.019 [17]	-0.028 [16]	
		-0.024 [18]	
Graphene		-0.016 [19]	-0.034 [19]
SWCNT	0.014 [20]	-0.022 [15]	
	0.013 [21]	-0.03 [21]	
	0.019 [22]	-0.0305 [23]	
		-0.031 [24]	
		-0.022 [25]	
		-0.038 [16]	
		-0.042 [16]	
		-0.028 [26]	
DWCNT	0.015 [20]	-0.023_o [27]	
		-0.045_i [27]	
	0.015 [21]	-0.026 [21]	
	-0.024 [28]	-0.024 [28]	
MWCNT	-0.018 [22]	-0.028 [16]	
		-0.023 [18]	
	-0.017 [29]	-0.025 [29]	-0.028 [29]

In highly ordered pyrolytic graphite no increase of temperature with the increase of laser power is observed [15] while Au-ion implanted HOPG show a increase in temperature with laser power [16]. The laser induced temperature increase is found to be less in purified SWCNT compared to unpurified SWCNT [16]. The laser induced temperature increase in carbon nanotubes can therefore be used to detect disorder and impurities.

The down shifts of Raman RBM and G mode of SWCNT with increase of laser power and from thermostat heating reported by Li *et al.* [16] are shown in figure 3.1. The down shifts of the RBM and G modes induced by thermostat heating are found identical to those observed by laser power. The solid and dashed lines in the figure 3.1 are linear least square fits. The thermal coefficient for the G band is larger than thermal coefficient for RBM band. The curvature in the tube gives a radial component of the restoring force when stretching the C-C bonds and this radial component of the restoring force is proportional to

the curvature.
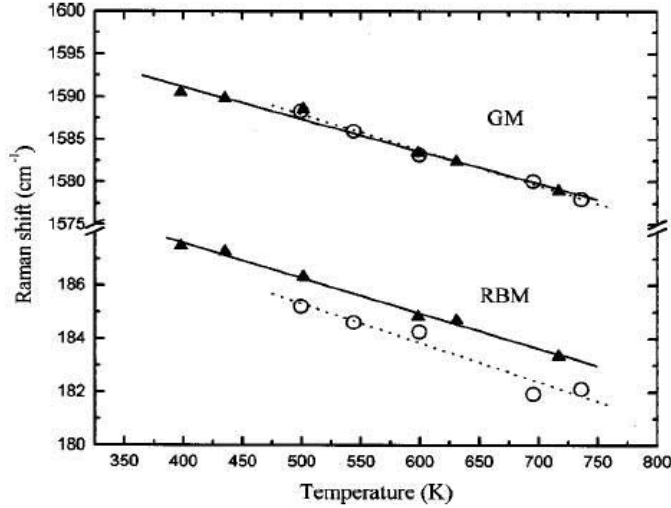
Figure 3.1: *Temperature dependence of the frequencies of the RBM and G band for SWCNT heated by laser (symbol ▲ and solid fitted lines) and by a thermostat (Linkam TH600 stage) (symbol O and the dashed fitted line) [16]*

Table 3.2: *Slopes and intercepts of the fitted straight line for the GM and RBM of the SWCNT in figure 3.1 [16].*

	Raman mode	Laser heating	Stage heating
Slope ($10^{-2} cm^{-1}/K$)	G	-3.8	-4.2
	RBM	-1.3	-1.5
Intercept cm^{-1}	G	1606	1609
	RBM	193	192

It has been reported that with increasing temperature $\sim$ to 700K, the RBM bands retain their initial peak shapes and the frequency shift is linearly to lower frequencies [13, 16, 30]. In contrast it has also been reported that there is considerable change in the line shapes of RBM bands with the downshift with increasing temperature from 150K to 610K [31]. Narrowing of the line shape of the RBM bands with increasing temperature has been also reported [32]. The different temperature dependence can be explained by the large variety of carbon nanotubes available.

Increase in temperature increases the anharmonic component and phonon-phonon interaction. Anharmonicity reduces the force constants. The Raman spectra reflects these effects by broadening of bands, lowering of intensity and spectral down shifting of bands.

The G$^+$ frequencies vary for different SWCNT samples [24]. However, the G$^+$ frequencies for different samples with different excitation wavelengths show the same temperature dependence of Raman shift (figure 3.2). Thus temperature of SWCNT can be measured by observing the change in Raman shift of the G$^+$ band. The three phonons scattering process is considered to be mainly responsible for the temperature dependent shift of the G$^+$ band [8]. The G$^-$ band shows different frequencies for different laser excitation wavelengths and has a different temperature dependence. The reason for this is that the G$^-$ band position is diameter dependent. For different laser lines, different diameter tubes are in resonance and as a result the temperature shift depends on laser energy [24].
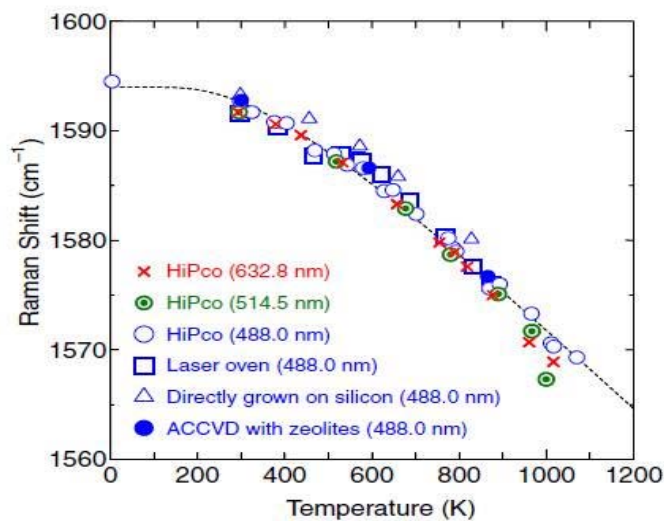
Figure 3.2: *Temperature dependence of Raman shift of the G$^+$ peak for various SWCNT samples measured with the 488.0 nm excitation laser and for HiPco samples measured with three different excitation lasers (488.0, 514.5, and 632.8 nm). The dashed line represents the fit with empirical law $\Omega = \Omega_\circ - C/(exp(D\hbar\omega/kT) - 1)$ [24](C = 61.14 cm^{-1} and D = 0.787)*

The intensity of the defect induced D band is used to estimate the quality of carbon nanotubes [33]. Heating of SWCNT in air increases the intensity of D band while in vacuum no significant change is observed. The change of intensity by heating in air is attributed to oxidation of the nanotubes [34].

The interaction of the walls in DWCNT by van der Waals interaction may give rise to additional Raman band [35] called interlayer interaction band. However, the van der Waals interactions does not affect the main vibration mode of inner and outer tubes corresponding to SWCNT and depends on diameter. Thus RBM bands of DWCNT in first approximation can be assigned with the same rules which apply for SWCNT [36, 37]. The band positions and line

shapes of Raman bands of DWCNT depend again on the laser energies due to resonance [38]. Raman spectra of DWCNT exhibit splitting of the G band at higher frequency. The splitting reduces with increasing external-tube diameter [39]. The nanotubes of large diameter have a higher downshift in frequency as shown in figure 3.3.
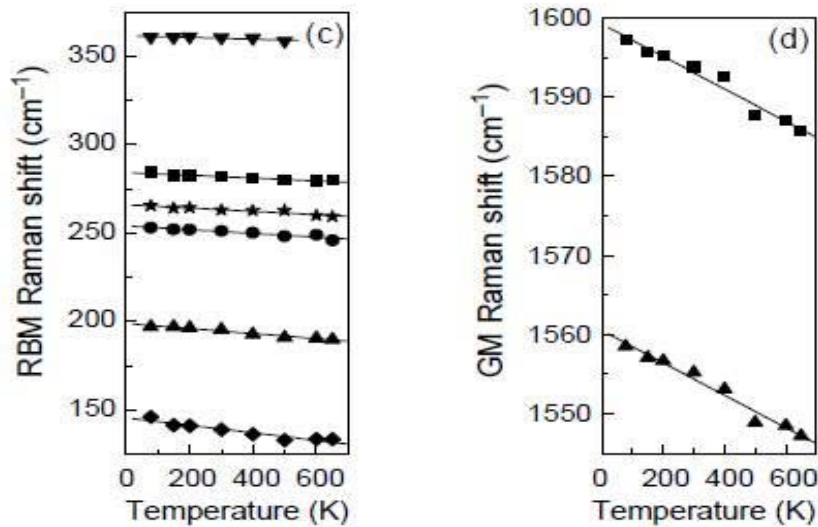
Figure 3.3: *Temperature dependence of the frequencies of the RBM (c) and GM (d) for the DWNTs [37]*

The variation in the C-C stretching force constant with temperature is smaller for small diameter carbon nanotubes leading to a smaller Raman frequency down shift [37].

The G mode of DWCNT are due to the overlap of tangential vibrations from outer and inner tubes [21]. This broader distribution makes the G band broad comparing to the G bands of SWCNT. The change of excitation wavelength changes the band frequencies and intensities due to dependence on resonance conditions which depends on excitation wavelengths [21].

The D mode band down shifts with increase in temperature [21]. The down shift is dependent on laser power. The down shift in the D band is equal to or less then the G band down shift. For MWCNT, the peak width of D mode can be used to estimate the amount of impurities and defects present in the sample [40].

The increase in temperature of MWCNT reduces the D band and G band width, down shift D band(-0.017 cm^{-1}/K) and G band(-0.025 cm^{-1}/K) and decreases the I_D/I_G ratio leading to more graphitized MWCNT by reducing the number of defects [29]. The I_D/I_G ratio using a given excitation wavelength

indicates the relative density of defects and impurities. A smaller I_D/I_G ratio with laser heating reflects a decrease in the density of defects [41]. The reduction in defects due to heating may be due to removal of adsorbed organic impurities and oxidation of non-tubular carbon materials [29]. Graphitized MWCNT show more resistance to oxidation as compared to defective MWCNT. The temperature dependent shifts of G mode for MWCNT lies between the shifts for SWCNT and graphite [29].
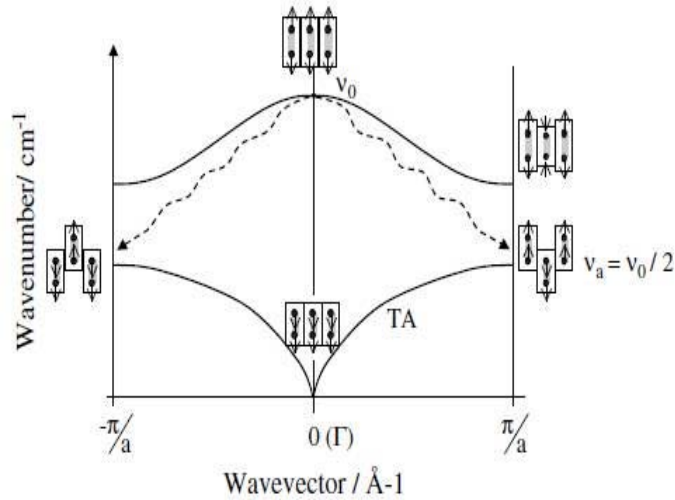
Figure 3.4: *Illustration of an optical phonon decay into acoustic phonons. The conservation of energy is obtained by choosing $\nu_{acc(q=\pi/a)} = 1/2\nu_{opt(q=0)}$. These phonons are in a linear assembly of diatomic molecules where atoms vibrate perpendicular linear axis [1]*

.

The intensity of the Raman scattered light changes with temperature. The creation of phonons (Stokes) or annihilation of phonons (antiStokes) depends on phonon population. At thermal equilibrium, the phonon population in the lattice is given by the Bose-Einstein distribution:

$$n_o(\omega_o, T) = \frac{1}{e^{(\hbar\omega_o/kT)} - 1} \tag{3.4}$$

where ω_o is the frequency of the phonon, k is the Boltzman constant and T is the lattice temperature. The temperature of the sample can be determined by two methods using Raman spectroscopy:

1- By observing the change in Raman frequency of the radial breathing mode or the G band with temperature. Several studies have indicated the temperature induced variations in the RBM and G band [16, 32, 42, 43]. These changes in Raman shift are given by the temperature coefficient ($\frac{\Delta\omega}{\Delta T}$). The an-

harmonicity, cause of the temperature shift, is due to volume effects $(\Delta\omega/\Delta V)_T$ and temperature effects $(\Delta\omega/\Delta T)_V$. Due to small thermal expansion coefficient of carbon nanotubes, the volume effect is insignificant [13]. Thus pure temperature effect is considered to be mainly responsible for the temperature dependent Raman spectra of single wall carbon nanotubes [13]. For single wall carbon nanotubes, the G^+ and G^- bands down shift and broaden with increasing laser power [26].

The optical phonon decays into two equal energy acoustic phonons. The energy of each acoustic phonon is equal to the half of the energy of optical phonon and two acoustic phonons have linear momentums opposite to each other. The HWHM of optical phonon having frequency ω_o is given as [44].

$$\Gamma(\omega_o, T) = \Gamma_o \left[1 + 2n(\omega_o/2, T) \right] \tag{3.5}$$

where n represents the Bose-Einstein factor. For temperature range 300K to 1500K, HWHM variation can be linearly approximated by the relation

$$\Delta\Gamma = \Gamma_o \times 0.00146\Delta T \tag{3.6}$$

From the equation (3.6) and the temperature coefficient can be calculated as [26]

$$\frac{d\omega}{dT} = \frac{d\omega}{d\Gamma} \times \Gamma_o \times 0.00146 \tag{3.7}$$
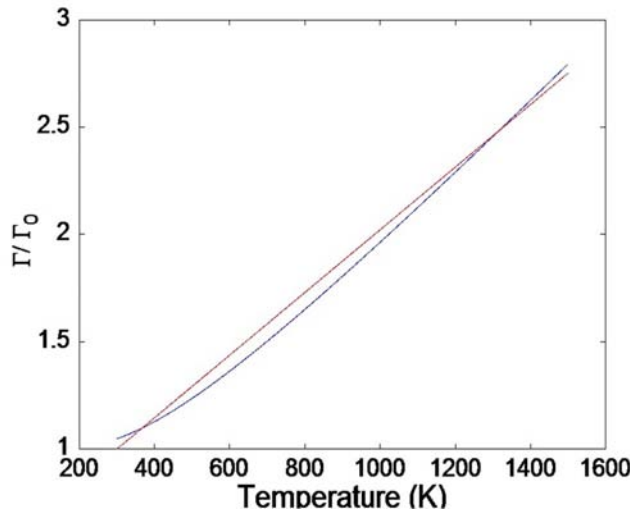
Figure 3.5: Γ/Γ_o *as function of temperature from* (3.5) *and with linear approximation by* (3.6)

By observing the HWHM variation of phonons and the thermal coefficient of the Raman shift ($\frac{\Delta\omega}{\Delta\Gamma}$) the temperature of the sample can be calculated [26].

$$\Delta T = \left(\frac{\Delta T}{\Delta\omega}\right)\Delta\omega \tag{3.8}$$

2- The temperature of the carbon nanotubes by Raman spectroscopy can be obtained by taking the ratio of antiStokes and Stokes intensities [45].

$$\frac{I_S}{I_{AS}} = F\frac{n_o(\omega_o, T) + 1}{n_o(\omega_o, T)} = Fe^{(\hbar\omega_o/kT)} \tag{3.9}$$

By assuming $F \approx 1$, we can write

$$\frac{I_S}{I_{AS}} \approx e^{(\hbar\omega_o/kT)} \tag{3.10}$$

From the equation (3.11), one can find the approximate temperature of the sample during photoexcitation.

3.2 Experiments for Temperature of DWCNT Synthesized by Peapods and CCVD at Four Different Laser Lines

The DWCNT synthesized from CCVD and transformed from peapods are influenced by environment differently. This may be due to different interlayer distance between the the inner and outer wall or having different impurities or defects in both cases. DWCNT synthesized by CCVD due to use of catalysts has higher impurities compared to DWCNT transformed from peapods. We have conducted a Raman study to investigate and compare the temperature of the two samples at four laser excitation wavelengths (468 nm, 530 nm, 568 nm and 647 nm) by Stokes and antiStokes intensity ratio of the G band. The temperature obtained are then compared with the temperature values determined by shift in Raman G band spectral position when laser power is changed by the factor of 20. The synthesis of DWCNT prepared by the catalytical chemical vapor deposition method (CCVD) is reported in reference [27]. For the double wall carbon nanotubes obtained by the transformation of peapods, the SWCNT used for filling of C_{60} have been prepared [46] by the electric arc discharge method with graphite anodes doped with Ni and Y as catalysts to enhance the efficiency in the growth of nanotubes under the similar regular conditions reported in reference [47]. The produced nanotubes was purified by steps which includes sulphuric acid treatments, heat treatments in air, regular mild-heat-based drying procedures, and a final 1000 °C heat-treatment

in vacuum to remove surface chemicals functions brought by the purification
treatment [46]. The SWCNT are 80% purified and are available commercially
from NANOCARBLAB(Russia) [46].

The figure 3.6 shows the Stokes-antiStokes spectra with four laser wave-
lengths 468 nm, 530 nm, 568 nm and 647 nm for DWCNT transformed from
peapods. In the Temperatures shown in figure 3.6 are calculated by antiStokes
and Stokes intensity ratio of the G band Raman spectra.

$$\frac{I_S}{I_{AS}} = F e^{(\hbar \omega_o / kT)} \tag{3.11}$$

where F is constant with the assumption of F = 1.
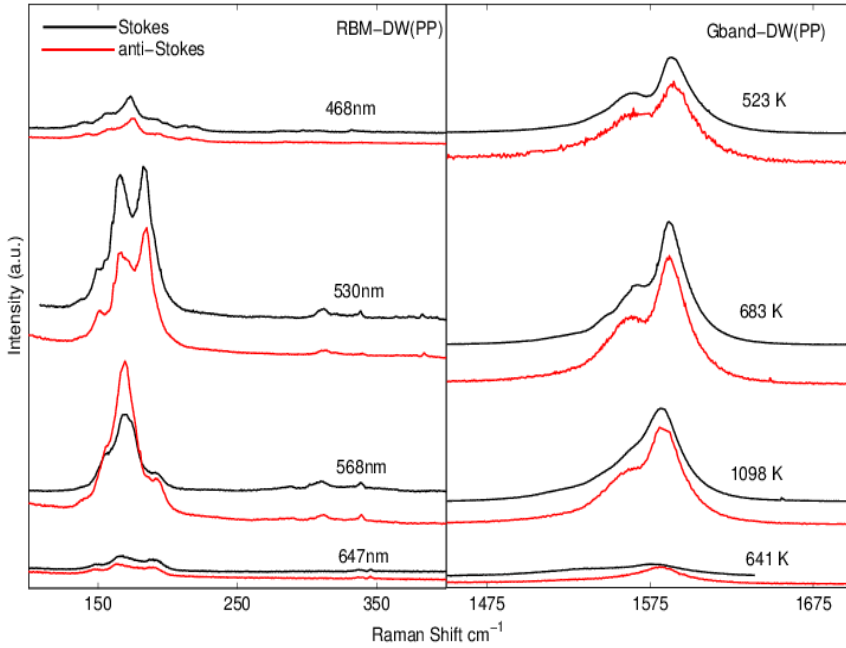
Figure 3.6: *The Stokes-antiStokes spectra with four laser wavelengths 468 nm, 530
nm, 568 nm and 647 nm for DWCNT(peapods). The temperatures are calculated by
Stokes and antiStokes intensity ratio of G band.*

The figure 3.7 shows the Stokes-antiStokes spectra with four laser wave-
lengths 468 nm, 530 nm, 568 nm and 647 nm for DWCNT synthesized from
CCVD. Temperatures shown in figure 3.7 are calculated by Stokes and antiS-
tokes intensity ratio of the G band Raman spectra.
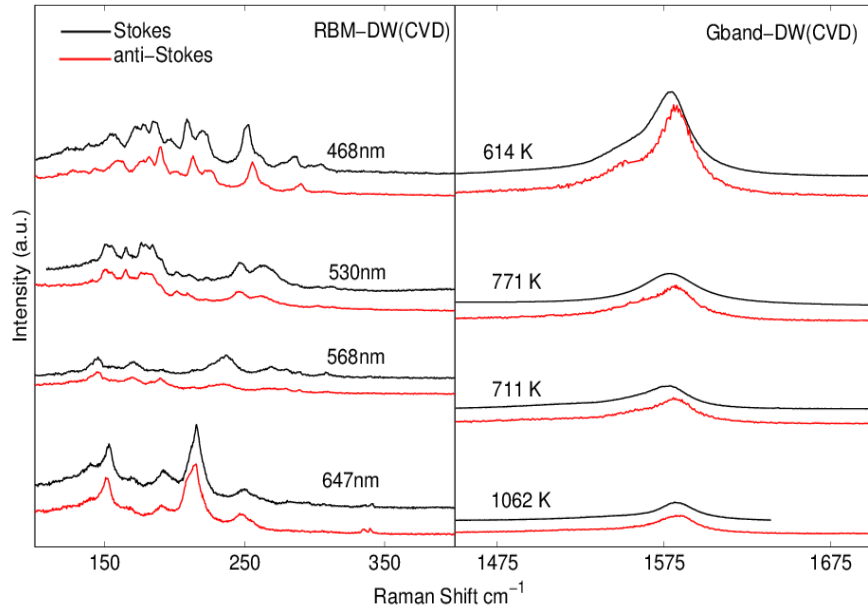
Figure 3.7: *The Stokes-antiStoke spectra with four laser wavelengths 468 nm, 530 nm, 568 nm and 647 nm for DWCNT(CVD). The temperatures are calculated by Stokes and antiStokes intensity ratio of G band.*

The table below indicates the estimated temperature values by $\frac{I_S}{I_{AS}}$ ratio (eq: (3.11))and their differences for two types of DWCNT at four wavelengths.

Table 3.3: *The estimated temperature values by $\frac{I_S}{I_{AS}}$ ratio (eq: (3.11)) for two types of tubes and their differences for four laser wavelengths 468 nm, 530 nm, 568 nm and 647 nm.*

Laser wavelength λ (nm)	T_{PP} (K)	T_{CVD} (K)
468	523	614
530	683	771
568	1098	711
647	641	1062

The temperature of DWCNT(CCVD) is higher than that of DWCNT(PP) for 468 nm, 530 nm and 647 nm. This concludes that double wall carbon nanotubes synthesized from CCVD method have higher photo absorption than double wall carbon nanotubes obtained by peapods.

Now we shall report the temperature values calculated by the change of Raman G band spectral position when the laser power is changed by 20 times.

The figure 3.8 shows the Raman spectra of two types of DWCNT when laser
power is changed by 20 times for four laser wavelengths 468nm, 530nm, 568nm
and 647nm. The black line is for higher power and red line is for lower power.

The difference of peak positions($\Delta\omega$) indicated in the figure 3.8 is due to
change in power by 20 times. We calculate the temperature change for the
power level shifts with the $\Delta\omega = \alpha\Delta T$. The thermal coefficient for Raman
shift of DWCNT is taken from literature [28] which is -0.024 cm^{-1}/K.
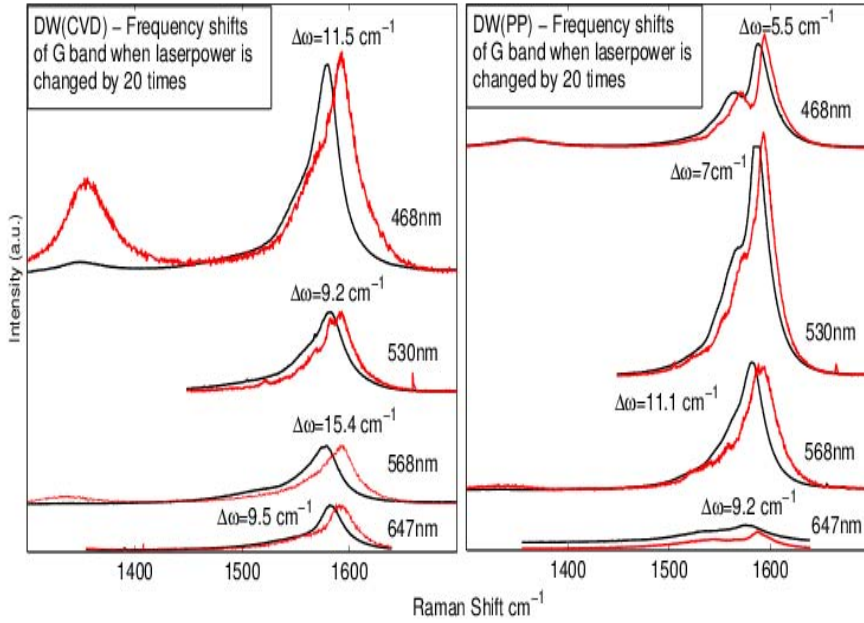
Figure 3.8: *The comparison of two types of DWCNT at two laser power levels for
four laser wavelengths 468 nm, 530 nm, 568 nm and 647 nm. The difference of two
powers is 20 times along with the difference of peak positions at two laser powers*

Table 3.4: *The change in temperature values for two types of tubes and their differ-
ences for four laser wavelengths 468 nm, 530 nm, 568 nm and 647 nm when power
is changed by 20 times.*

λ nm	$\Delta\omega$(DW-PP) cm^{-1}	$\Delta\omega$(DW-CVD) cm^{-1}	ΔT (DW-PP) K	ΔT (DW-CVD) K
468 nm	5.5	11.5	229	479
530 nm	7	9.2	292	383
568 nm	11.1	15.4	462	642
647 nm	9.2	9.5	383	396

The table 3.4 show the corresponding temperature changes for peak position variation when the laser power is changed by a factor of 20. The DWCNT synthesized from CCVD show larger laser power induced temperature variations compared to DWCNT from peapods.

The table 3.5 gives the comparison between the temperatures calculated for two types of DWCNT with Stokes-antiStokes intensity ratio and by spectral position shift with laser power variation. From the above comparison it is observed that temperature calculated by the two methods are not the same. This is due to assumption of taking F (constant) = 1 in equation (3.11). The resonance effects should be taken into account. Nevertheless, it is rough approximation. Without Breit-Wigner-Fano shape, the accuracy is less then 30%.

Table 3.5: *The comparison of temperature calculated by Stokes-antiStokes intensity ratio and by change in spectral position with laser power variation by 20 times for four laser wavelengths 468 nm, 530 nm, 568 nm and 647 nm.*

λ nm	$T_{S/AS}$(DW-PP) K	$T_{\Delta\omega}$ (PP) K	$T_{S/AS}$(DW-CVD) K	$T_{\Delta\omega}$ (CVD) K
468 nm	523	529	614	779
530 nm	683	591	771	683
568 nm	1098	762	711	941
647 nm	641	683	1062	695

3.3 Published Experimental Results of Photoexcited Double Wall Carbon Nanotubes
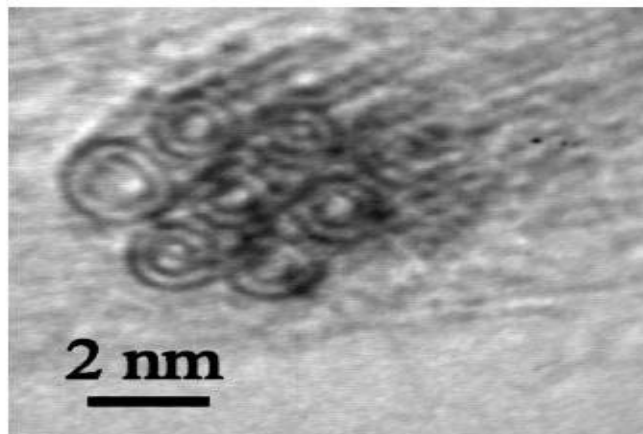
Figure 3.9: *Bundle of DWCNT observed by high-resolution transmission electron microscopy [48]*

Here we report the experiments and results from the paper which we published
in Physical Review B 79 (085418) 2009. In this paper, we compare D and G
band shifts by changing the temperature in a methanol heat bath and as a
function of laser power in air. Differences in spectral shifts of the D and G
bands of nanotubes in air are then compared with Stokes (S) and antiStokes
(AS) spectra recorded as function of laser irradiation. We also compare the
Raman intensity for double wall carbon nanotubes in the red spectral region
and in the UV spectral region with the laser power increase.

DWCNT used in experiment have been prepared by the catalytical chemical
vapor deposition method (CCVD) as reported in reference [27]. High-resolution
electron microscopy of DWCNT in bundles indicates the diameters are from 0.6
to 3.0 nm range as shown in figure: 3.9. Raman spectra have been recorded
using three excitation wavelengths 633 nm, 647 nm, and 338 nm. We compare
spectra recorded with two different spectrometers(Renishaw and Dilor XY
visible) working in the visible spectral range to detect possible differences in
the spectrometer characteristics which depends on grating and microscope used.
We measured a spectral error smaller than 0.05 cm^{-1} by mapping the strained
silicon and fitting the optical phonon band. All phonon bands have been fitted
with a Lorentzian line function.

We have used methanol in heat bath for thermalization of DWCNT with
thermostat. Agglomerated DWCNT sample in the form of pieces are immersed
in methanol without sonication.
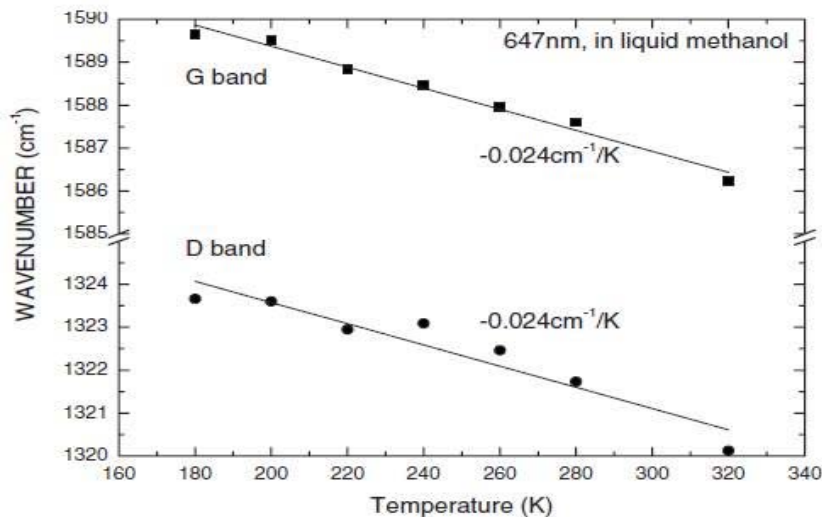
Figure 3.10: *D and G band positions of DWCNT in methanol as a function of
temperature [48].*

The spectral D and G band positions changes uniformly at different locations

of the sample at low laser power (1 mW/μ m^2). We have recorded the Raman spectra at different temperatures ranging from 180 to 320 K using a cryostat. The D and G band spectral positions are obtained by fitting the recorded spectral bands with Lorentzian function. Figure 3.10 shows the temperature dependent D and G band spectral positions from 180 to 320 K.

We observed that both the D and G bands shift to lower energies at the same rate with increasing temperature. The temperature shift coefficient (figure 3.10) measured from the linear fit of D and G band frequencies is -0.024 cm^{-1}/K [28, 43]. During the photoexcitation of carbon nanotubes in methanol, the optical absorption by the DWCNT increases the local temperature and the liquid in which tubes are immersed. When the temperatures reaches to the boiling point of methanol (65 °C), vaporization takes place and the agglomerated DWCNT drift out of the focal point. Thus for CNT in methanol, the laser power applied is limited to the boiling point. The thermal shift coefficient of the D and G bands Raman shift is consistent with the earlier reported values. For suspended tubes a similar temperature dependent linear shift of G band with temperature coefficient (-0.022 cm^{-1}/K) has been reported [25]. Chiashi et al [24] has measured RBM and G band from 100 to 1000 K at three different laser wavelengths in visible region and found a similar temperature coefficient of the G band (-0.031 cm^{-1}/K) in the linear range, i.e., from 300 K to 1000 K temperature.
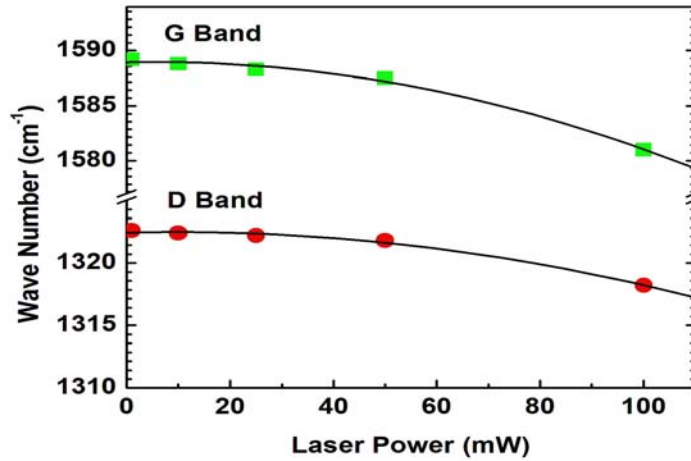
Figure 3.11: *DWCNT wave number versus the laser power (633 nm) [48].*

For photoexcitation of DWCNT in air, we have irradiated DWCNT with increasing laser power from 1 mW to 100 mW at 633 nm excitation wavelength. Photo absorption leads to considerable heating of the DWCNT which depends strongly on wavelength of the incident beam [43] and is limited by the oxidation

of the tubes. The down shifts of Raman modes induced by laser power increase
are found similar to those observed by thermostat heating [16]. Excitation with
a shorter wavelength leads to a large increase in temperature at constant laser
power. In the lower laser power range from 1 mW to 10 mW at 633 nm laser
line, the G band shifts by less than 1 cm^{-1} corresponding to temperatures close
to room temperature. The spectral G band positions at 1 mW and at 10 mW
are 1589.2 cm^{-1} and 1588.8 cm^{-1} respectively. At higher laser powers when
laser irradiation is increased we find that the spectral shifts for the D and G
bands are nonlinear and different for the two bands as reported in figure 3.11.

To understand the differences in the spectral down shifts of the D and G
bands due to heating of tubes by photo absorption in air or heating in a ther-
mostat, we have recorded Stokes and antiStokes spectra. AntiStokes Raman
spectra for graphite, graphitic whiskers [49], MWCNT [50], and SWCNT [51]
have been analyzed in detail. The antiStokes spectrum is reduced by a factor
of 2000 when compared to the Stokes spectrum at room temperature consid-
ering the Bose-Einstein factor with $\omega = 1600 cm^{-1}$. The weak and less intense
antiStokes spectrum at room temperature makes it difficult and challenging
to obtain spectra far from the Rayleigh line [52]. To observe the temperature
change with increasing laser power we recorded Stokes and antiStokes spectra
at 50 and 100 mW as shown in figure 3.12. The spectra recorded at 100 mW
laser power have D and G bands shifted to lower energy when compared to the
spectra recorded at 50 mW due to stronger laser heating. We find that the G
band down shift is nearly two times as large as the D band down shift for both
Stokes and antiStokes spectra with changing laser power from 50 and 100 mW.
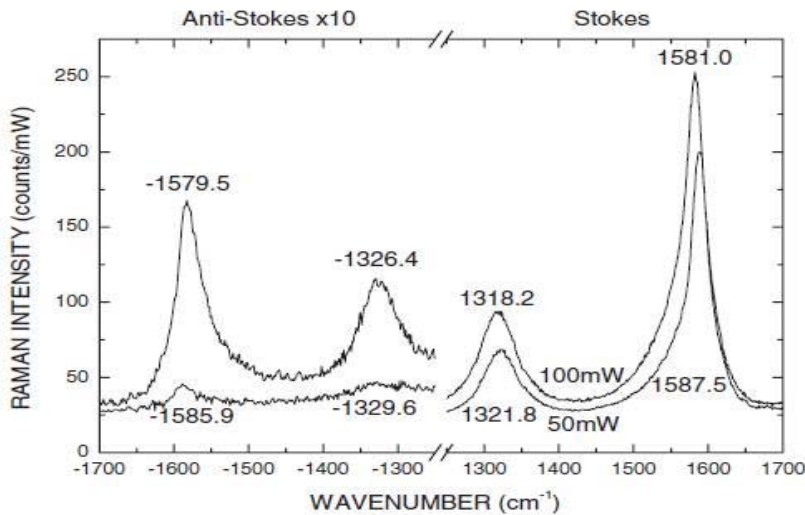
Figure 3.12: *Raman spectra of DWCNT recorded with 50 and 100 mW (633 nm).
The spectra are scaled to the incident laser power. The antiStokes spectra have been
multiplied by a factor of 10 [48].*

This different D band and G band spectral shifts shows that there is a fundamental difference of laser heating for defect induced phonon mode (D band) and G band at higher laser power. We compare the Stokes and antiStokes spectra by assuming that the temperature induced shifts of the electronic levels is negligible in contrast to the width of electronic resonance profile for the G band. The lower limit of the resonance profile for isolated suspended tubes is 80 meV [10]. While for temperature induced shifts of the electronic transitions, we expect 3 meV/100 K for the E_{11} transition [53] which is significantly smaller than resonance profile for isolated suspended tubes. Brown et al [54] have investigated in detail the antiStokes RBM spectra of SWCNT and demonstrated that the spectra on the Stokes and antiStokes sides correspond to tubes of different chiralities or helicities due to the different resonant conditions for Stokes and antiStokes spectra.

DWCNT compared to SWCNT, the coupling between the walls and large size diameter distribution broaden the G band resonance. The ratio of the Stokes and antiStokes spectra eliminate the common factors in the spectra.

$$\frac{\frac{I_S}{I_{AS}}(T_{100mW})}{\frac{I_S}{I_{AS}}(T_{50mW})} = \frac{e^{\hbar\omega/(k_B T_{100mW})}}{e^{\hbar\omega/(k_B T_{100mW})}} = e^{1.44\omega[(1/T_{100mW})-(1/T_{50mW})]} \qquad (3.12)$$

where T is in K and ω in cm^{-1}.

We further eliminate the ω^4 factor and the electronic contributions present in the spectra by taking the ratio of the ratio of the Stokes and antiStokes spectra at two laser powers (50 mW and 100 mW) represented by equation (3.12). It is assumed that the temperature distribution is homogenous. We can deduce the difference of the inverse temperatures from the above equation (3.12)). The values for difference in inverse temperatures for D and G band are shown in table: 3.6 and are approximately equal. Table: 3.6 also shows the

Table 3.6: *Parameters deduced from the S and AS spectra in figure 3.12*

Values	D band	G band
$\frac{1}{T_{50mW}} - \frac{1}{T_{100mW}}$ (S/AS)	-8.57×10^{-4}K^{-1}	-8.65×10^{-4}K^{-1}
$\omega(T_{50mW}) - \omega(T_{1mW})$(S)	-0.8 cm^{-1}	-1.7 cm^{-1}
$\omega(T_{100mW}) - \omega(T_{1mW})$(S)	-4.4 cm^{-1}	-8.2 cm^{-1}

frequency down shift for D and G band at two laser powers(50 mW and 100 mW) from 1 mW. The D band shift is significantly smaller compared to the G band shift both at 50 and 100 mW as shown in table: 3.6. The difference

in inverse temperatures is then calculated with the measured frequency down shifts of the D and G bands as reported in table: 3.6. We also find that the intensity variation in the G and D band are similar as obtained by taking the ratio of the integrated intensities of the G and D bands in deducing the difference of the inverse temperatures.

The inverse temperature for the G band deduced from the band shift is close to the value obtained from the ratio of the Stokes/antiStokes spectra while for the D band the corresponding value is 30% lower.

This demonstrates that the D band position is influenced by laser irradiation. The ratio of the two spectra recorded at different laser power gives the opportunity to compare the differences in the D and G band positions attributed to differences in phonon temperature with the temperature deduced from the ratio of the Stokes and antiStokes spectra.

This shows that laser induced changes for G and D band are different. Differences in phonon temperature due to nonequilibrium phonons would, however, imply changes in the relative D and G band intensities. Laser irradiation can leads to the creation of a larger number of excitons. The presence of excitons modifies the electronic and the local tube structures. When recording laser power dependent Raman spectra of different types of tubes (SWCNT, MWCNT, and doped MWCNT), we find no uniform shift of the D and G bands; $\Delta\omega_D/\Delta\omega_G$ varies between zero to one. At 468 nm and for DWCNT, $\Delta\omega_G = 12.5 cm^{-1}$ while $\Delta\omega_D = 6.0 cm^{-1}$, for SWCNT $\Delta\omega_G = 8.5 cm^{-1}$ while $\Delta\omega_D = 3.5 cm^{-1}$, and for nitrogen-doped MWCNT, the D band remains unaffected while G band downshifts. With UV excitation, we find that the G and D bands are the same for SWCNT. While the G band shifts are consistent with the corresponding Stokes/antiStokes spectra, the D band shift is nonuniform at high laser irradiation. D band shifts are not only attributed to temperature variations but also appear to be connected to the presence of excitons. The other possible reason for different D and G band shifts is that G band is possibly coming from cylindrical tube vibrations while the D band is evolved from the defects at the edges of the tube. Apart from the nonlinear shifts of the D and G bands with laser irradiation, Figure 3.12 shows that the intensity of the two bands is superlinear when increasing the laser irradiation.

To explore the differences in the resonance conditions for different excitation wavelengths, we have compared the power scaled intensity of the G band for DWCNT. Figure 3.13 shows the variation in the integrated intensity of the G band as a function of laser power excited at 647 and 338 nm. We find that the normalized intensity as a function of laser power follows a power law. The Raman intensity is smaller when excited at 338 nm compared to 647 nm excitation laser line. The same is observed when using a different spectrom-

eter (Renishaw at 633 nm) to exclude the influence of detector response and spectrometer performance. When excited at 647 nm, the integrated intensity increases superlinearly ($I = I_o P^{1.8}$) while when excited at 338 nm, the intensity increases sublinearly ($I = I_o P^{0.85}$). Sublinear behavior can be explained by heat induced broadening of the electronic bands due to strong absorption in the UV spectral range which reduces the Raman cross section. Superlinear behavior can be explained by participation of excitons in the resonance process as observed in strained GaAs [55, 56], or by exciton screening resulting in changes in the joint density of states.
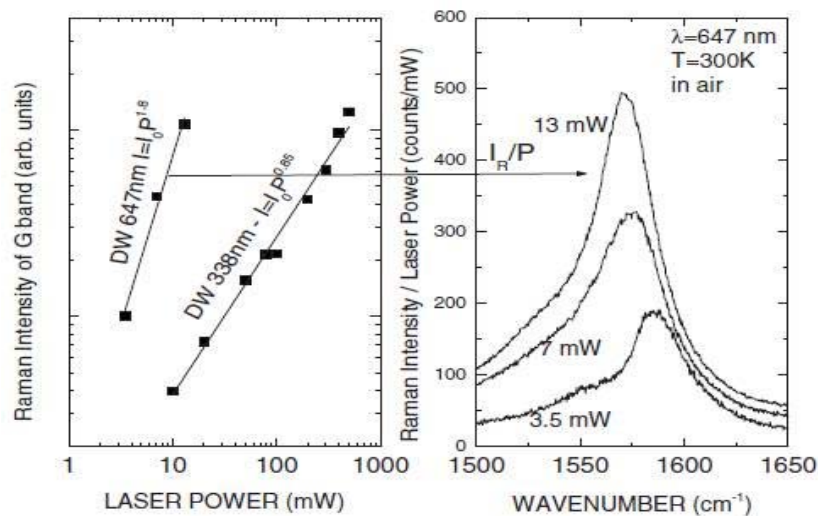
Figure 3.13: *Raman intensity as a function of laser power. Excitation wavelength of 647 nm [48].*

3.4 Experimental Results of Photoexcitation of Lyophilized and Non-Lyophilized DWCNT

Carbon nanotubes samples produced by different methods often contain impurities like catalyst particles, amorphous carbon and other by products. These impurities present can be removed by acid treatment. Then neutral water is used to wash the sample to eliminate the acid traces. The remains of water present are quenched by drying process. The dry sample of carbon nanotubes can be applied for dispersion in polymers or for storage purposes. The nanotubes samples obtained by regular drying have limitation on the dispersion of tubes in polymers or in solutions. Freeze drying process instead of regular drying by thermal vaporization is reported to reduce the limitations on processability and dispersion of CNT [46]. Freeze-drying is a process to remove water(dehydration) from the material also known as lyophilization or cryodessi-

cation. Lyophilization is done in the following steps: *1*-Freezing the material so that the water in the material is converted into ice. *2*- Pressure is reduced as well as heat is provided so that water present as ice in material is directly changes into water vapor. *3*- Removal of water vapors. *4*- After the removal water vapors, lyophilized material is taken out from the machine.
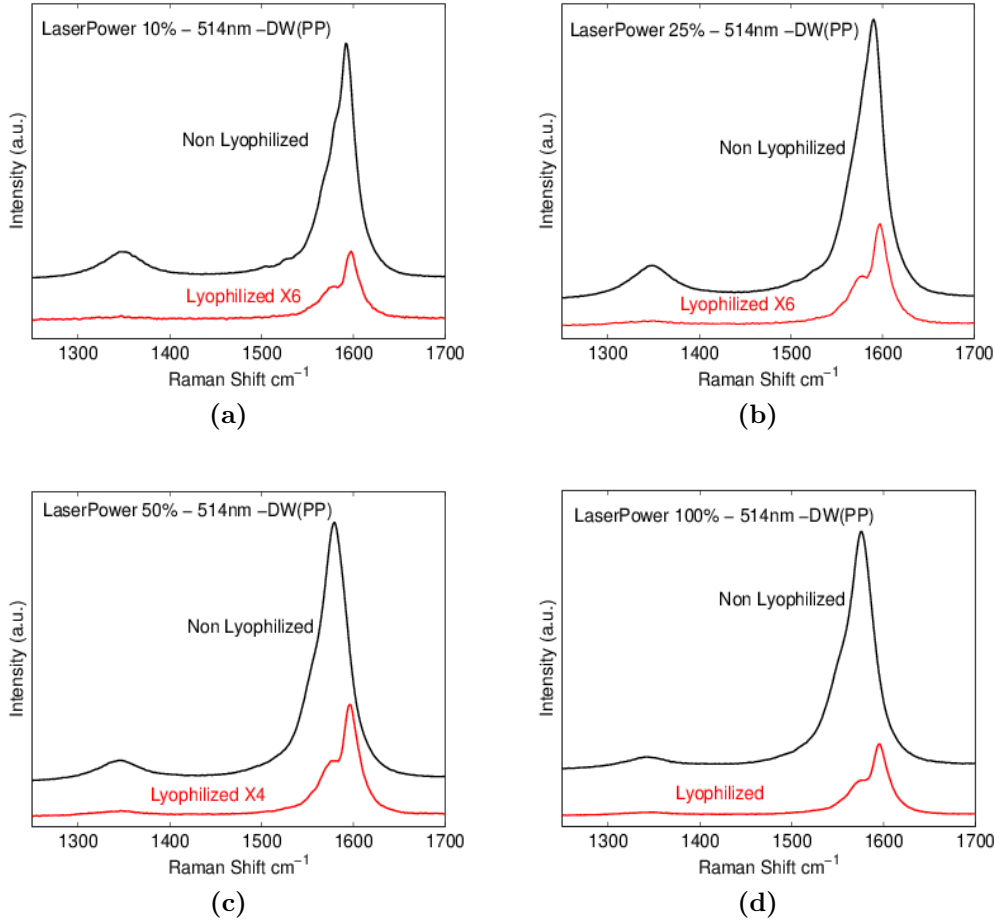
Figure 3.14: *D and G band of lyophilized and non-lyophilized DWCNT synthesized by peapods at 514 nm excitation wavelength at four different laser powers*

Here we report the comparative photoexcitation study of lyophilized double wall carbon nanotubes transformed from peapods and tubes processed by regular drying process (We term it as non-lyophilized DWCNT) by Raman spectroscopy. This study will help to characterize the lyophilized DWCNT under strong photoexcitation and environmental effects with laser heating.

The double wall carbon nanotubes used are obtained by the transformation of peapods. The SWCNT used for filling of C_{60} have been prepared [46] by

the electric arc discharge method using graphite anodes doped with Ni and Y as catalysts enhance the efficiency in the growth nanotubes under the similar regular conditions reported in reference [47]. One batch of as produced nanotubes was purified by steps which includes sulphuric acid treatments, heat treatments in air, regular mild-heat-based drying procedures, and a final 1000 °C heat-treatment in vacuum to remove surface chemicals functions brought by the purification treatment [46]. The SWCNT are 80% purified and are available commercially from NANOCARBLAB (Russia). Another batch of the same raw SWCNT was purified with the same method but the regular drying steps were replaced by a freeze-drying [46].

Figure 3.14 shows the Raman D and G band spectra for lyophilized DWCNT and non lyophilized DWCNT at different laser powers with 514 nm excitation wavelength.
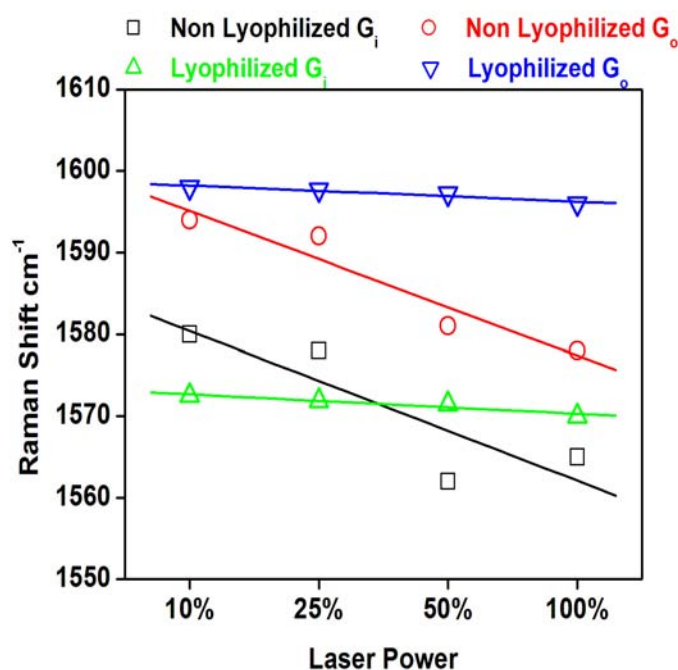
Figure 3.15: *G band spectral positions with linear fit of lyophilized and non-lyophilized DWCNT synthesized by peapods at 514 nm excitation wavelength at four different laser powers*

The figure 3.15 shows the laser power dependent for G band of inner and outer tubes for non-lyophilized and lyophilized DWCNT. The lyophilized tubes are less sensitive to laser induce heating as the down shift with the increase in laser power is very small compared to non-lyophilized tubes. Thus lyophilized tubes absorb less light and are less sensitive to irradiation.

3.5 Conclusion

We observed clear differences in the D and G band Raman shifts at high photon irradiation of carbon nanotubes. Comparison with the Stokes and antiStokes spectra show that the D band shift is reduced at high photon irradiation and depends on tube type. Superlinear and sublinear intensity increases in the phonon bands with laser power are observed when using excitation in the red and UV spectral range, respectively, and attributed to participation of excitons in the double-resonance process and heat induced broadening of the electronic bands due to strong absorption.

The comparison of lyophilized and non lyophilized DWCNT synthesized from the transformation of peapods show that lyophilized are more robust to laser induced heating effects compared to non lyophilized. Thus among the three types of DWCNT, tubes synthesized from CCVD are more prone to temperature induced effects then to non lyophilized and lyophilized tubes obtained by the peapods transformation. Lyophilized tubes are least affected by the laser induced heating.

Bibliography

[1] G. Lucazeau, Journal of Raman Spectroscopy **34**, 478 (2003).

[2] E. S. Zouboulis and M. Grimsditch, Physical Review B **43**, 12490 (1991).

[3] H. Herchen and M. A. Cappelli, Physical Review B **43**, 11740 (1991).

[4] P. H. Tan, Y. M. Deng, Q. Zhao, and W. C. Cheng, Applied Physics Letters **74**, 1818 (1999).

[5] P. Lespade, R. Al-Jishi, and M. S. Dresselhaus, Carbon **20**, 427 (1982).

[6] P. H. Tan, Y. M. Deng, and Q. Zhao, Physical Review B **58**, 5435 (1998).

[7] T. Skipa, Ph.D. thesis, von der Fakultt fr Physik der Universitt (TH), Forschungszentrum Karlsruhe GmbH Postfach 3640, 76021 Karlsruhe, (2006).

[8] Y. Maniwa *et al.*, Physical Review B **64**, 241402 (2001).

[9] Y. Maniwa *et al.*, Physical Review B **64**, 073105 (2001).

[10] C. Fantini *et al.*, Physical Review Letters **93**, 147406 (2004).

[11] S. N. Bokova *et al.*, Quantum Electronics **33**, 645 (2003).

[12] R. B. Capaz *et al.*, Physical Review Letters **94**, 036801 (2005).

[13] N. R. Raravikar *et al.*, Physical Review B **66**, 235424 (2002).

[14] R. S. Krishnann, Proceedings of the Indian Academy of Sciences, Section A **24**, 45 (1946).

[15] F. M. Huang *et al.*, Journal of Applied Physics **84**, 4022 (1998).

[16] H. D. Li *et al.*, Applied Physics Letters **76**, 2053 (2000).

[17] J. Sandler *et al.*, Physical Review B **67**, 035417 (2003).

[18] Y. Ouyang and Y. Fang, Physica E: Low-dimensional Systems and Nanostructures **24**, 222 (2004).

[19] I. Calizo *et al.*, Applied Physics Letters **91**, 071913 (2007).

[20] Z. H. Ni *et al.*, Journal of Raman Spectroscopy **38**, 1449 (2007).

[21] S. Osswald, E. Flahaut, and Y. Gogotsi, Chemistry of Materials **18**, 1525 (2006).

[22] M. Terrones *et al.*, Science **288**, 1226 (2000).

[23] A. Jungen *et al.*, *MEMS 2008 Tucson : 21st IEEE International Conference on Micro Electro Mechanical Systems* (IEEE, New York, 2008), pp. 733–736.

[24] S. Chiashi, Y. Murakami, Y. Miyauchi, and S. Maruyama, Japanese Journal of Applied Physics **47**, 20102015 (2008).

[25] I. K. Hsu *et al.*, Applied Physics Letters **92**, 063119 (2008).

[26] P. Puech *et al.*, Physical Review B **76**, 054118 (2007).

[27] E. Flahaut, R. Bacsa, A. Peigney, and C. Laurent, Chemical Communication 1442 (2003).

[28] P. Puech *et al.*, Journal of Raman Spectroscopy **38**, 714 (2007).

[29] S. Osswald and M. H. Y. Gogotsi, Journal of Raman Spectroscopy **38**, 728 (2007).

[30] L. Ci *et al.*, Applied Physics Letters **82**, 3098 (2003).

[31] A. Jorio *et al.*, Physical Review B **66**, 115411 (2002).

[32] Q. Zhang *et al.*, Smart Materials and Structures **15**, S1 (2006).

[33] A. C. Dillon *et al.*, Chemical Physics Letters **401**, 522 (2005).

[34] D. Kang, M. Hakamatsuka, K. Kojima, and M. Tachibana, Diamond and Related Materials **19**, 578 (2010).

[35] Y. Kwon and D. Tomànek, Physical Review B **58**, R16001 (1998).

[36] R. Saito *et al.*, Chemical Physics Letters **348**, 187 (2001).

[37] S. S. Xiea *et al.*, Science and Technology of Advanced Materials **6**, 725 (2005).

[38] L. J. Ci *et al.*, Journal of Applied Physics **94**, 5715 (2003).

[39] A. Rahmani, J. L. Sauvajol, J. Cambedouzou, and C. Benoit, Physical Review B **71**, 125402 (2005).

[40] T. Nakamiya *et al.*, Thin Solid Films **in press**, (2010).

[41] T. Nakamiya *et al.*, Current Applied Physics **8**, 400 (2008).

[42] Z. Zhou *et al.*, Journal of Physical Chemistry B **110**, 1206 (2006).

[43] A. Bassil, P. Puech, L. Tubery, and W. Bacsa, Applied Physics Letters **88**, 173113 (2006).

[44] P. G. Klemens, Physical Review B **11**, 3206 (1975).

[45] G. E. Jellison, D. H. Lowndness, and R. F. Wood, Physical Review B **28**, 3272 (1983).

[46] M. Maugey *et al.*, Journal of Nanoscience and nanotechnology **7**, 2633 (2007).

[47] C. Journet *et al.*, Nature **388**, 756 (1997).

[48] P. Puech *et al.*, Physical Review B **79**, 085418 (2009).

[49] P. H. Tan *et al.*, Physical Review B **64**, 214301 (2001).

[50] P. H. Tan *et al.*, Physical Review B **66**, 245410 (2002).

[51] J. Maultzsch, S. Reich, and C. Thomsen, Physical Review B **70**, 155403 (2004).

[52] P. Puech *et al.*, Physical Review B **73**, 233408 (2006).

[53] D. Karaiskaj *et al.*, Physical Review Letters **96**, 106805 (2006).

[54] S. D. M. Brown *et al.*, Physical Review B **61**, R5137 (2000).

[55] A. Alexandrou, C. Trallero-Giner, G. Kanellis, and M. Cardona, Physical Review B **40**, 1013 (1989).

[56] Y. Liu, R. Sooryakumar, E. S. Koteles, and B. Elman, Physical Review B **45**, 6769 (1992).

Chapter 4

Nitrogen and Sulphuric Acid Doped Carbon Nanotubes

The electronic and optical properties of carbon nanotubes can be changed by moving the Fermi level and add new electronic states with doping. The first part of the chapter describes the Raman study of undoped and nitrogen doped multiwall carbon nanotubes and carbon nanofibers. Nitrogen doped carbon nanofibers used in this study are synthesized by the pyridine and acetonitrile precursors. The Raman observations are also compared with transmission electron microscopy, X-ray photoelectron spectroscopy and elemental analysis. We also study the difference on undoped and doped samples by varying the laser power. In the second part we present the investigations for sulphuric acid doped double wall carbon nanotubes by Raman spectroscopy and by high pressure Raman spectroscopy. First, with Raman spectroscopy, we discuss the difference of sulphuric acid (H_2SO_4) doping effect on the internal and external wall in DWCNT synthesized with CCVD method. Later on, we combine the sulphuric acid doping and high pressure. We study the nanoscale structure of H_2SO_4 around the nanotubes by using different concentrations of sulphuric acid.

4.1   Introduction

The band gap and density of states of carbon nanotubes changes with the change in diameter and chirality. The variation of diameter and chirality gives different electronic and mechanical properties of carbon nanotubes [1, 2]. The sample of nanotubes as produced has diameter and chirality distribution having metallic as well as semiconducting nanotubes together and this limits the

physical and chemical properties [3]. These limitations can be avoided by introduction of atoms or molecules from different elements and compounds like boron or nitrogen in carbon nanotubes by increasing the conductivity of the semiconducting nanotubes present in the sample. The electronic properties of the carbon nanotubes can be changed by moving the Fermi level and is a better route to tailor the nanotubes according to required applications [4]. For example, the field emission property of CNT can be improved with boron or nitrogen doping. The Fermi energy position E_F with respect to van Hove singularities in carbon nanotubes can be changed by chemical [5] or electrochemical doping [6]. Incorporation of nitrogen in bulk graphite structures results disorder in the graphene planes and can introduce curvature in graphene layers by promoting the pentagon [7].

Doping can create defects or chemically activate sites on the surface of carbon nanotubes which can help to catalytical active deposition on the surfaces of tubular carbon structures [8–10]. Controlled defects and presence of hetero atoms in carbon nanotubes have high impacts in technological applications [11–14]. For example, the possibility of spatially localized doping can enhance the probability of complete device construction within a single nanotube.

Sulphuric acid (H_2SO_4) is a strong protonic acid and down shifts the Fermi level upon doping in carbon nanotubes. The double wall carbon nanotubes provides an ideal opportunity to investigate the changes with doping. Raman G band is sensitive to doping and can be used to investigate the doped DWCNT properties by comparing with Raman G band of pristine tubes. The investigations of intrinsic properties and interwall interactions for pure and doped nanotubes can play a main role in understanding their properties and to develop new devices.

The physical properties (thermal conductivity, optical response) of the materials changes with the variation of interatomic distances and physical structure. Pressure can be applied to change the structure and interatomic distances. This can help to explore the relationship between structure and properties of the materials. Thus high pressure techniques can help to understand the structure dependent physical properties of the materials which can be used to improve the design parameters of devices [15, 16]. The vibrational properties of carbon nanotube change when high pressure is applied. The details of structural stability can be extracted from the parameters of Raman peaks of carbon nanotubes under high pressure [16–18]. The G mode frequency increases with the increase in pressure. Large diameter tubes are more affected compared to smaller diameter tubes [17].

The combined effect of chemical doping and hydrostatic pressure separate the contributions from internal and external tubes in DWCNT [19]. The inter-

nal tubes with low doping effect(10%) [20] experience the pressure from outer tube only. So inner tube contributions can be used as a reference [21].

4.2 Types of Doping

There are three main type of doping. *1-* Exohedral doping(Intercalation) *2-* Endohedral doping(Encapsulation) *3-* Substitutional doping (Inplane).
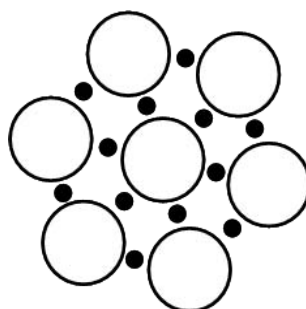
Figure 4.1: *A model representation of exohedral doping. Dots represents the doped atoms or molecules. Open circles represents carbon nanotubes*

Exohedral Doping(Intercalation): The trapping of atoms or molecules in the bundles of carbon nanotubes such that atoms or molecules are intercalated between the outer walls of carbon nanotubes is called exohedral doping as shown in figure 4.1. Electronic properties of the host lattice can be changed by doping with electron donating and electron accepting guest atoms or molecules that reside in the interstitial channels [22]. Nanotubes can act as amphoteric materials by accepting electrons from guest atoms or molecules or by donating electrons to guest atoms or molecules [22].
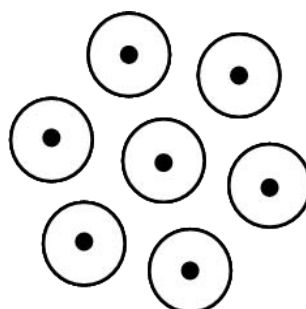
Figure 4.2: *A model representation of endohedral doping. Dots represents the doped atoms or molecules. Open circles represents carbon nanotubes*

Endohedral Doping(Encapsulation): The encapsulation of guest atoms or

molecules inside the core of CNT is called endohedral doping as shown in figure 4.2. Endohedral doping is a capillary behavior of carbon nanotubes [23]. The SWCNT filled with C_{60}(peapods) is an example of endohedral doping. Chemical reactions inside the carbon nanotubes can be performed by encapsulations of reactants inside the tubes, so these can act as nano reactors [4].
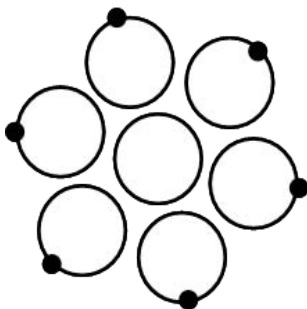
Figure 4.3: *A model representation of inplane doping. Dots represents the doped atoms or molecules. Open circles represents carbon nanotubes/carbon nanofibers*

Substitutional Doping(In-plane): The replacement of C atoms by guest atoms or molecules in the graphene layers of CNT is called substitutional or in-plane doping as shown in figure 4.3.

4.3   Review of Nitrogen Doping in Carbon Nanotubes

Soon after the discovery of carbon nanotubes by Iijima in 1991 [24, 25], the doped carbon nanotubes were studied and doping effects were analyzed in 1993 [26]. The wall configuration can be changed by substitution doping of nitrogen by introducing defects in the graphene layers of tubular nano structures and can change the properties of these nanostructures [27].

For intrinsic doping in carbon nanotubes and carbon nanofibers, nitrogen is considered to be a good candidate because, *1-* The atomic dimensions of nitrogen and carbon are approximately same. The radius of carbon is 0.070 nm while atomic radius of nitrogen is 0.065 nm. C-C (CNT) bond length is 0.142 nm where as C-N bond length is 0.134 nm. *2-* Carbon has four electrons in its valence shell while nitrogen has five electrons in its valence shell. *3-* Nitrogen doping in CNT and CNF is analogous to hetero atom doping in semiconductors [28]. This makes the nitrogen atom suitable for incorporation into graphene layers of carbon nanostructures. The C-N bond length is shorter as compared to C-C bond length. Thus the substitution of nitrogen in graphene layers due to difference in C-N and C-C bond length can change the crystallinity of the

well ordered graphite layers. Quantum confinement effects and curvatures in tubular structures make them to behave differently compared to bulk doped graphite [27].

The properties of carbon structures depends upon the type of hybridization which define the type of carbon atom bonding with neighboring atoms in the structure [27]. Initial studies have indicated the incorporation of nitrogen in carbon structures by thermal annealing at low concentration values (<0.5 at%) [27, 29, 30]. The nitrogen incorporation in amorphous carbon thin films creates internal stress reduction effect [31]. The internal stress reduction effects depends on the sp^2 to sp^3 carbon bonding ratios [27]. These studies are useful for the future analysis giving comparative data for carbon nanotubes and carbon nanofibers because of the limited data available on doped carbon nanotubes [27]. The different types of bonds and concentration of nitrogen doping has been largely understood by the results obtained by bulk doped systems [27].

Nitrogen has an extra electron compared to carbon. It is expected that substitution of nitrogen in carbon nanotubes will act as electron donor showing the n-type semiconductor behavior [32, 33]. The nitrogen doping in MWCNT is complicated because more than one walls present in these structures. Different types of bonding are expected in case of nitrogen incorporation in MWCNT. These different types can be direct substitution, pyridinic type or pyrrolic type. With higher concentration of graphite like nitrogen bonding structures, n-type behavior can be expected as suggested by transport studies of isolated nitrogen doped SWCNT [34]. The Pyridine type induces the localized states below and above the Fermi level and can lead to p-type or n-type conducting behavior of carbon nanotubes depending on the number of nitrogen atoms substituted in the graphene layer [4].

Pyridine configuration based on tight binding and ab initio calculations has been explored by Czerw *et al* [35]. The metallic nature of bamboo like nitrogen doped MWCNT is assumed to be due to the pyridine configuration [35]. Kang and Jeong [32] using density function theory calculations reported that the pyridine configuration of nitrogen in carbon nanotubes is energetically feasible with lone-pair state of electrons.

It is found that the nitrogen concentration is higher in the inner walls of carbon nanotubes and carbon nanofibers [36–38]. The quantity of nitrogen incorporated in carbon nanotubes and the type of nitrogen bonding is defined by the growth parameters [39–42]. For the synthesis of N doped MWCNT most of the efforts were with the intension of achieving high nitrogen percentage incorporation in the MWCNT. High amount of nitrogen incorporation in carbon nanotubes is considered good for high reactivity of carbon nanotubes and for porosity [27]. But the higher amount of doping in nanotubes should not be

the only objective rather controlled doping of nitrogen should be considered for particular applications or for the type of bonds required for specific uses [27].

In the domain of semiconducting materials, high amount of nitrogen doping is not needed rather small amount of nitrogen doping is desired. Similarly superficial defects created by functionalization or surface modifications of carbon nanotubes can help to decrease their chemical inertness and make them more active [27]. Synthesis methods used for pristine nanotubes with some additional parameters and conditions can be used for nitrogen doping of carbon nanotubes which can produce MWCNT with nitrogen contents below 1% to 20% [43]. The nitrogen doped carbon nanotubes do not have the same structure having the hollow core like pristine MWCNT [44]. Nitrogen doped MWCNT shows bamboo like structure having compartments separated by graphitic layers [27]. Coiled structures of high yield nitrogen doped MWCNT is also observed [45]. Analytical techniques like XPS can be used to identify the nitrogen present in the nitrogen doped carbon nanotubes [27].

4.4 Raman Spectroscopy Analysis of Nitrogen Doping

In this study we describe Raman spectroscopy analysis of the following samples *1*- Undoped multiwall carbon nanotubes. *2*- Nitrogen doped MWCNT. *3*- Undoped carbon nanofibers. *4*- Nitrogen doped CNF with pyridine precursor at different deposition temperatures. *5*- Nitrogen doped CNF with acetonitrile precursor at different deposition temperatures. Samples were provided by Jacques Teddy of LCC-ENSIACET, Toulouse in the group of Prof. Philippe Serp. All the samples used in this study are synthesized by catalytic chemical vapor deposition deposition. Transmission electron microscopy(TEM), X-ray photoelectron spectroscopy(XPS) and elemental analysis(E.A.) results are provided by Jacques Teddy(ENSIACET, Toulouse) [46]. The details of synthesis, TEM, XPS and EA can be found in appendix A.

Raman spectroscopy has been successfully applied to obtain information about the physical and electronic structures of different types of carbon nanotubes. So the changes in Raman bands introduced by doping can indicate the changes in physical and electronic structure of the carbon nanotubes. Thus the Raman spectroscopy can be used for characterizing the N doped CNT and CNF to find the physical and electronic structure when compared with undoped tubes and fibers. Raman spectroscopic results generally indicates the down shift of G-band for nitrogen doped CNT along with the increase of I_D/I_G. The increase of I_D/I_G is considered as increase of disorder in the CNT and CNF which can be linked to N doping in CNT [47].

In our study, we have used 302.4nm (UV), 514nm (Green) and 632.8nm (Red) laser excitation except for MWCNT which are excited by 302.4 nm and 514 nm. We have observed the variation of Raman spectra of N doped compared to undoped MWCNT and CNF with the change of excitation energy and tried to find different type of C-N bonds in the samples. The parameters of D band and G band were used to make the conclusion about nitrogen doping in MWCNT and CNF. The effects of temperature with increase of laser power are compared for undoped and doped tubes and fibers by observing changes in the Raman bands.

4.4.1 Undoped and N-Doped MWCNT

Elemental analysis results of nitrogen doped MWCNT indicate the 1.6% nitrogen and TEM micrographs show good graphitic layers. Raman spectra of undoped MWCNT and nitrogen doped MWCNT are shown in figure 4.4 at 302.4 nm and 514 nm laser excitation. The intensity decreases and the spectral position up shifts with doping.
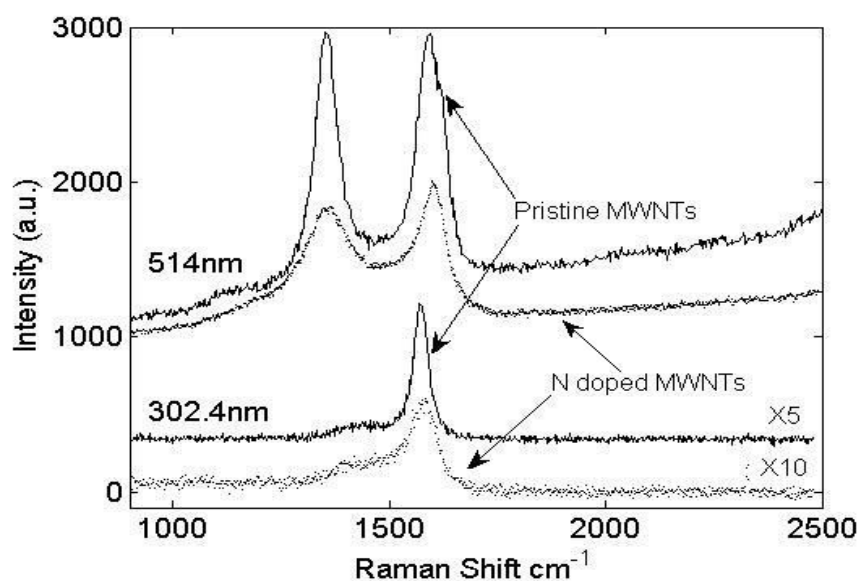
Figure 4.4: *Raman spectra of undoped and N doped MWCNT at two different laser excitation wavelengths(302.4nm and 514nm).*

We have observed the Raman spectra of undoped and doped tubes at four different laser powers. For undoped and N doped MWCNT, the HWHM of the D band and the G band as a function of Raman shift at four different laser powers using the 514 nm laser excitation are shown in figure 4.5.

The D band half width half maximum ($HWHM_D$) of N doped MWCNT is approximately 2.6 times large then undoped tubes indicating dispersion of D band with the doping of nitrogen. Doping of nitrogen in the graphitic layers increases the disorder which can be observed by the increase in line width of D band [40]. The half width at half maximum increase of the D band in our case is consistent with investigations by Yun et al [40]. In the case of $HWHM_G$ of the G band of N doped MWCNT, the increase is small compared to HWHM of the D band.
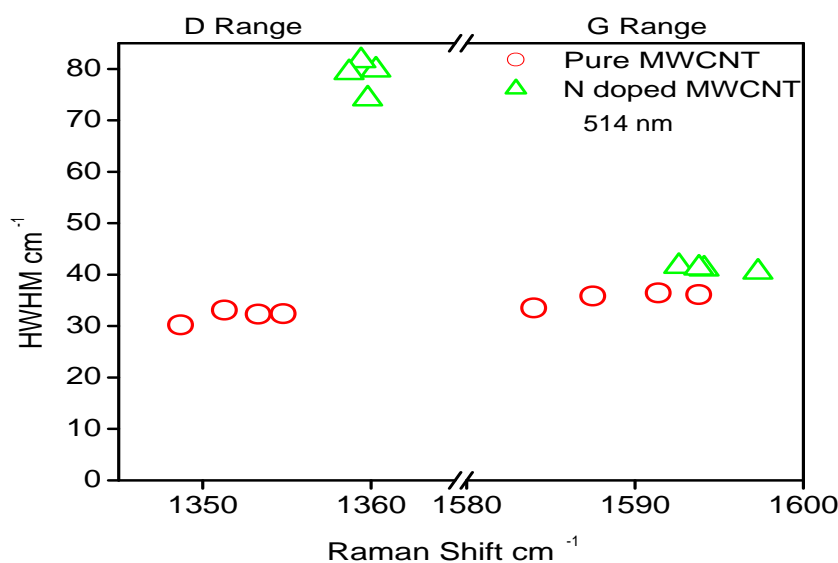
Figure 4.5: *HWHM vs Raman Shift for Pure and N doped MWCNT (514nm). Large broadening of $HWHM_D$ as compare to $HWHM_G$ for N doping indicates the nitrogen is doped in MWCNT*

4.4.2   Undoped and N-Doped Carbon Nanofibers

We have used three laser excitation wavelengths, 632.8 nm, 514 nm and 302.4 nm for Raman spectroscopy of undoped and nitrogen doped CNF. The doped CNF are synthesized from pyridine precursor and acetonitrile precursor. CNF synthesized from pyridine precursor are represented by P1, P2 and P3 at deposition temperatures 750 °C, 650 °C and 600 °C respectively. CNF synthesized from acetonitrile precursor are represented by A1, A2, A3 and A4 at deposition temperature 600 °C, 650 °C, 700 °C and 750 °C respectively.

632.8 nm Laser Excitation Wavelength

Figure 4.6: *Raman spectras of carbon nanofibers (a) synthesized from pyridine precursor (b) synthesized from acetonitrile precursor at 633nm excitation wavelength*

The Raman spectra of undoped CNF and nitrogen doped CNF from pyridine precursor and acetonitrile precursor at laser excitation wavelength 632.8 nm are shown in figure 4.6(a) and figure 4.6(b) respectively. The intensity of D band and G band decreases with nitrogen doping for both pyridine based CNF and acetonitrile based CNF.
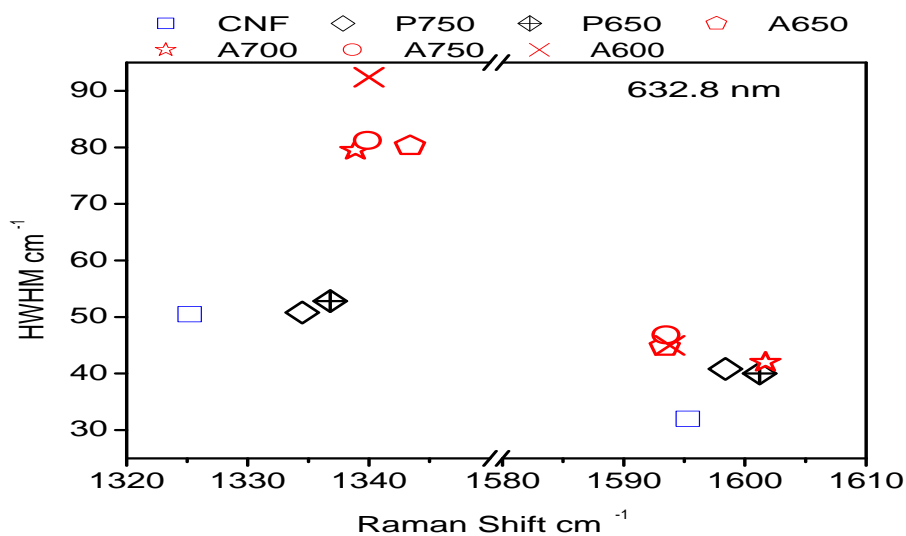
Figure 4.7: *HWHM vs Raman Shift at 632nm for D band and G band*

The figure 4.7 shows the HWHM as a function of D band and G band Raman shift for pure carbon nanofibers, N doped carbon nanofibers synthesized from pyridine precursor and N doped carbon nanofibers synthesized from acetonitrile precursor at 632.8nm laser excitation wavelength.

For pyridine based fibers, there is a upshift of the Raman D and G band. The upshift in the D band is higher compared to the upshift in G band as shown in figure 4.7.

For acetonitrile based doped fibers, there is a upshift of the Raman D and down shift of G band compared to undoped CNF for three out of four samples. For one sample, there is a up shift in the D and G band. The upshift in D band is higher compared to down shift in G band. This shows that nitrogen doping for pyridine and acetonitrile precursors are different.
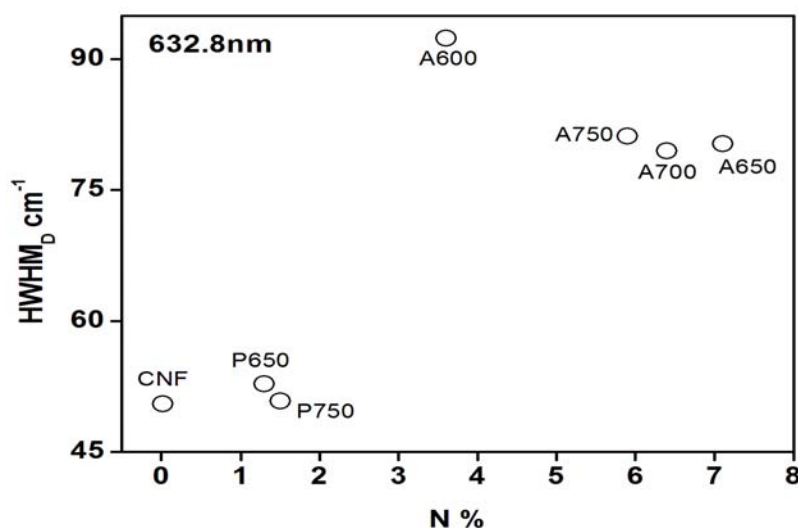
Figure 4.8: *HWHM$_D$ as a function of percentage nitrogen doping for 632nm laser excitation wavelength*

For pyridine based N doped CNF, there is no considerable change in the HWHM of the D band where as HWHM of G band is increased somewhat. For acetonitrile based N doped CNF, there is an increase in the HWHM of the D band where as the HWHM of the G band is increased.

The HWHM$_D$ of N doped carbon nanofibers synthesized from acetonitrile precursor is approximately two times larger than HWHM$_D$ pure carbon nanofibers where as the HWHM$_D$ of N doped carbon nanofibers synthesized from pyridine precursor is approximately equal to HWHM$_D$ of pure carbon nanofibers.

The HWHM$_G$ of N doped carbon nanofibers synthesized from acetonitrile precursor is approximately 1.3 times to 1.6 times larger than the HWHM$_G$ of pure carbon nanofibers where as the HWHM$_G$ of N doped carbon nanofibers synthesized from pyridine precursor is approximately 1.3 times larger than the HWHM$_G$ of pure carbon nanofibers.

HWHM$_D$ as a function of percentage nitrogen doping along with the deposition temperature for 632.8 nm laser excitation wavelength is shown in figure 4.8. The X ray photoelectron spectroscopy and elemental analysis results (Appendix A) shows that doping of nitrogen is higher in acetonitrile based fibers compared to pyridine based fibers. The Raman results also indicates larger values of HWHM$_D$ for acetonitrile based fibers compared to pyridine based fibers. The larger values of HWHM$_D$ represent the increase in disorder with the N increase showing higher doping and is consistent with XPS and EA values represented in figure 4.8.

514nm Laser Excitation Wavelength
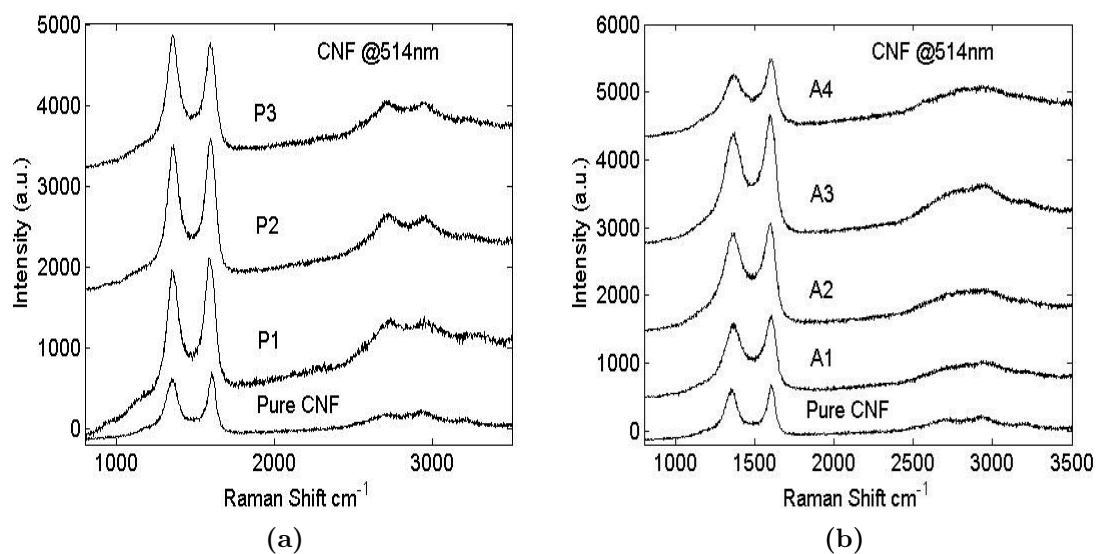
Figure 4.9: *Raman spectras of carbon nanofibers (a) synthesized from pyridine precursor (b) synthesized from acetonitrile precursor at 514nm laser excitation wavelength*

The Raman spectra of undoped CNF and nitrogen doped CNF from pyridine precursor and acetonitrile precursor at laser excitation wavelength 514nm are shown in figure 4.9(a) and figure 4.9(b) respectively. The D band and G band intensity of nitrogen doped fibers (both pyridine and acetonitrile precursors)

have a higher intensity compared to undoped. For pyridine based nitrogen doped fibers, the intensity increase is higher compared to acetonitrile based fibers.

Raman D band upshifts for doped fibers with both acetonitrile based fibers and pyridine based fibers compared to undoped CNF. Upshift of D band is large for acetonitrile based N doped CNF then fibers obtained from pyridine precursor.

The G band is down shifted for N doped pyridine based fibers and acetonitrile based fibers. The downshift of G band for pyridine based fibers are large or approximately equal to the acetonitrile based CNF samples as reported in figure 4.10.
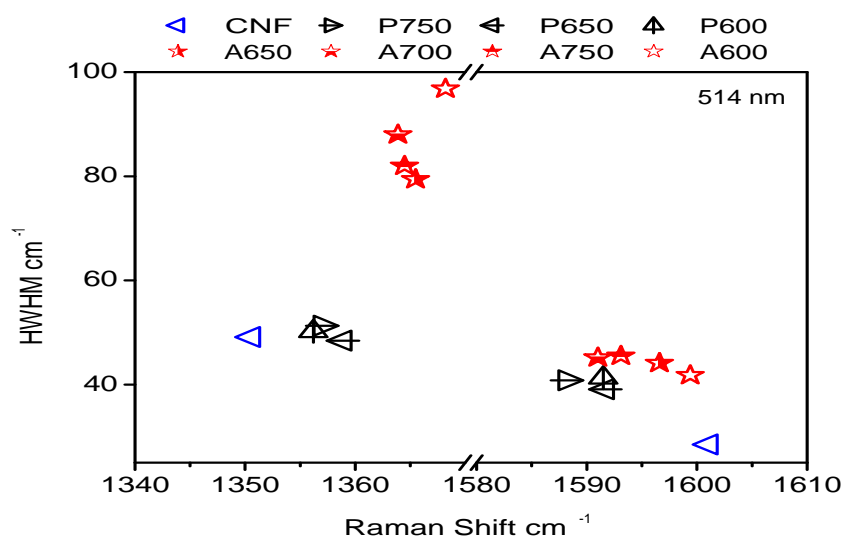
Figure 4.10: *HWHM vs Raman Shift at 514nm for D band and G band*

The figure 4.10 reports the HWHM of Raman D and G band as a function of spectral position of undoped, N doped carbon nanofibers synthesized from pyridine precursor and from acetonitrile precursor.

The $HWHM_D$ of N doped nanofibers synthesized from acetonitrile precursor is approximately two times larger than $HWHM_D$ of undoped where as the $HWHM_D$ of N doped nanofibers synthesized from pyridine precursor is approximately equal to $HWHM_D$ of undoped. The $HWHM_G$ of N doped carbon nanofibers synthesized from acetonitrile precursor are approximately 1.6 times to 1.8 times larger than $HWHM_G$ of undoped while for pyridine precursor $HWHM_G$ is approximately 1.5 times larger then undoped.
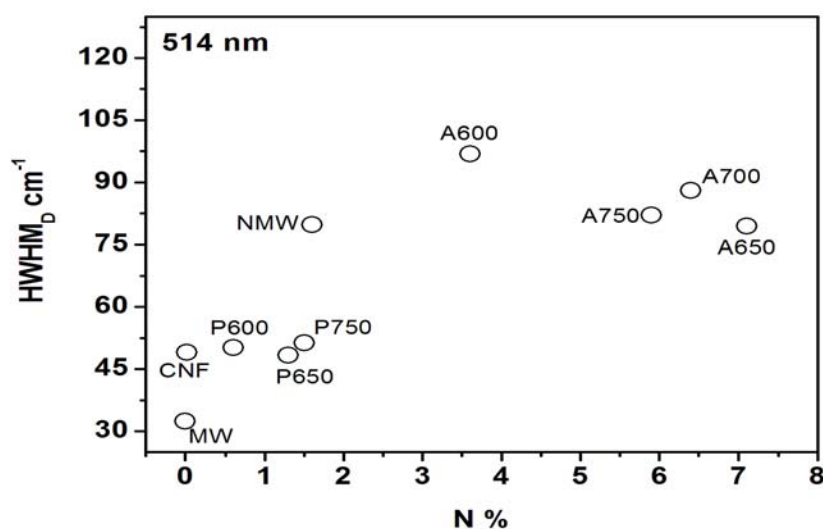
Figure 4.11: *HWHM$_D$ as a function of % nitrogen doping for 514nm excitation wavelength*

Figure 4.11 indicates the HWHM$_D$ as a function of percentage nitrogen doped (Elemental analysis). The nitrogen doped CNF with acetonitrile have higher dispersion of Raman D band at lower temperature. This may be due to more defects at lower deposition temperature for acetonitrile precursor.

302.4nm Laser Excitation Wavelength

The Raman spectra of undoped carbon nanofibers, nitrogen doped nanofibers from pyridine precursor and acetonitrile precursor at laser excitation wavelength 302.4 nm are shown in figure 4.12(a) and figure 4.12(b) respectively. The intensity of D band and G band is reduced for nitrogen doped pyridine based and acetonitrile based carbon nanofibers compared to undoped. The peak height of Raman D and G band is low for pyridine based nitrogen doped nanofibers compared to acetonitrile based.

There is down shift of the Raman D band for two acetonitrile based CNF samples and for one sample it is approximately equal when comparing with pure CNF as show in figure 4.13. For pyridine based N doped CNF, there is a down shift of Raman D band when comparing with pure CNF. For G band there is a up shift for N doped pyridine based CNF and acetonitrile based CNF.
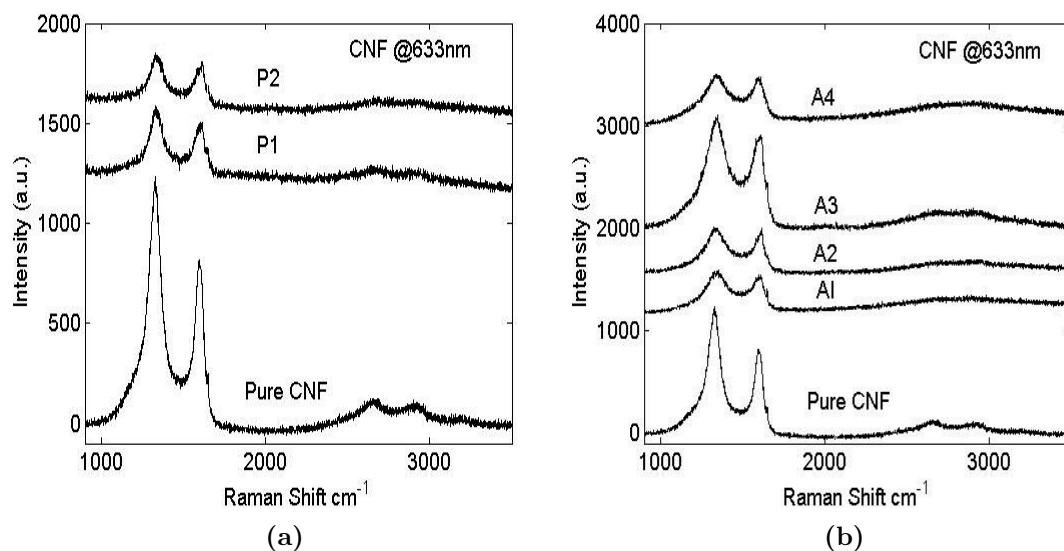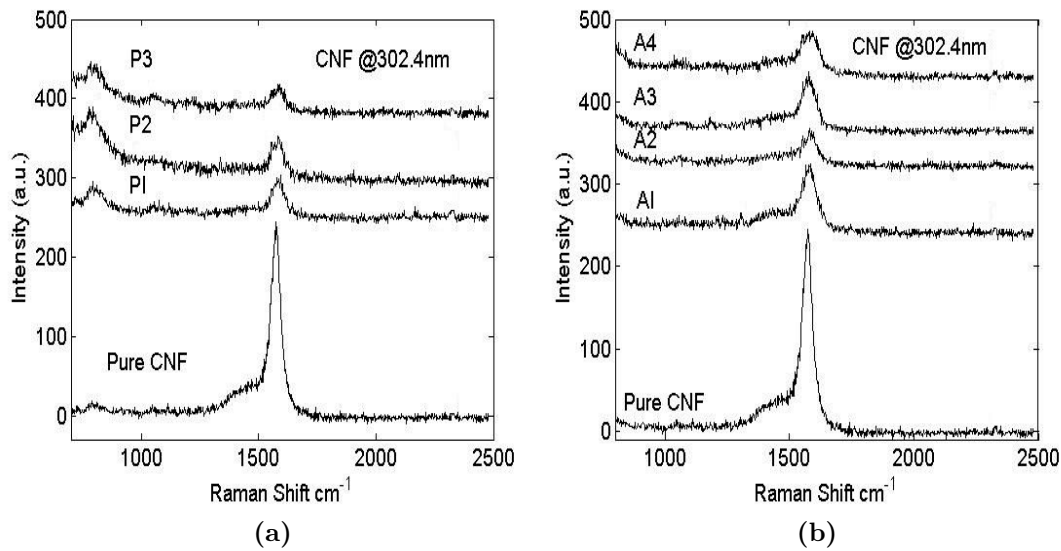
Figure 4.12: *Raman spectra of carbon nanofibers (a) synthesized from pyridine precursor (b) synthesized from acetonitrile precursor at 302nm excitation wavelength*

The $HWHM_D$ of three samples of N doped carbon nanofibers synthesized from acetonitrile precursor is decreased and for one sample, it is increased. The $HWHM_D$ of N doped CNF synthesized from pyridine precursor is decreased.
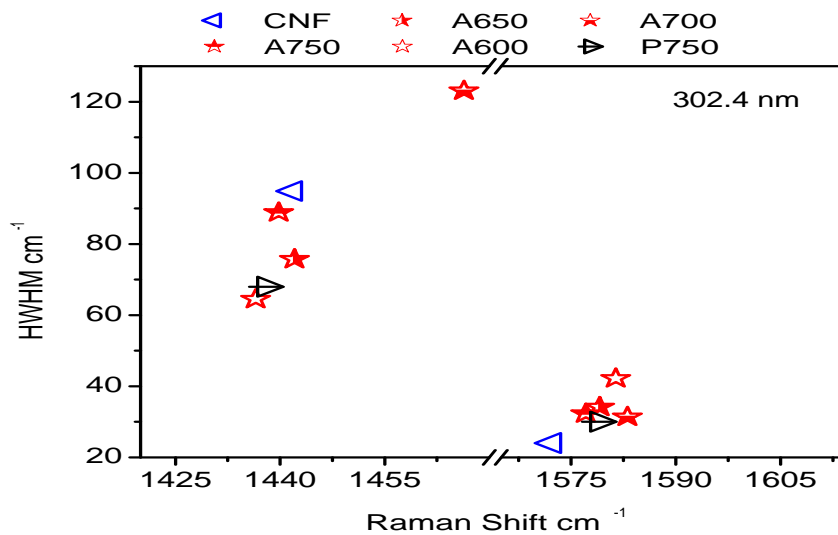
Figure 4.13: *HWHM vs Raman Shift at 302nm for D band and G band*

The $HWHM_G$ of N doped CNF from acetonitrile precursor and from pyridine precursor is increased. From the figure 4.13, the increase of $HWHM_G$ of N doped

CNF from acetonitrile precursor is higher then the HWHM_G of N doped CNF from pyridine precursor when comparing with HWHM_G of pure CNF.
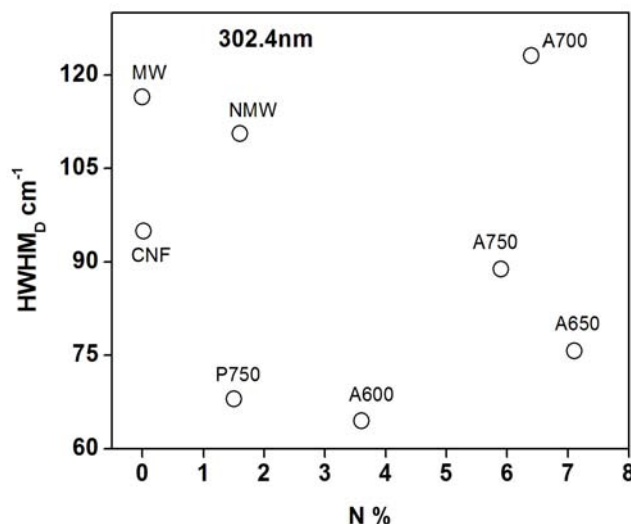
Figure 4.14: *$HWHM_D$ as a function of percentage nitrogen doping for 302.4nm*

HWHM_D as a function of percentage of nitrogen doped for 302.4 nm laser excitation wavelength is shown in figure 4.14. Nitrogen doped CNF with acetonitrile have larger value of line width of Raman D band compared to CNF from pyridine precursor.
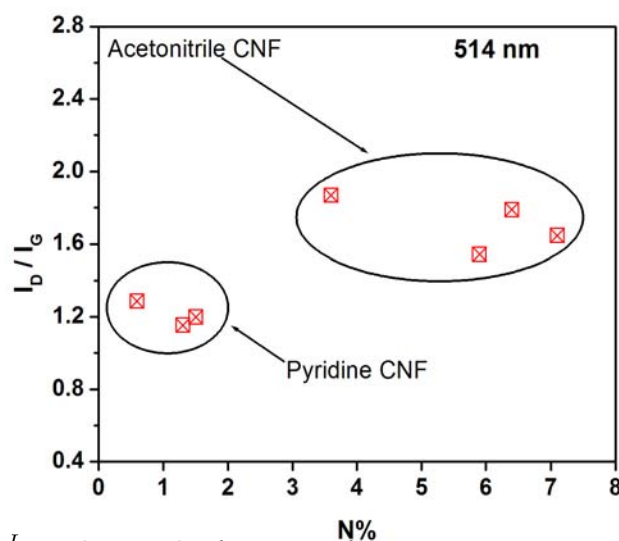
Figure 4.15: *$\frac{I_D}{I_G}$ value as the function of percentage nitrogen doped in carbon nanotubes and carbon nanofibers.*

The large value of the line width of D band indicates the higher value of disorder in the carbon nanotube structure due to nitrogen doping. The XPS and EA shows the higher values nitrogen for acetonitrile based CNF compared to N doped carbon nanofibers synthesized from pyridine precursor. Thus Raman results are consistent with the XPS and EA results.

$\frac{I_D}{I_G}$ is considered a good parameter for estimating the disorder produced in carbon nanotubes and carbon nanofibers by doping. Figure 4.15 gives the $\frac{I_D}{I_G}$ value as the function of percentage nitrogen doped in carbon nanofibers at 514 nm and 632.8 nm. The $\frac{I_D}{I_G}$ values are consistent with elemental analysis results. The $\frac{I_D}{I_G}$ values are low for pyridine based N doped fibers compared to acetonitrile based fibers.

4.5 Review of Sulphuric Acid Doped DWCNT

The sulphuric acid doping induced shifts in the frequency can be divided into two parts as strain induced shifts and charge induced shifts. The G mode of DWCNT have contributions from inner tubes and outer tubes. The inner and outer tubes G mode contributions can be separated by the hydrostatic pressure [19, 48, 49]. Under pressure, the G-mode frequency of internal tube is observed close to graphite G mode where as the G mode of external tube shifts to higher frequencies. High pressure Raman spectroscopy has been used to study effect of high pressure on radial and axial deformation and their consequences on the geometric and electronic structure of CNT [50–52].
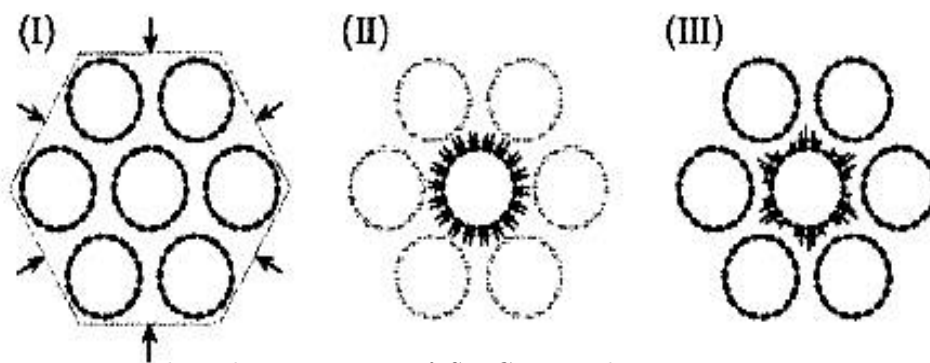
Figure 4.16: *The schematic view of SWCNT under pressure. Figure I, in which the entire bundle with nanotubes arranged in a triangular lattice is subjected to an external compression. Figure II, in which the individual tubes are each compressed symmetrically, and intertubule coupling is ignored. The absence of vdW interactions between the tubes is shown schematically by the lightly shaded tubes surrounding the center tube. Figure III, in which the pressure medium is allowed to penetrate into the interstitial channels between tubes [53].*

The first order RBM and tangential Raman mode under high pressure were first investigated by Venkateswaran et al [53]. To analyze the data, Venkateswaran et al performed the numerical simulations under high pressure using generalized tight binding molecular dynamics (GTBMD) model. Venkateswaran et al used three models to analyze the data of high pressure Raman spectroscopy of SWCNT as shown in figure 4.16.

1: In first model, they considered the uniform external radial compression for the whole bundle considering the van der Waals interaction among the tubes. It is assumed that pressure transmitting medium does not penetrate into interstitial channels in the bundle. The compression of tubes is entirely by external pressure and it makes a little hexagonal deformation in the cross sectional area of the tubes.

2: In second model, symmetric compression of all individual tubes in bundles with the penetration of of pressure transmitting medium inside the interstitial channels between the tubes and without considering van der Waals interaction between the tubes. The force is transmitted to individual tubes through the PTM. The experimental situation is simplified which allow the PTM to exert a symmetric force along the radial direction on each nanotube. This model equally works well for individual nanotube suspended in the pressure transmitting medium.

3: The third model includes the symmetric compression of individual tubes along with the van der Waals interactions among the tubes and penetration of of pressure transmitting medium inside the interstitial channels between the tubes. The individual tubes experience the force by the PTM. The pressure transmitting medium is penetrated in the interstitial spaces around individual nanotubes. The force profile in this model is such that the maximum force is at the center of each interstitial channel and have small hexagonal distortion similar to model I.

Table 4.1: *DWCNT G-band positions, half width half maximum of inner-outer tubes for pressure transmitting medium H_2SO_4 at 633 nm (i: inner tube; o, outer tube) [19]*

PTM	ω_i(P=0) (cm^{-1})	ω_o(P=0) (cm^{-1})	Γ_{i-o}(P=0) (cm^{-1})
H_2SO_4	1587	1618	10

DWCNT have been investigated by applying high pressure Raman spectroscopy using different pressure transmitting mediums [54–56]. The DWCNT G-band positions, half width half maximum of inner-outer tubes for H_2SO_4 as pressure transmitting medium at excitation wavelength 633 nm are shown in

the table 4.1. The effect of different pressure transmitting medium is interpreted as pressure coefficient for inner and outer tube shown in table 4.2. From the slope reported in table 4.2 for H_2SO_4 as pressure transmitting medium, $\Delta\omega_i = 6cm^{-1}$ is the upshift of spectral Raman G band for the inner tube due to strain and $\Delta\omega_o = 6cm^{-1}(strain) + 12cm^{-1}(electron-phononcoupling)$ is for the outer tube at 0 GPa obtained by the extrapolation.

Table 4.2: *DWCNT G-band pressure coefficients and relative intensities for four different pressure transmitting media (oxygen, argon, methanol-ethanol4:1 and H_2SO_4) (633 nm) (i: inner tube and o: outer tube) [19]*

PTM	$d\omega_i/dP$ (cm^{-1}/GPa)	$d\omega_o/dP$ (cm^{-1}/GPa)
O_2	4.1	6.9
Argon	5.1	8.6
4:1 M-E	3.3	5.8
H_2SO_4	2.2	$\approx 2.1(\pm30\%)$

The pressure behavior of DWCNT for different pressure transmitting medium are different. These different behavior of pressure transmitting mediums are due to different local ordering, shell formation and molecular organization on the surfaces of carbon nanotubes [21]. The small value of pressure dependent frequency shift for H_2SO_4 PTM compared to other pressure transmitting mediums is due to development of molecular shells around the surface of carbon nanotubes [21, 57].

4.6 High Pressure by Diamond Anvil Cell (DAC)

High pressure on the sample is achieved by Diamond Anvil Cell (DAC). High pressure experiment were restricted to few laboratories until 1960 due to engineering and safety limitations [58, 59]. The invention of diamond anvil cell (DAC) has made it easy to perform high pressure experiment up to 1 Mbar, safely and reliably [60, 61].

The high pressure can be obtained by increasing force or decreasing the surface area on which the pressure is applied. The DAC allows to get high pressure by applying moderate force on small area. The high pressure is easily achieved by reducing the area. The standard DAC can be used to apply pressure from 10 - 300 kbar. The standard DAC consists of two flawless diamonds of weight 0.067 gram facing parallel and opposite to each other, culet, metallic gasket and screws. The screws are tightened by which the diamonds are pressed

against each other and pressure is increased. The place where the two diamonds contact each other is called culet. So smaller the culet, higher the pressure that can be achieved with less force. The metallic gasket is made out of a hard metal foil and separates the two culets. The gasket is used to *1.* contain the hydrostatic transmitting medium in a cavity between the diamond. *2.* avoid the anvil failure by providing support to diamond tips which decreases the pressure at the edges of the cult.

Two steps are required to prepare the diamond cell
1. The new cell is prepared by placing the diamonds on right place and preserving the alignments. The misaligned cell can cause the diamond breakage and results in the failure of experiment. The alignment is of two types, tilt and axial alignment. The axial alignment makes the two diamonds centered by the side screws. The tilt alignment is used to make the two diamonds parallel by adjusting the bottom screws. *2.* The second stage is preparation of gaskets. Gasket is a crucial part of DAC. Gaskets are made of hard steel. The failure of gasket can lead the termination of experiment along with the possibility of diamond breakage. The gaskets are pre-indented to desired thickness in steps by external force. Then hole of required diameter according to the pressure required is drilled at the center of the indent. The diameter of the hole should be 1/3 to 2/5 of culet diameter for safe and good high pressure experiment. Before loading the sample, the gasket is cleaned by ultra sonication.

When the gasket is ready, sample with some hydrostatic fluid is loaded in the gasket hole. The liquid is called pressure transmitting medium and is used to apply hydrostatic pressure on the sample. The small peace of ruby is also placed inside the hole of the gasket. The pressure in the chamber of diamond cell can be measured by ruby. The ruby emits a light when excited by a light source. The emitted light is collected by the spectrometer. The peak of the ruby light shifts linearly with the increase of pressure (7.567 cm^{-1}/GPa). The broadening of ruby peak (R1) is used as a indication of deviation from hydrostatic condition. During the high pressure experiment hole of gasket is checked after every pressure value reading. The expansion of the hole means diamonds start to reach each other and this is the failure of the gasket and experiment has to be stopped.

4.7 Experiments and Results for Sulphuric Acid Doped DWCNT

We report two series of experiments for sulphuric acid doped DWCNT. First we shall discuss the Raman spectroscopy of H_2SO_4 doped DWCNT and second we shall report on high pressure Raman spectroscopy of H_2SO_4 doped DWCNT.

The different types of DWCNT exposed to high pressure are DWCNT synthesized by CCVD, non lyophilized and lyophilized DWCNT obtained by the transformation of peapods. The synthesis details of DWCNT used in this study are already discussed in chapter 3.

Raman Spectroscopy Experiment

The first set of experiments consist of Raman spectroscopy of pristine and sulphuric acid doped DWCNT synthesized from CCVD with four laser excitation wavelengths 468 nm, 530 nm, 568 nm and 647 nm. The intensity of the Raman RBM and G mode for double wall carbon nanotubes when doped with sulphuric acid is decreased significantly compared to undoped double wall carbon nanotubes. The upshift of the G band is observed when doped with sulphuric acid.

Table 4.3: *The ω_{G_i} is for inner tube and ω_{G_o} is for outer tube Raman G mode shifts. The G mode contributions are taken at 468 nm, 530 nm, 568 nm and 647 nm laser excitation wavelengths for pristine and H_2SO_4 doped DWCNT synthesized from CCVD*

Laser Wavelength λ nm	ω_{G_i} cm^{-1}	$\Delta\omega_{G_i}$ cm^{-1}	ω_{G_o} cm^{-1}	$\Delta\omega_{G_o}$ cm^{-1}
468	1581		1592	
468+H_2SO_4	1587.5	6.5	1606	14
530	1581		1592	
530+H_2SO_4	1585.5	4.5	1602.5	10.5
568	1581		1592	
568+H_2SO_4	1584.9	3.9	1603.7	11.7
647	1582		1593	
647+H_2SO_4	1586.7	4.7	1604.6	11.6

Table 4.3 shows the Raman G mode spectral positions for inner and outer walls of undoped and doped DWCNT synthesized from CCVD at four different laser excitation wavelengths. The upshift recorded for inner tube is from 3.9 cm^{-1} to 6.5 cm^{-1} while for outer tube 10.5 cm^{-1} to 14.0 cm^{-1}. The average upshift observed for inner tube Raman G band is 4.9 cm^{-1} and for outer tube, upshift is 11.9 cm^{-1}. The strain induced G mode frequency upshift of graphite

for the first H_2SO_4 intercalation stage is 4 cm^{-1} [19, 62, 63]. This shift increases to two times or three times for second and third stages. Thus subtracting 4 cm^{-1} from the total shift can give the upshift due to charge doping. Charge induced shifts in DWCNT can be associated to changes in the electron-phonon coupling [19]. Chen et al found that only 10% charge is transferred on the inner tube of DWCNT [20]. So the inner tube shift can be taken as reference for strain induced shifts. The modification of electron phonon coupling due to charge transfer is attributed for remaining upshift [64]. DWCNT can be applied as nanoscale pressure sensor.

High Pressure Raman Spectroscopy Experiment

High pressure Raman spectroscopy studies were performed at the Physics Department, Queen Mary University of London UK under the supervision of Dr. Andrei Sapelkin. Laser excitation energy used was 1.96 eV (632.8 nm).
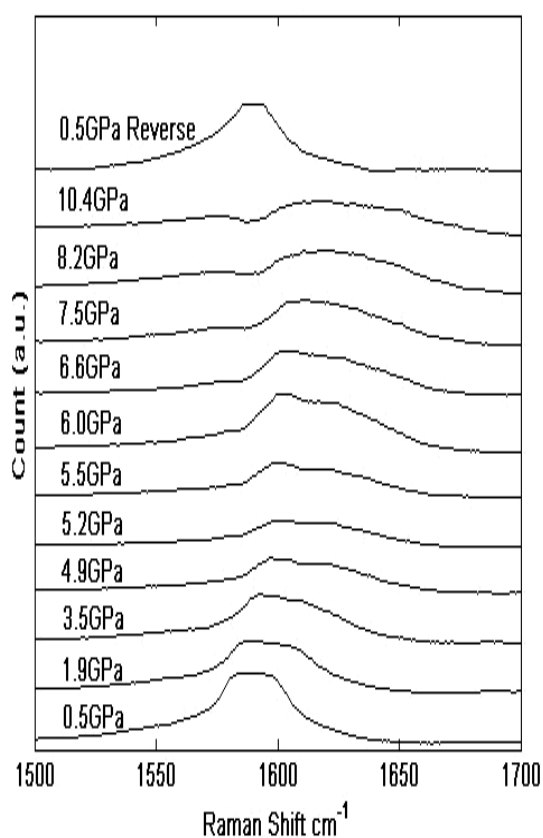
Figure 4.17: *G band Raman spectra of DWCNT (synthesized by CCVD) doped with sulphuric acid at different pressure values using 633 nm laser excitation wavelength.*

The double wall carbon nanotubes used in the experiments are synthesized

from catalytic chemical vapor deposition as reported in reference [65]. In this
study we have applied the high pressure Raman spectroscopy to explore the
contributions of internal and external walls in the sulphuric acid doped double
wall carbon nanotubes to know the interwall interaction between the two walls.
Sulphuric acid used is supposed to serve as pressure transmitting medium as
well as for p-type doping. The p-type doping helps to separate the Raman G
band contributions from inner and outer tubes. This positive charge on the
DWCNT help in separation of tubes and easy penetration of pressure trans-
mitting medium into the interstitial spaces in the bundles of carbon nanotubes.

For the structuring of H_2SO_4 around the tubes (CCVD) we have used the
three different acid concentrations. In first, tubes were mixed with the 100%
acid, in second part tubes were put in the 90% acid + 10% distilled water
solution and in the third part we used 50% acid + 50% distilled water solution
with nanotubes. High pressure on the sample was achieved by Diamond Anvil
Cell. Pressure dependence of the DWCNT Raman tangential modes peaks were
studied in the 0 to 15 GPa pressure range. The normal trend is that intensities
of Raman signal decreases and bands shift up when pressure is increased.

(a)   (b)
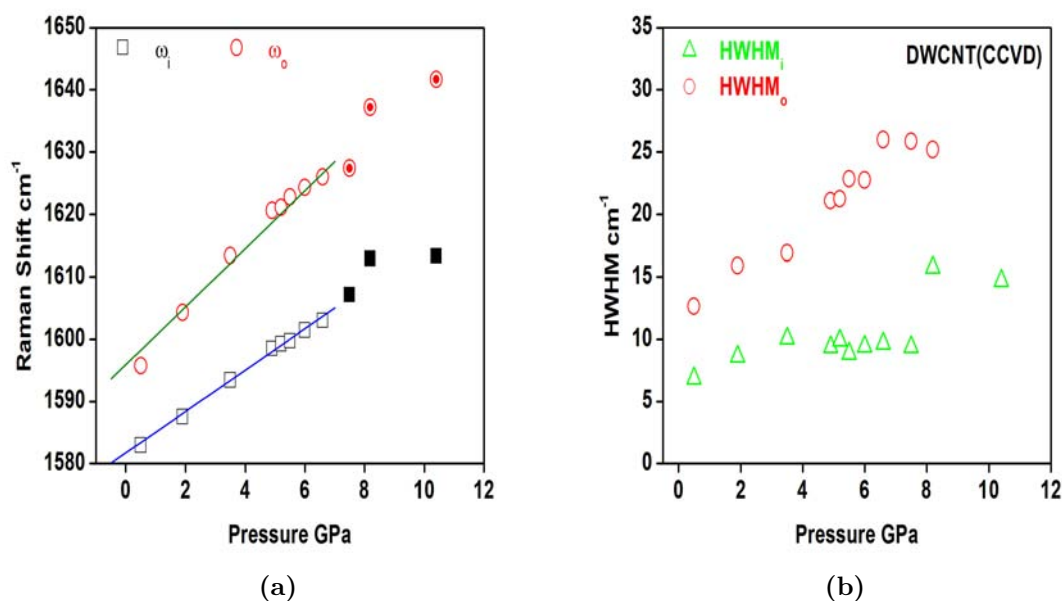
Figure 4.18: *(a)Raman G band frequency shift for inner and outer tube of
DWCNT(CCVD) with the increase of pressure. (b) HWHM of Raman G band for
inner and outer tube of DWCNT(CCVD) with the increase of pressure.*

The figure 4.17 shows the evolution of Raman G band spectra with the
increase in pressure for DWCNT (CCVD) doped with H_2SO_4 (Laser excitation

633 nm). The contribution for the inner and outer tubes are prominent with pressure increase. The outer tube intensity decreases more compared to the inner tube intensity with the increase in pressure.

The figure 4.18(a) shows the upshift of the Raman G band for inner and outer tubes with increase in pressure. There is a clear difference between pressure coefficient for inner and outer tubes. The linear response of the Raman G band upshift changes at at 6.6 GPa. The change in response at the transition pressure is due to a phase transition of tubes. The open circles and open squares are values for the outer and inner tubes respectively upto the transition pressure. The solid circles and solid squares are for data values after transition pressure. The pressure coefficient obtained by the linear fit for the region before phase transition for outer tubes (4.7 cm^{-1}/GPa) is larger than for inner tubes (3.4 cm^{-1}/GPa). In the figure 4.18(b), before the transition pressure, the line width for outer tubes increases at higher rate with pressure increase compared to inner tubes. This shows that the inner tube is less affected by the hydrostatic pressure due to shielding of the outer tube.

(a)   (b)
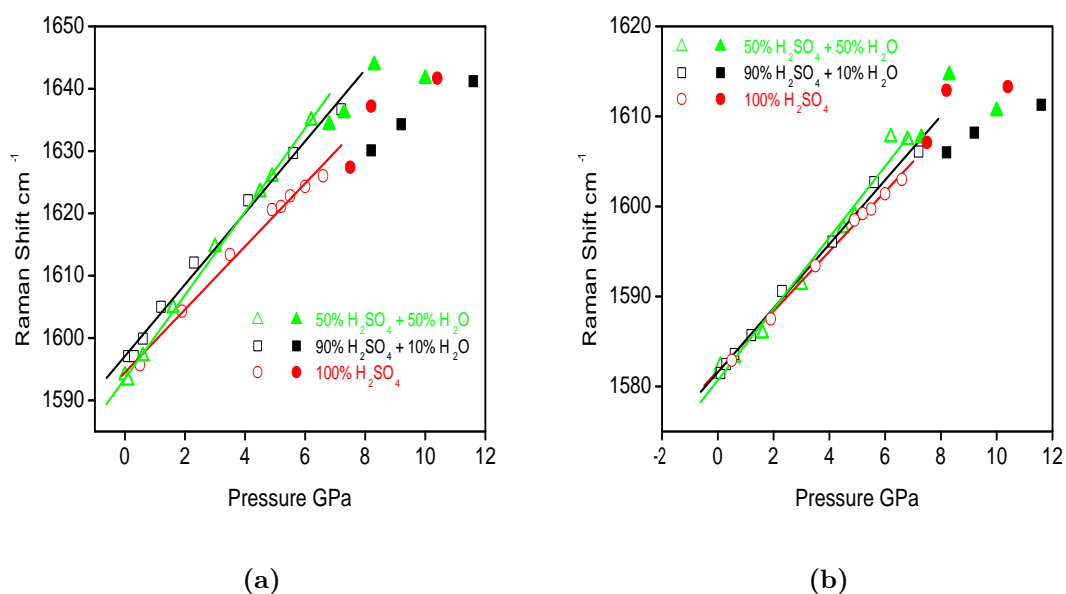
Figure 4.19: *DWCNT(CCVD) with three different concentrations of sulphuric acid and water. 1-100% H_2SO_4 2-90% $H_2SO_4+10\%$ H_2O 3-50% $H_2SO_4+50\%$ H_2O(a)Raman G band frequency shift for outer tube with the increase of pressure (b) Raman G band frequency shift for inner tube with the increase of pressure.*

The figure 4.19 shows the G band Raman spectral shift of DWCNT(CCVD) with three different compositions of sulphuric acid and water that is *1-* 100% H_2SO_4 *2-* 90% $H_2SO_4+10\%$ H_2O *3-* 50% $H_2SO_4+50\%$ H_2O at the different

pressure values. Figure 4.19(a) represents the Raman G band frequency shift for outer tube with the increase of pressure. Figure 4.19(b) gives the Raman G band frequency shift for inner tube with the increase of pressure. The open circles, open squares and open triangles are values upto the transition pressure while solid are for after transition pressure.

Table 4.4: *DWCNT(CCVD) G-band pressure coefficients for inner and outer tubes with three different concentrations of sulphuric acid and water. 1-100% H_2SO_4 2-90% H_2SO_4+10% H_2O 3-50% H_2SO_4+50% H_2O*

DWCNT(CVD)	(H_2SO_4)	(90%H_2SO_4+10%H_2O)	(50%H_2SO_4+50%H_2O)
$d\omega_i/dP$ (cm$^{-1}/GPa$)	3.4	3.6	4
$d\omega_o/dP$ (cm$^{-1}/GPa$)	4.7	5.7	6.7

For outer tube, the pressure coefficient obtained by linear fit upto transition pressure increases from 4.7 cm$^{-1}/GPa$, 5.7 cm$^{-1}/GPa$ to 6.7 cm$^{-1}/GPa$ for 100% H_2SO_4, 90% H_2SO_4+10% H_2O and 50% H_2SO_4+50% H_2O respectively. This shows that for higher concentration of sulphuric acid, the pressure experienced by CNT is smaller when compared with lower concentration of sulphuric acid. This can be attributed to higher ordering of sulphuric acid for stronger acid. The structuring of the medium around carbon nanotubes makes nanoscale shells around the tube and shields the tube from environmental effects. The inner tube shows the same trend as the outer tube but the increase in pressure coefficient is very small compared to outer tube. This shows that the inner tube is less affected by ordering of the pressure transmitting medium around the DWCNT. The pressure coefficient already reported [19] are 2.2 cm$^{-1}/GPa$ for inner tube and 2.3 cm$^{-1}/GPa$ for outer tube with 100% sulphuric acid. These lower values compared to our values are due to smaller concentration of tubes which gives higher ordering of acid around tubes leading to less pressure experienced by tubes. The pressure coefficients for outer and inner tubes with three acid-water compositions are tabulated in table 4.4.

4.8 Conclusion

Controlled nitrogen doping of carbon nanotubes is still difficult. Raman spectroscopy can help to systematically characterize the physical and electronic structure of nitrogen doped carbon nanotubes and carbon nanofibers. Raman

spectroscopy of nitrogen doped multiwall carbon nanotubes for Raman D and G mode is different when compared with pristine carbon nanotubes. This suggest that the electron phonon coupling is influenced by nitrogen doping. The small change in the half width half maximum of D mode for pyridine based carbon nanofibers in comparison to pristine CNF show that nitrogen doping in pyridine based carbon nanofibers is negligible. In contrast to pyridine based CNF, the acetonitrile based carbon nanofibers shows the considerable increase in the HWHM of D mode indicating the presence of defects due to higher doping of nitrogen and is consistent with XPS and EA values.

The high values of the pressure coefficients for inner and outer tubes shows that sulphuric acid is not sufficiently doped due to a higher concentration of DWCNT limiting our interpretation to trends. For higher concentration of sulphuric acid, the pressure experienced by the outer tube of DWCNT (CCVD) is lower when compared with low concentration of sulphuric acid. This can be attributed to higher nano scale ordering in strong sulphuric acid around the carbon nanotubes.

Bibliography

[1] M. S. Dresselhaus, G. Dresselhaus, and P. C. Eklund, *Science of Fullerences and Carbon nanotubes* (Academic Press, New York, 1996).

[2] J. Sloan *et al.*, Journal of The American Chemical Society **124 (10)**, 2116 (2002).

[3] V. A. Basiuk and E. V. Basiuk, *Chemistry of carbon nanotubes* (American Scientific Publishers, Los Angeles USA, 2007).

[4] A. Jorio, G. Dresselhaus, and M. S. Dresselhaus(Eds), *Topics Applied Physics III* (Springer- Verlag, Berlin Heidelerg, 2008), pp. 531 – 566.

[5] J. E. Fischer, Accounts of Chemical Research **35**, 1079 (2002).

[6] L. Kavan *et al.*, The Journal of Physical Chemistry B **105**, 10764 (2001).

[7] J. Mandumpal, S. Gemming, and G. Seifert, Chemical Physics Letters **447**, 115 (2007).

[8] P. Serp, M. Corrias, and P. Kalck, Applied Catalysis A: General **253**, 337 (2003).

[9] M. L. Toebes *et al.*, The Journal of Physical Chemistry B **108(31)**, 11611 (2004).

[10] T. G. Ros *et al.*, Journal of Catalysis **211**, 85 (2002).

[11] G. S. Duesberg *et al.*, Diamond and Related Materials **13**, 354 (2004).

[12] M. Dresselhaus, G. Dresselhaus, and P. Avouris, *Carbon nanotubes:synthesis, structure, properties, and applications.* (Springer-Verlag, Germany, 2001).

[13] J. Tsang *et al.*, Nature Nanotech **2**, 725 (2007).

[14] M. S. Dresselhaus and G. Dresselhaus, Advances in Physics **30**, 139 (1981).

[15] R. J. Hemley, Erskine Williamson, Extreme Conditions, and the Birth of Mineral Physics, (2006).

[16] M. Grennvall, Master's thesis, Lulea University of Technology, (2008).

[17] U. D. Venkateswaran *et al.*, physica status solidi (b) **223**, 225 (2001).

[18] I. Loa, Journal of Raman Spectroscopy **34**, 611 (2003).

[19] P. Puech *et al.*, Physical Review B **78**, 045413 (2008).

[20] G. Chen *et al.*, Physical Review Letters **90**, 257403 (2003).

[21] P. Puech *et al.*, Physical Review B **73**, 233408 (2006).

[22] D. Y. Zhang *et al.*, Applied Physics Letters **79**, 553 (2001).

[23] M. R. Pederson and J. Q. Broughton, Physical Review Letters **69**, 533 (1992).

[24] S. Iijima, Nature **354**, 56 (1991).

[25] S. Iijima and T. Ichihashi, Nature **363**, 603 (1993).

[26] J. Y. Yi and J. Bernholc, Physical Review B **47**, 1708 (1993).

[27] P. Ayala *et al.*, Carbon **48**, 576 (2010).

[28] S. van Dommele, Nitrogen Doped Carbon Nanotubes: synthesis, characterization and catalysis, (2008).

[29] J. Zanchetta and A. Marchand, Carbon **3**, 332 (1965).

[30] J. Zanchetta and A. Marchand, Carbon **3**, 483 (1966).

[31] D. Franceschini, C. Achete, and F. F. Jr., Applied Physics Letters **60**, 3229 (1992).

[32] H. Kang and S. Jeong, Physical Review B **70**, 233411 (2004).

[33] A. Nevidomskyy, G. Csányi, and M. Payne, Physical Review Letters **91**, 105502 (2003).

[34] V. Krstic *et al.*, Europhysics Letters **77**, 107 (2007).

[35] R. Czerw *et al.*, Nanoletters **1(9)**, 457 (2001).

[36] M. Castignolles, Ph.D. thesis, Université Montpelliere II, France, (2004).

[37] H. C. Choi *et al.*, Applied Physics Letters **85**, 5742 (2004).

[38] H. C. Choi, J. Park, and B. Kim, Journal of Physical Chemistry B **109**, 4333 (2005).

[39] P. Ayala *et al.*, Journal of Physical Chemistry C **101**, 2879 (2007).

[40] Y. T. Lee *et al.*, Journal of Physical Chemistry B **107**, 12958 (2003).

[41] J. Liu, S. Webster, and D. L. Carroll, Journal of Physical Chemistry B **109(33)**, 15769 (2005).

[42] C. Tang, Y. Bando, D. Goldberg, and F. Xu, Carbon **42**, 2625 (2004).

[43] M. Glerup *et al.*, Chemical communications **20**, 2542 (2003).

[44] C. L. Sun *et al.*, Journal of American Chemical Society **128 (26)**, 8368 (2006).

[45] R. Sen *et al.*, Journal of Material Chemistry **7**, 2335 (1997).

[46] J. Teddy, Ph.D. thesis, Institut National Polytechnique De Toulouse, Toulouse, (2009).

[47] F. V. Páeza *et al.*, Chemical Physics Letter **424**, 345 (2006).

[48] S. Kawasaki *et al.*, physica status solidi (b) **241**, 3512 (2004).

[49] S. Kawasaki *et al.*, Journal of Physics and Chemistry of Solids **65**, 327 (2004).

[50] M. J. Longhurst and N. Quirke, Physical Review Letters **98**, 145503 (2007).

[51] K. Gao *et al.*, Solid State Communications **147**, 65 (2008).

[52] T. Chang, Applied Physics Letters **93**, 061901 (2008).

[53] U. D. Venkateswaran *et al.*, Physical Review B **59**, 10928 (1999).

[54] J. Arvanitidis *et al.*, Physical Review B **71**, 125404 (2005).

[55] X. Yang and G. Wu, Europhysics Letters **81**, 47003 (2008).

[56] P. Puech *et al.*, Physical Review Letters **93**, 095506 (2004).

[57] W. Zhou *et al.*, Physical Review B **71**, 205423 (2005).

[58] H. T. Hall, Review of Scientific Instruments **29**, 267 (1957).

[59] A. J. Ghandour, Ph.D. thesis, Department of physics Queen Mary, University of London, (2009).

[60] J. C. Jamieson, A. W. Lawson, and N. D. Nachtrieb, Review of Scientific Instruments **30**, 1016 (1959).

[61] C. E. Weir, E. R. Lippincott, A. V. Valkenburg, and E. N. Bunting, Journal of Research of the national Bureau of Standards **63A**, 55 (1959).

[62] R. Nishitani, Y. Sasaki, and Y. Nishina, Physical Review B **37**, 3141 (1988).

[63] M. Hanfland, H. Beister, and K. Syassen, Physical Review B **39**, 12598 (1989).

[64] S. Piscanec *et al.*, Physical Review B **75**, 035427 (2007).

[65] E. Flahaut, R. Bacsa, A. Peigney, and C. Laurent, Chemical Communication 1442 (2003).

Chapter 5

Raman Spectroscopy Of Individual Double Wall Carbon Nanotubes

This chapter describes the comparative study of individual and bundled double wall carbon nanotubes by Raman spectroscopy. We shall discuss the radial breathing modes, G band and 2D band in the Raman spectra of individual tube and nanotubes in bundles. The contributions coming from inner and outer tubes in DWCNT for different bands in two situations i.e., with and without bundles are explained. The individual tube is an ideal to find the interlayer coupling and also the environmental effects. We shall also compare the Raman spectra of DWCNT synthesized by CCVD and transformed by peapods. To have comprehensive comparison we have taken the Raman spectra at three different excitation wavelengths (468, 530 and 568 nm) for individual carbon nanotube as well as the DWCNT in bundles. The laser power influence on the contribution of inner and outer walls of individual double wall will be elaborated by exciting the individual double wall tube from 1 mW laser power to 3 mW.

5.1   Introduction

The Raman bands of single wall, double wall and multiwall carbon nanotubes are not identical and there exists clear differences between Raman bands for different types of tubes.

For DWCNT in bundles, the interaction between the tubes can modify the RBM frequencies [1, 2]. This inner-outer tubes interaction apply radial pressure on inner tube and down shifts the transition energies [1]. A recent Raman study [3] of individual DWCNT shows spectra for different metallic

127

and semiconducting tube configurations for inner and outer tubes. Using SC for semiconducting and M for metallic tubes, we can use the following notation for the four combinations of tubes for DWCNT: M@M, SC@M, M@SC, SC@SC (inner@outer). The frequency of the RBM and excitation energy provide the opportunity to determine the tube structure (n,m). The G band shape is dominant by the metallic or semiconducting tube depending on which one is in strong resonance with the excitation energy when one of the two tubes in individual DWCNT is semiconducting and other is metallic. For M@SC combination the inter layer interaction is weak as compared to SC@M.

For SWCNT, the disorder induced D band and the second order 2D bands have only single band. For DWCNT or MWCNT, the D and 2D bands consists of more than one peaks or bands with shoulders. So by just observing the Raman bands of carbon nanotubes, one can observe whether the tubes are SWCNT, DWCNT or MWCNT.

For SWCNT, the G^+ band have a half width at half maximum of 3 cm^{-1} which is lower than the HWHM value of graphite (7 cm^{-1}) [4]. The G band in DWCNT is composed of two bands that is one for inner and one for outer tube as discussed in chapter 2. An additional less intense electronic interlayer contribution which could be fitted by a single Lorentzian band has been observed at lower frequency (1560 cm^{-1}). The wall interaction has to be taken into account as evidenced by findings in doped DWCNT and by the influence of high pressure on DWCNT. The coupling of the wall is essential for DWCNT Raman bands. For bundled DWCNT, all the G band contributions(inner tube, outer tube and interlayer interaction) together form a broad band.

5.2   Samples And Experiments

DWCNT were prepared by the CCVD method as described in reference [5]. A dense mat of composite powder is produced. The catalyst used is $Mg_{0.9}Co_{0.1}O$ solid solution with excess of Mo oxide. This MgO-based catalyst was easily removed by mild acidic treatment yielding to gram-scale amounts of clean carbon nanotubes. The sample contains 77% double-walled carbon nanotubes. High-resolution electron microscopy shows that the inner tubes of the DWCNT have a diameter ranging from 0.6 to 2.3 nm.

The DWCNT have been dispersed using a 1,2-dichloroethane (DCE) solution. The solution DWCNT and 1,2-dichloroethane has been sonicated for a short time (less than 10 min) at low power (less than 35 W). This debundles the DWCNT to some degree. Then it was deposited on an oxidized silicon substrate pre-patterned with secondary Au electrodes. Only the top portion of the

solution containing isolated DWCNT has been used for deposition on substrate. The samples have been rinsed with acetone and ethanol after deposition to remove the DCE. The samples were analyzed by transport experiments prior and after the sonication. From comparative transport measurements we conclude that tubes have not been damaged by the sonication process.
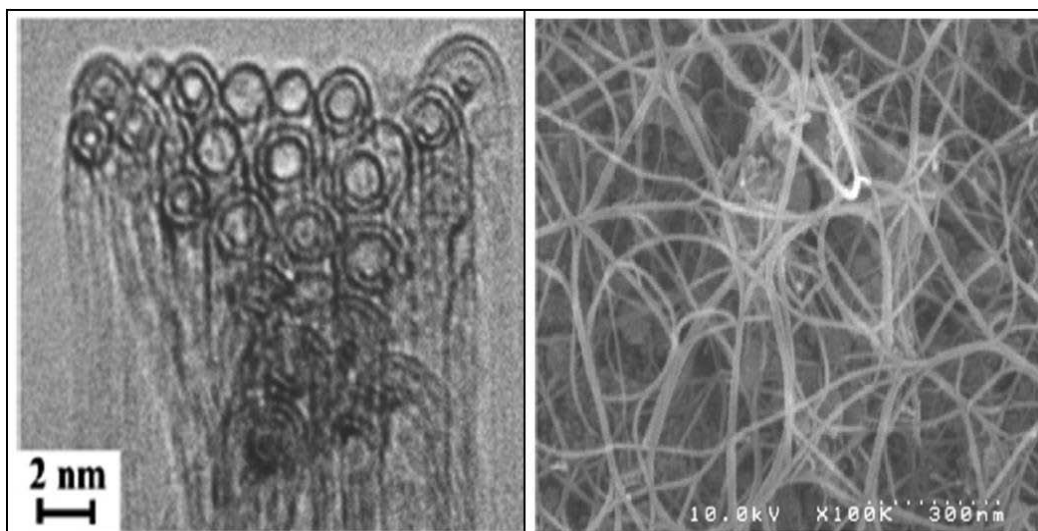
Figure 5.1: *HRTEM images of DWCNT(left side) and FEG-SEM image of raw DWCNT (right side) [5]*

Individual tubes (typical length: 3mm) are localized by scanning force microscopy. The tubes have been at a later stage connected with Pd electrodes using e-beam lithography and lift-off technique with a distance of 0.5 mm between the electrodes. We can differentiate tubes which are bundled and individual tubes using scanning force microscopy. We can estimate the individual DWCNT height(1.4±0.4 nm) from the analysis of scanning force microscopy images. Height variation of the substrate results in a relative large uncertainty in the tube height. The transport measurements obtained by the the gate-voltage variation performed under ambient conditions show that the individual double wall tube is conducting.

Raman spectra were acquired on a T64000 spectrometer from Horiba Jobin-Yvon industry. The laser power was measured after the objective. Polarization has been selected along the tube axis according to the scanning force microscopy images of the tube to have the maximum light absorption. We used three different excitation wavelengths (468 nm, 530 nm and 568 nm) for individual tube and nanotubes in bundles.

Carbon nanotubes have very high thermal conductivity and we find that

laser heating is less important for individual DWCNT in contact with the substrate or connected to the metal electrode. We use 1mW with an objective of magnitude 100. Bundles of DWCNT are more sensitive to laser power. To minimize heating effects on DWCNT bundles we use a low laser power, typically 0.1 mW and an objective of magnitude 40 to increase the focal spot size (2mm) decreasing the power density. All spectra have been recorded by integrating the signal from the scattered light for 100-500 s. For the laser power dependent measurements, we increased the laser power up to 3 mW.

5.3 Results And Discussion

5.3.1 Individual and Bundled DWCNT
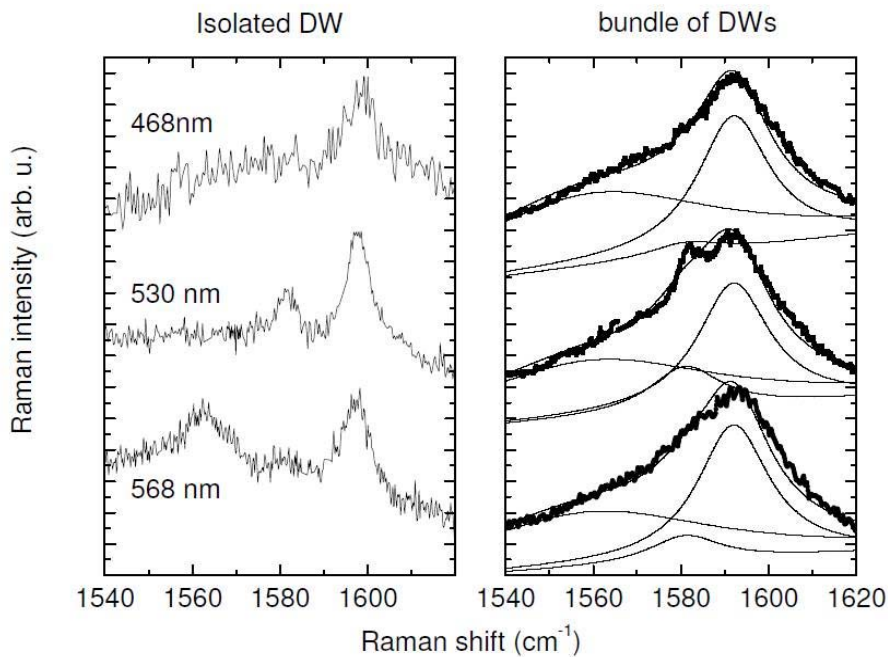
Figure 5.2: *G band of individual DWCNT(left side) and bundles of DWCNT (right side) using three different excitation energies.*

Figure 5.2 shows the Raman G band region of the individual DWCNT and bundled DWCNT excited at three different excitation wavelengths (468 nm, 530 nm and 568 nm). The Raman spectra from the individual DWCNT contains up to three spectral bands. The three contributions are coming from inner tube, outer tube and interlayer coupling. We find all bands in individual tubes are narrower while the spectra of DWCNT in Bundle show a larger and asymmetric

G band. The spectra of the DWCNT in bundles is analyzed by fitting with three Lorentzian line shapes of fixed spectral positions and taking the relative intensities as a free parameter [6]. The Raman band positions and HWHM for individual DWCNT and tubes in bundles are reported in Table 5.1. The HWHM is much smaller for individual DWCNT.

Table 5.1: *G band and band due to interlayer coupling for bundled and individual DWCNT.*

Raman Mode	Composition	Peak position (cm^{-1})	HWHM (cm^{-1})
Interlayer coupling	In bundle	1560	35
Interlayer coupling	Individual	1563	8
G band inner tube	In bundle	1581	10
G band inner tube	Individual	1580	4
G band outer tube	In bundle	1592	10
G band outer tube	Individual	1597	4

The HWHM of the G band of the inner and the outer tube of individual tube is 4 ± 1 cm^{-1} which is the same HWHM observed for individual SWCNT and for single layer graphene [7]. The HWHM depends on the decay process [8] and is increased by the number of defects. It has been shown that for SWCNT that the HWHM varies with applied voltage, with a minimum value at 4 cm^{-1} [4, 9].

The changes in the Raman spectra by gate voltage can be used to probe local doping in carbon nanotubes or to observe the changes in carrier densities induced by environmental interactions. These spectral changes are attributed to the renormalization of the carbon nanotube phonon energies by the electron-phonon interaction when the carrier density in the carbon nanotube is changed [9]. For DWCNT in bundles, the HWHM of inner and outer tube G band is 10 cm^{-1}. This larger HWHM for bundles can be explained by the interaction with neighboring tubes leading to heterogeneous line broadening. For comparison, pyrolytic graphite has a similar HWHM (7 cm^{-1}) [10]. Few reports investigate the number of tubes in the bundle. Jiang *et al.* [11] show that the Breit-Wigner-Fano line which is weak for an individual tube in air and without electrode contact, intensity is strongly enhanced in a bundle and they observe no change of HWHM. The Breit-Wigner-Fano line intensity increases strongly with the thickness of bundles. Nguyen *et al.* [12] shows that

in air, oxygen doping of individual metallic tube move the Fermi level towards van Hove singularity leading to the disappearance of the Breit-Wigner-Fano line into Lorentzian line. The Breit-Wigner-Fano line shape can be restored by controlling the gate voltage. In bundles the atoms in contact with air, are reduced and this prevents doping and consequently the Fermi level is positioned close to the K point. Higher the number of tubes in DWCNT bundles increases the heterogeneity. The increase of the broadening for DWCNT can be connected to the number of DWCNT in each bundle and the fact that several bundles are observed at the same time . A variation in doping (Fermi level position) of each bundles due to oxygen leads to a change in frequency and resulting in a broader band when observing several bundles at the same time. For both metallic [12] and semiconducting [13] tubes, this broadening is observed. We consequently conclude that heterogeneity and not defects is at the origin of the increase of the measured HWHM.

For the Raman spectra from an individual DWCNT as shown in Figure 5.2, the spectral position of the G band of the inner tube is at 1580 ± 2 cm^{-1} and for the outer tube at 1597 ± 2 cm^{-1}. The spectral position of the inner tube is consistent with the extrapolated spectral position deduced from high pressure experiments [14] and when studying the influence by chemical doping of DWCNT [15]. The spectral position of the G band for the outer tube is relatively high compared to values found by high pressure experiments [14] and chemical doping of DWCNT [15]. When changing the excitation energy, we can see the considerable changes in the intensity of the inner tube which we can attribute to changes in the resonance condition. At 568 nm excitation wavelength an additional band is appeared at 1563 cm^{-1} which has been previously observed and identified as being associated with electronic coupling with the environment and the outer tube [6]. Nguyen *et al.* have shown that SWCNT exposed to air leads to strong p-doping of the SWCNT [12]. The G band changes are similar to changes observed when the Fermi level shifts to few hundred meV to lower value with the application of gate voltage. The high frequency associated to the outer tube in our case is consistent with this explanation.

5.3.2   Resonant Excitation

Kataura plot relates the band gap energy in a carbon nanotube with its diameter. The RBM spectral position in Raman spectra is inversely proportional to the diameter and with Kataura plot one can find the chiral indices. To identify the tube structure we use the electronic transition energies from the Kataura plot [16] with the following expression as reported by Araujo *et al.* [17]:

$$E_{ii}(p, d_t) = \frac{\beta_p \cos(3\theta)}{d_t^2} + a\frac{p}{d_t}\left[1 + blog\left(\frac{c}{p/d_t}\right)\right] + \frac{\gamma_p}{d_t} \tag{5.1}$$

Using this analytical expression and $\gamma_p = 0$, one can estimate accurately the transition energies for E_{11}^{sc}, E_{22}^{sc} and E_{11}^{M}. For the E_{33}^{sc} and E_{44}^{sc} or E_{55}^{sc} and E_{66}^{sc}, we use $\gamma = 0.305$ for unbound excitonic states as suggested by the authors. For the E_{22}^{M} transition, we use $\gamma = 0.305$ which fits well with the experimental results (obtained by electron diffraction and rayleigh scattering) of Sfeir et $al.$ [18] reducing the uncertainty to less than 0.1 eV for the corresponding transition energies.
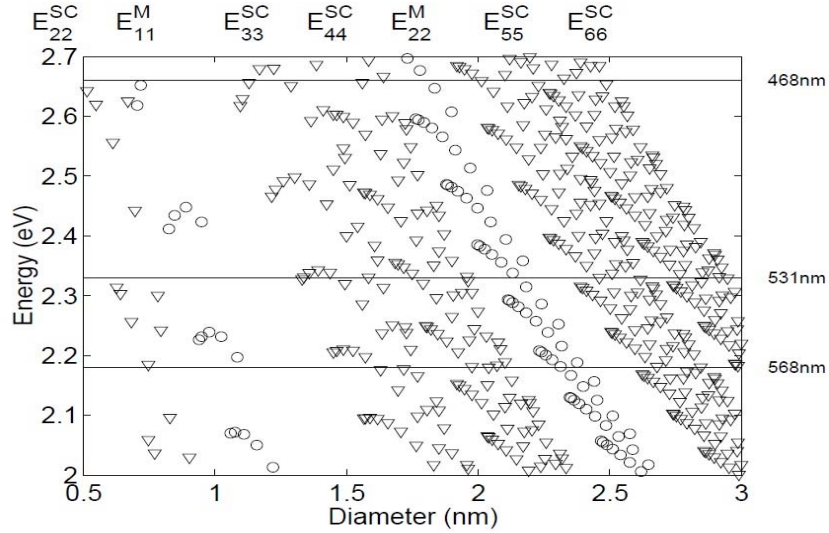
Figure 5.3: *Optical transition energies from Araujo* et al. *[17]. The circles show the transition energies for metallic and the triangles show the transition energies for semiconducting tubes.*

By considering only the resonant Raman scattering experiment and using the figure 5.3, we can identify the several configurations with increasing diameter from the possible diameters. The SC@SC combination corresponding roughly to an inner diameter of 0.6 nm, M@SC corresponding roughly to an inner diameter of 1 nm and SC@M corresponding roughly to an inner diameter of 1.7 nm. We apply the scanning force microscopy to approximate the diameter values with metallic(semiconductor)@semiconductor(metallic) configuration. From the height estimation with scanning force microscopy, we conclude that the M@SC configuration with an inner diameter of 1 nm and an outer one of 1.7 nm is the most likely configuration for the DWCNT investigated in our case.

This configuration is quite consistent with our preliminary electronic transport measurements which show a small on/off ratio in the source-drain current versus the gate voltage dependence characteristic for metallic tubes [19]. From the gate voltage observed at the largest variation of the source drain current we find that the semiconducting tube is p doped.

We note that for a similar DWCNT, M@SC configuration and similar diameter(0.87 nm@ 1.51 nm), Villalpando-Paez *et al.* [3] found a G band frequency of 1591 cm^{-1} without separating contributions from the inner and the outer tube although the tube diameters are similar and the DWCNT have been grown using the CCVD method. Interestingly, in our measurements no splitting is observed here for the 2D band while Villalpando-Paez *et al.* [3] have observed a clear splitting of the 2D for the DWCNT grown from the peapod method. This shows that the two types of behavior of DWCNT, either strongly coupled or decoupled can be observed for CCVD grown tubes. This difference of coupling can be explained by the different growth parameters used in the CCVD method which apparently play an important role in the inter wall spacing. In our case, the inner and outer tubes are strongly coupled, leading to a clear difference in the spectral positions.

Figure 5.4 shows the RBM region and the second order D band (2D band) of the individual DWCNT on top and bundled DWCNT on bottom using 531 nm laser excitation wavelength. The intense RBM bands in the case of individual tube is absent which indicates that the excitation energy does not exactly coincide with the resonance maximum in resonance window with neither of the two tubes(inner and outer). Nevertheless, for the individual DWCNT we have observed the RBM band at 250 cm^{-1} consistent with an inner tube of 0.94 nm diameter. In the range 200-300 cm^{-1}, this is the only feature. In the range 100-200 cm^{-1}, several bands of low intensity are observed.

A less intense spectral band at 150 cm^{-1} consistent with the RBM of 1.61 nm diameter tube can be associated to the outer tube of DWCNT. We have used the constants determined by Telg *et al.* [20] for the determination of the diameter from the RBM frequency. From the Kataura plot reported in Figure 5.3, we found chirality of (12,0) for the inner tube and a chirality of (20,1) for the outer tube. The wall spacing is found 0.34 nm consistent with the interlayer spacing in graphite. For the chirality attribution so far, we have assumed that the coupling between the walls is weak and does not affect the RBM frequencies. The (12,0)@(20,1) is thus the most appropriate combination for inner and outer tubes. We note that Kuzmany *et al.* [1] have reported that the inner tube frequency is dependent to the wall spacing leading to a small correction for inner tube value. For DWCNT in bundles we observe several RBM's in the 140-180 cm^{-1} and 240-270 cm^{-1} spectral range. We find that the 2D band for

isolated tubes is less broad then for bundled DWCNT.
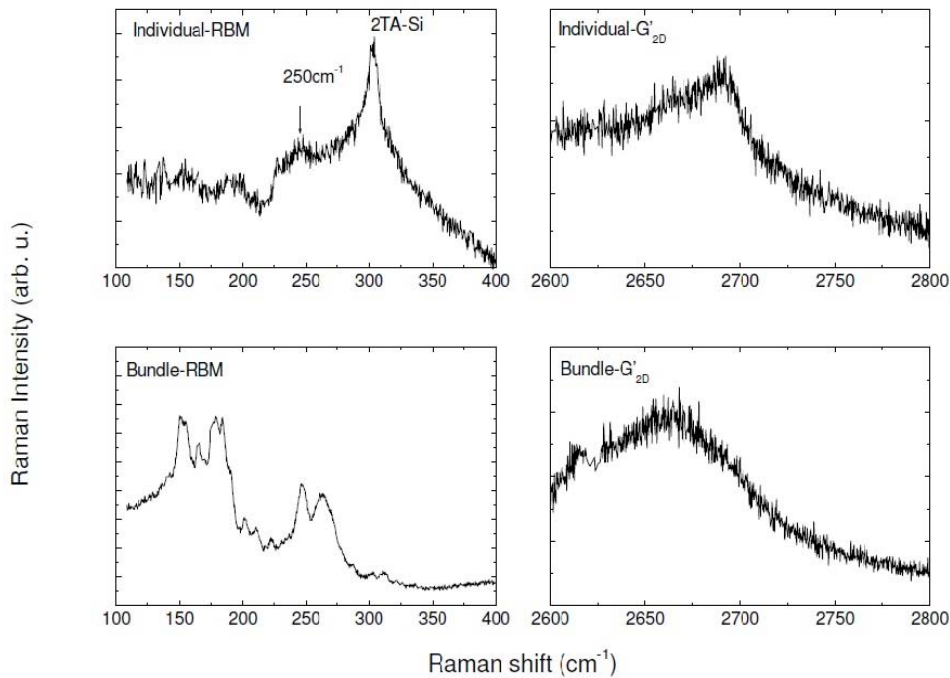
Figure 5.4: *Frequency range of RBM and 2D band of individual DW on SiO_2 (top) and DW bundles (below) at 531 nm.*

Thus conductance measurements, Raman spectra observations in the RBM range and scanning force microscopy measurements are consistent with an M@SC configuration. An outer diameter of 1.61 nm and an inner diameter of 0.94 nm can be deduced when assigning the tubes chiralities to the (12,0)@(20,1) configuration.

5.3.3 Laser Power Effect

Three bands at 1563 cm^{-1}, 1581 cm^{-1} and 1597 which correspond to interlayer interaction, G band for inner tube and outer tube respectively are observed at 1 mW laser power for the individual DWCNT on SiO_2 using 568 nm laser excitation wavelength. We vary the laser power from 1 to 3 mW to observe the laser power effects on the individual DWCNT. We observe changes in the G band of the outer tube and the disappearance of the additional spectral band at 1563 cm^{-1} when increasing laser power from 1 mW to 3 mW. The fitted band positions are reported in table 5.2 for 1 mW and 3 mW. It has been previously found that this additional band at 1563 cm^{-1} is correlated to the G band shift of the outer tube with chemical doping [6]. The G band of the outer tube

shifts to higher frequency and broadens with laser power while the G band of the inner tube remains at the same spectral position. A temperature increase, however, is known to shift the G band to lower frequency and the uniform band broadening. The up-shift and non-uniform broadening can be attributed to

Table 5.2: *G band position for individual DWCNT for two laser powers excited at 568 nm.*

Raman Mode	Laser Power	Peak position (cm^{-1})	HWHM (cm^{-1})
Interlayer coupling	1 mW	1563	8
Interlayer coupling	3 mW	1568	1
G band inner tube	1 mW	1581	4
G band inner tube	3 mW	1580	4
G band outer tube	1 mW	1597	4
G band outer tube	3 mW	1600	6

doping. Different environmental interactions can dope the tubes. Here doping can be due to substrate or oxygen exposure or it can be due to substrate and oxygen both. Doping can lead to an upshift of the G band and can increase the HWHM for semiconducting tubes [13]. This is consistent with our assignment to outer tube as semiconducting tube in an individual double wall tube.

Electrical conductance measurements have shown that one G band of the DWCNT can up shift or down shift and shows hysteresis when scanning the applied gate voltage from -20 volts to +20 volts [21]. For the tube placed on an insulating SiO_2 layer, the Fermi level of the outer tube can be influenced when illuminated through its interaction with its environment (oxygen and substrate). The more or less disappearance of the additional band observed at 1563 cm^{-1} with 3 mW laser power is attributed to electronic coupling [6] and is consistent with a change in the Fermi level position. A less intense band remains at 1568 cm^{-1} with the strongly reduced background. We note that far from the K point, electronic interlayer coupling is removed [12]. In the present case, the G band frequency of the inner tube is not influenced when the laser power increases from 1 mW to 3 mW. The G band position of inner tube at 1580 cm^{-1} shows that the interaction with the outer tube is still present. The absence of a power induced frequency shift is consistent with no considerable charge transfer to the inner tube as reported by Chen *et al.* [15].
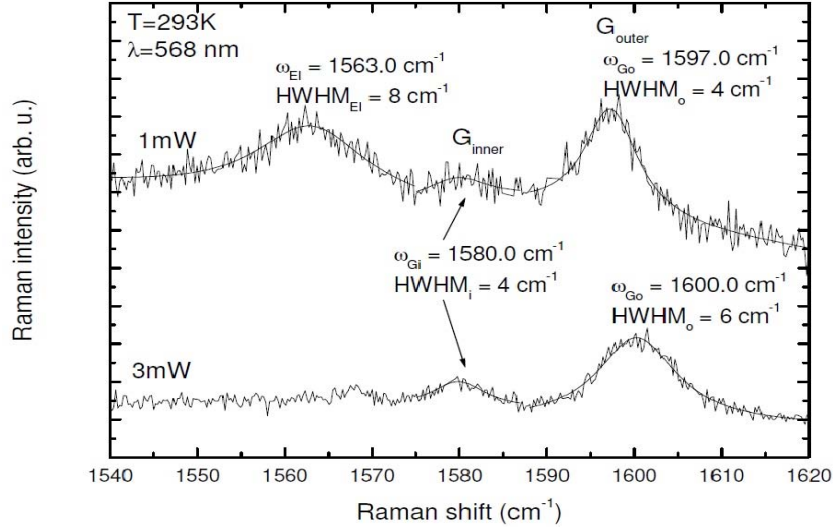
Figure 5.5: *Raman G band of individual double wall carbon nanotube excited at two different laser powers.*

Consistent with what has been reported by Nguyen *et al.* [12], the integrated intensity of all bands of the G band is conserved when normalized to the D band intensity. In our case, the inner tube can be used as a reference because there is no change in frequency and line width with increasing laser power. The integrated intensity of the G band associated to the outer tube compared to the intensity of the G band associated to the inner tube is increased by 40% when the laser power increases from 1 to 3 mW. At the same time, the huge background is reduced along with the band associated with electronic interlayer coupling. This shows that there is an intensity transfer from the electronic interlayer signal to the G band of the outer tube.

5.4   Conclusion

In summary, we find that coupled individual DWCNT show narrow and separated G bands corresponding to the inner and outer tube compared to DWCNT in bundles. The line-widths of the G band of the inner and outer tube are comparable to what has been reported for individual SWCNT and single layer graphene. Bundling broadens the G band considerably. Using height estimation from scanning force microscopy, laser excitation wavelength and preliminary transport measurements, we can identify the tube configuration to be M@SC having diameter 1@1.7 nm with chiralities(12,0)@(20,1). An increase of the laser power at 568 nm leads to a preferential modification of the outer tube and is correlated with the disappearance of a band associated to electronic interlayer coupling.

Bibliography

[1] R. Pfeiffer, F. Simon, H. Kuzmany, and V. N. Popov, Physical Review B **72**, 161404 (2005).

[2] R. R. Bacsa *et al.*, Physical Review B **65**, 161404 (2002).

[3] F. Villalpando-Paez *et al.*, Nano Letters **8**, 3879 (2008).

[4] A. Jorio *et al.*, Physical Review B **66**, 115411 (2002).

[5] E. Flahaut, R. Bacsa, A. Peigney, and C. Laurent, Chemical Communications **12**, 1442 (2003).

[6] P. Puech *et al.*, Physical Review B **78**, 045413 (2008).

[7] A. Das *et al.*, Nature Nanotechnology **3**, 210 (2008).

[8] G. P. Srivastava, *The Physics of Phonons* (Adam Hilger 1990)

[9] J. C. Tsang *et al.*, Nature Nanotechnology **2**, 725 (2007).

[10] M. Hanfland, H. Beister, and K. Syassen, Physical Review B **39**, 12598 (1989).

[11] C. Jiang *et al.*, Physical Review B **66**, 161404(R) (2002).

[12] K. T. Nguyen, A. Gaur, and M. Shim, Physical Review Letters **98**, 145504 (2007).

[13] A. Das and A. K. Sood, Physical Review B **79**, 235429 (2009).

[14] P. Puech *et al.*, Physical Review Letters **93**, 095506 (2004).

[15] G. Chen *et al.*, Physical Review Letters **90**, 257403 (2003).

[16] H. Kataura *et al.*, Synthetic Metals **103**, 2555 (1999).

[17] P. T. Araujo *et al.*, Physical Review Letters **98**, 067401 (2007).

[18] M. Y. Sfeir *et al.*, Science **312**, 554 (2006).

[19] S. Wang *et al.*, The Journal of Physical Chemistry B **109**, 17361 (2005).

[20] H. Telg *et al.*, Physical Review Letters **93**, 177401 (2004).

[21] S. Yuan *et al.*, Nano Letters **9**, 383 (2009).

Chapter 6

General Conclusion

The objectives of this thesis are to investigate the doping and photoexcitation of carbon nanotubes by Raman spectroscopy as well as to characterize the individual double wall carbon nanotubes and compare the results with double wall carbon nanotubes in bundles. Concerning the scope of this work, we have reported several results for doping and photoexcitation effects on carbon nanotubes using Raman scattering process. Raman spectrometry has been widely used as Raman signal observed can be unique to a carbon nanotube. Moreover, the Radial Breathing Mode is diameter dependent and its intensity is directly correlated to optical transition energy. We can analyze the carbon nanotubes in air without preparation and observe some characteristics sometimes even its chirality. Due to double resonance process, the D mode is observable when some defects (all types) are present. Its excitation wavelength dependence goes from 50 cm^{-1}/eV for good carbon to nearly 0 for highly defective carbon. In the first case, it corresponds to the selection of a particular phonon in the Brillouin zone. In the second case of disordered carbon material, it corresponds the breathing of a hexagonal ring. For the G band of SWCNT, its interpretation is not straightforward and ab initio calculation can help in this regard. Two bands are observed, one diameter dependent G$^-$ mode at low frequency and other located close to 1592 cm^{-1} labeled as G$^+$ mode. The G modes are sensitive to doping, leading to modification of the intensities and position. Doping changes the Fermi level position, which hardens the frequency (for n or p doping), and also changes the lattice parameter which harden (p-doping) or soften (n-doping) the frequency. For double wall carbon nanotubes and multi-wall carbon nanotubes, the inner tubes give a frequency corresponding to the graphite value. The outer tube gives a signal close to the single wall carbon nanotube. Moreover, a contribution D', due to stacking defect along the C axis near 1620 cm^{-1} is present.

In the first part, we report the state of the art from literature. We present the different forms of the graphitic carbon materials which includes graphite, graphene, single, double and multiwall carbon nanotubes. We explain the physical and electronic structure of single wall carbon nanotubes which can be helpful in understanding double wall and multiwall carbon nanotubes. The overview of double and multiwall carbon nanotubes are also presented. At the end we present the carbon nanotubes applications in different areas to emphasize the importance of carbon nanotubes.

In the second part we present the Raman spectroscopy theory. We explain the Raman spectra of different graphitic forms. We explain the Raman bands associated with graphite, graphene, single wall, double wall and multiwall carbon nanotubes.

In the third part, we report about the photoexcitation of carbon nanotubes. We have observed that increasing the laser power could strongly increase the intensity. At the same time, we are interested in the peak modifications of the D and G bands (frequency and broadening). With high photoexcitation, the heating of the tube is such that antiStokes spectra can be acquired. We have consequently roughly compared the shift of the G band and the temperature deduced from the Stoke-antiStokes ratio. Our findings show that thermalization using liquid bath is very efficient. Due to low vaporization temperature of alcohol, the sample is stable under laser beam only with low laser power. In this case, the D and G band shifts identically when the temperature of the thermostat is modified. Under photoexcitation, several effects have been observed. The integrated intensity doesn't vary linearly with the excitation laser power. This non linear effect is of practical importance, as usually, the laser power is increased up to a value which gives signal. It means that low laser power should be used and to be not too far from equilibrium. The D band, which is double resonant, behaves differently than G band. Two explanations can be proposed to explain the shift variation. First, the most likely explanation is a modification of double resonance conditions. The high photoexcitation modifies the electronic band structure, increasing the q vector involved, modifying the phonon band structure and reducing the phonon energy. Second explanation is that the D and G signal doesn't comes from the same area, as back-scattering of an electron is in the main process of the D band due to a defect or a boundary. Under strong photoexcitation, the temperature of all areas are not homogeneous. Both effects are opposite and a decrease of the frequency versus the temperature change is lower than the G mode. In conclusion, the thermal effect can be determined by thermostatic bath of liquid. Stokes-antiStokes ratio is simply a rough estimation for temperature as several unknown factors intervene in the ratio. The variation of the ratio is better and could be used but a starting point is necessary and at low laser power, the

antiStokes part is very weak.

The fourth part of this thesis is devoted to nitrogen and sulphuric acid doping of carbon nanotubes. Doping is interesting as it can modify the properties of the carbon species. As optical observation remains simple, we have tried to determine what can be extracted from a Raman spectra. One can note that this task is difficult, and few works have been available in the literature. We can expect, in an ideal case from doping, a modification of the electronic band structure and a variation of the electron-phonon coupling. Unfortunately, disorder in the sample is present and strongly affects the Raman spectra. For example, G band upshift is expected with doping and with disorder. The decorrelation of both effects is difficult. In our sample, the defect content is quite high as verified by the large value of the half width at half maximum. The G band position is higher for nitrogen doped MWCNT, as well as for the D band position at 514 nm excitation wavelength. The G band position is lower for nitrogen doped carbon nanofibers at 514 nm while the D band is at 1360 cm^{-1}. Using UV excitation, the D band position is modified due to double resonance process. High D and G band position are associated to high nitrogen contents. As our fitting is based on two Lorentzians, a contribution of C-N at high frequency leading to a D mode upshift can't be excluded. Nevertheless, D and G mode position seems upshifted due to the presence of nitrogen. Sulphuric acid is a strong acid, and CNT contact with protons (or what is sometimes called protonation in literature) lead to a strong shift of the Fermi level in the valence band. This p-doping modify both band position and band intensity. For several samples, we have used sulphuric acid and observed logically a decrease in the intensity of the radial breathing mode associated to the outer tube or an upshift in frequency when the doping is not high enough. The outer tube is in contact with proton and the charge transfer between the two tubes is as small as 10-20%, so the inner tube is not significantly affected. We also observed an upshift of the G band associated to the outer tube due to both hardening of the frequency associated to electron-phonon coupling and a bond contraction due to charge transfer. If the doping is strong, the intensity of the outer tube decreases and could be reduce to zero as the van Hove singularity is depopulated. We have performed high pressure experiment with low, medium and high concentration of sulphuric acid. With high concentration of sulphuric acid, the medium structurization seems to reduce the slope of the frequency versus the pressure, the medium structurization acts as a supplementary shielding of the tube. Nevertheless, a low concentration of nanotubes should be used to increase this effect.

In the last part we include one interesting contribution obtained during my thesis work. For an individual double wall carbon nanotube, we have shown that under electrode but without polarization, the G band shape is very narrow

with half width at half maximum close to 4 cm^{-1}, giving the intrinsic limit. In bundle, the observed broadening is larger, which could be interpreted as heterogeneous broadening. The inner tube has a G mode located at 1580 cm^{-1}, already observed for bundled tubes. Nevertheless, in the present case, the observation and determination doesn't need an external parameter such as high pressure or chemical doping. This result proves that the inner tube is influenced by the outer one as for the single wall carbon nanotube, the observed frequency is always higher. The outer tube is very sensitive to the environment.

In this thesis, we have reported experimental data about carbon nanotubes by Raman spectroscopy. We have paid particular attention to experimental conditions. The literature analysis remains difficult as the knowledge advances quickly with new ideas and old explanations are often in contradiction with actual ones. The time spend on nitrogen doped samples is not well represented by the length of the associated chapter but it has been very formative. A consequent and complementary work on other types of carbon structures is needed to find a clear way to extract quantitative piece of information from the spectra. The results on isolated double wall carbon nanotube between electrodes has been more easy to obtain as we have used at the first time an excitation wavelength in resonance with both tubes. These experimental data are a good conclusion of all works already performed in our group. The idea of doping is very exciting but it's practical use is tricky. Complementary high pressure experiments using dehydrated sulphuric acid are necessary to complete the experimental data reported in this manuscript. Finally, thermal effect using Raman scattering is widely used as it's a local probe. We have analyzed what can be the consequences of a too large laser power.

Conclusion Générale

Les objectifs de cette thèse sont d'étudier le dopage et la photoexcitation des nanotubes de carbone par spectroscopie Raman ainsi que de caractériser un nanotube de carbone double parois individuel et de comparer les résultats avec des nanotubes de carbone double parois en faisceaux. Nous avons rapporté plusieurs résultats sur le dopage et les effets de photoexcitation de nanotubes de carbone en utilisant le processus de diffusion Raman. La spectrométrie Raman a été largement utilisée car le signal Raman observé est caractéristique du nanotube. En plus, le mode de respiration dépend de diamètre et son intensité est directement liée à l'énergie de la transition optique. Par conséquent, nous pouvons analyser les nanotubes de carbone dans l'air sans préparation et observer certaines caractéristiques et parfois même dduire sa chiralité. Grâce au processus de double résonance, le mode D est observable lorsque des défauts (de tous types) sont présents. Sa dépendance en fonction de la longueur d'onde d'excitation est d'environ 50 cm^{-1}/eV pour le graphite et est près de 0 pour un carbone très défectueux. Dans le premier cas, il correspond à la sélection d'un phonon particulier dans la zone de Brillouin. Dans le cas du carbone désordonné, il correspond à la respiration d'un anneau hexagonal. Pour le bande G, son interprétation n'est pas simple et un calcul ab-initio peut aider à cet égard. Pour le mode G des nanotubes de carbone mono paroi, deux bandes sont observées, un mode diamètre dependant dit G^{-} à basses fréquences et un autre à proximité de 1592 cm^{-1} étiquetés en tant que G^{+}. Les modes G sont sensibles au dopage, conduisant à la modification de l'intensité et de la position. Le dopage modifie la position du niveau de Fermi, ce qui durcit la fréquence (pour un dopage n ou p), et modifie également le paramètre de maille qui réduit (dopage p) ou augmente (dopage n) la fréquence. Pour les nanotubes de carbone à double parois et les nanotubes de carbone multi-parois, les tubes intérieurs donnent une fréquence correspondant à la valeur du graphite. Le tube extérieur donne un signal similaire à celui d'un nanotube de carbone à

mono paroi. En plus, une contribution D', en raison de défauts d'empilement selon l'axe C près de 1620 cm^{-1}, est présente.

Dans la première partie, nous présentons l'état de l'art de la littérature sur les différentes formes des matériaux carbone graphitique qui comprend le graphite, le graphène, les nanotubes de carbone mono, double et multi parois. Les nanotubes de carbone double et multi paroi sont l'assemblage concentrique de deux et plus de deux tubes de mono paroi. Nous expliquons la structure physique et électronique de nanotubes de carbone mono paroi qui peut être utile dans la compréhension des nanotubes de carbone double et multi paroi . La vue d'ensemble de nanotubes de carbone double et multi paroi sont également présentés. Après cela, nous expliquer les différentes méthodes de synthèse des nanotubes de carbone. A la fin, nous présentons les applications de nanotubes de carbone dans diffrents domaines.

Dans la deuxième partie, nous présentons la théorie de la spectroscopie Raman. Nous expliquons les spectres Raman des différentes formes de carbone sp^2. Nous expliquons les bandes Raman associée avec le graphite, le graphène, nanotubes de carbone mono paroi, double et multi parois.

Dans la troisième partie, nous présentons la photoexcitation des nanotubes de carbone. Nous avons observé que l'augmentation de la puissance du laser pouvait fortement augmenter l'intensité. Dans le même temps, nous nous intéressons à aux modifications de la bande D et G (fréquence et élargissement). Avec une photoexcitation élevée, le chauffage du tube est telle que les spectres anti-Stokes peut être acquis. Nous avons donc comparé approximativement le déplacement de la bande G et la température déduite du rapport Stokes-Anti-Stokes. Nos résultats montrent que la thermalisation dans un bain liquide est très efficace. En raison de la faible température de vaporisation de l'alcool, l'échantillon est stable sous laser uniquement avec une puissance laser faible. Dans ce cas, la bande D et G se déplacent à l'identique lorsque la température du thermostat est modifiée. En fonction de la photoexcitation, plusieurs effets ont été observés. L'intensité intégrée ne varie pas linéairement avec la puissance du laser d'excitation. Cet effet non linéaire est d'une importance pratique car d'habitude, la puissance du laser est augmentée jusqu'à une valeur qui donne du signal. Cela signifie qu'une puissance laser faible doit être utilisée pour ne pas être trop loin de l'équilibre. La bande D, qui est double résonnante, se comporte différent de la bande G. Deux explications peuvent être proposées. Premièrement, le signal D et G ne viennent pas de la même région. Une rétro-diffusion d'un électron intervient dans le processus principal donnant la bande D, une rétro-diffusion due à un défaut ou une frontière. Sous photo-excitation forte, la température de toutes les zones ne seraient pas homogènes. La seconde explication, qui est physiquement plus acceptable, est une modification des con-

ditions de double résonance. La photoexcitation élevée modifie la structure de bandes électroniques, augmentant ainsi le vecteur q impliqué, en modifiant la structure de bande des phonons et en réduisant l'énergie des phonons. Les deux effets sont opposés et la diminution de la fréquence par rapport à la variation de température est inférieure à celle du mode G. En conclusion, l'effet thermique peut être déterminé par thermalisation dans un bain de liquide. Le rapport Stokes Anti-Stokes est tout simplement une estimation de la température car plusieurs facteurs inconnus interviennent dans le rapport. La variation du rapport est meilleure et pourrait être utilisée, mais un point de départ est nécessaire et ce, à une puissance laser faible : la partie anti-Stokes est alors très faible.

La quatriéme partie de cette thèse est consacrée au dopage à l'azote et à l'acide sulfurique des nanotubes de carbone. Le dopage est intéressant car il peut modifier les propriétés électroniques des nanotubes de carbone. Comme l'observation optique reste simple, nous avons essayé de déterminer ce qui peut être extrait d'un spectre Raman. On peut noter que cette tâche est difficile, et peu de travaux se trouvent dans la littérature. Nous pouvons espérer, dans un cas idéal d'un dopage, une modification de la structure de bande électronique et une variation du couplage électron-phonon. Malheureusement, le désordre de l'échantillon présent influence fortement les spectres Raman. Par exemple, une augmentation de bande G est prévue avec le dopage et avec le désordre : la décorrélation de ces deux effets est difficile. Dans notre échantillon, la teneur en défauts est assez élevée attestée par la forte valeur de la demi-largeur à mi-hauteur. La position de la bande G est plus élevé pour les nanotubes de carbone dopés à l'azote, ainsi que pour la position de la bande D à une longueur d'onde d'excitation de 514 nm. La position de la bande G est plus basse pour les nanofibres de carbone dopés azote à 514 nm alors que la bande D est situé à 1360 cm^{-1}. En utilisant une excitation UV, la position de la bande D est modifiée du fait du processus de double résonance. Les positions élevée de la bande D et G sont associées au dopage en azote. Comme notre ajustement est basé sur deux Lorentziennes, une contribution C-N à hautes fréquences conduisant à une augmentation du mode D ne peut être exclue. Néanmoins, les bandes D et G semblent être à une fréquence élevée à cause de la présence d'azote. L'acide sulfurique est un acide fort, et le contact du nanotube avec des protons (ou ce qu'on appelle parfois protonation dans la littérature) conduit à un fort déplacement du niveau de Fermi dans la bande de valence. Ce dopage p modifie la position et l'intensité de la bande G. Pour plusieurs échantillons, nous avons utilisé de l'acide sulfurique et observé logiquement une diminution de l'intensité du mode de respiration associé au tube externe et à une augmentation de la fréquence lorsque le dopage n'est pas assez élevé. Le tube extérieur est en contact avec les protons ; le transfert de charge entre les deux tubes est faible, 10-20%; donc le tube intérieur n'est pas significativement affecté. Nous avons

également observé un déplacement de la bande G associée au tube externe à cause à la fois du durcissement de la fréquence associée au couplage électron-phonon et de la contraction de la liaison en raison du transfert de charge. Si le dopage est fort, l'intensité de la bande G baisse pour le tube extérieur et pourrait être nulle si la singularité de van Hove est dépeuplée. Nous avons réalisé les expériences de haute pression à faible, moyenne et forte concentration d'acide sulfurique. Avec une forte concentration d'acide sulfurique, la structuration du milieu semble réduire la pente de la fréquence en fonction de la pression, la structuration du milieu agit comme un protection supplémentaire du tube. Néanmoins, une faible concentration de nanotubes devraient tre utilisés pour augmenter cet effet. Pour les nanotubes de carbone à double parois, synthétisés par l'intermédiaire des Peapods, les amas et les diamètres sont différents et par conséquent, le mouillage des tubes est différent. Ces expériences m'ont permis d'apprendre à manipuler la haute pression hydrostatique.

Dans la dernier parties, nous présentons une très intéressante contribution obtenue au cours de mon travail de thèse. Pour un nanotube de carbone à double parois individuel, nous avons montré qu'entre électrodes mais sans polarisation, la forme de la bande G est très étroite avec une demi-largeur à mi-hauteur de 4 cm^{-1}, ce qui en donne la limite intrinsèque. En amas, un plus grand élargissement est observé, ce qui pourrait être interprété comme un élargissement hétérogène. Le tube intérieur a un mode G situé à 1580 cm^{-1}, déjà observé pour les tubes en amas. Néanmoins, dans le cas présent, l'observation et la détermination n'a pas besoin d'un paramètre externe comme la haute pression hydrostatique ou le dopage chimique. Ce résultat prouve que le tube intérieur est influencée par le tube externe, dont la fréquence observée est toujours plus élevée. Le tube extérieur est très sensible à l'environnement.

Dans cette thèse, nous avons rapporté des données expérimentales sur les nanotubes de carbone et de nanofibres de carbone par spectroscopie Raman. Nous avons accordé une attention particulière aux conditions expérimentales. L'analyse de la littérature reste difficile en raison des progrès rapides des connaissances avec de nouvelles idées et les explications anciennes sont souvent en contradiction avec les nouvelles. Le temps passé sur les échantillons dopés à l'azote n'est pas bien représenté par la longueur du demi-chapitre associé, mais il a été très formateur. Un travail conséquent et complémentaire sur d'autres types de structures de carbone est nécessaire pour trouver une façon claire d'extraire de l'information quantitative des spectres. Les résultats sur le nanotube de carbone bi-parois isolé entre les électrodes a été plus facile à obtenir car nous avons utilisé, la première fois, une longueur d'onde d'excitation en résonance avec les deux tubes. Ces données expérimentales sont une bonne conclusion de tous les travaux déjà réalisés dans notre groupe. L'idée du dopage est très séduisante, mais son utilisation pratique est délicate. Des expériences

complémentaires à haute pression à l'aide d'acide sulfurique déshydraté sont nécessaires pour compléter les données expérimentales rapportées dans ce manuscrit. Enfin, la mesure de température en utilisant la diffusion Raman est largement utilisée car c'est une sonde locale. Nous avons analysé ce que peuvent être les conséquences d'utiliser un laser avec une puissance trop importante.

Nitrogen doped and undoped samples: TEM micrographs, XPS and EA

Transmission electron microscopy, X-ray photoelectron spectroscopy and elemental analysis results are provided by Jacques Teddy(ENSIACET, Toulouse)in the group of Prof. Philippe Serp [1]. Undoped MWCNT were synthesized on the freshly prepared MO-CVD 4% w/w Fe_2O_3/Al_2O_3 catalyst at a deposition temperature 700 ^{0}C with the hyperion condition, 200 sccm C_2H_4, 100 sccm H_2, $t_{Reaction} = 30$ min and $m_{catalyst}$ is 0.5 gram [1]. The external average diameter by the external diameter distribution is calculated as ($D_{average}$) 6.5 nm. Temperature of oxidation is 636 ^{0}C determined by thermogravimetric analysis(TGA).

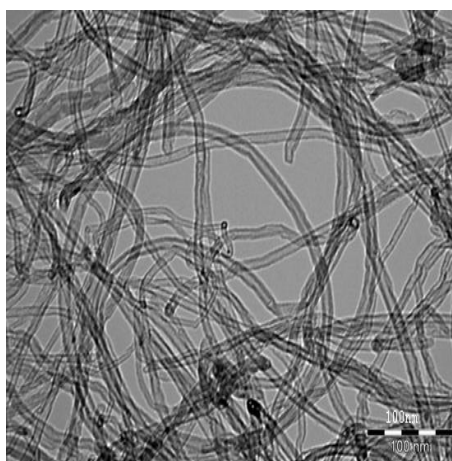**Figure A.1:** *TEM micrograph of the MWCNT. Pure MWCNT were synthesized on the freshly prepared MO-CVD 4% w/w Fe_2O_3/Al_2O_3 catalyst at a deposition temperature 700 ^0C with the hyperion condition, 200 sccm C_2H_4, 100 sccm H_2, $t_{Reaction} = 30$ min and $m_{catalyst}$ is 0.5 gram [1].*

According to elemental analysis(EA) C is 95% and N is 0%. Nitrogen doped MWCNT were synthesized by 2% w/w cobalt catalyst (Co/SiO$_2$) calcined supported on silica at a deposition temperature 700 ^{0}C.
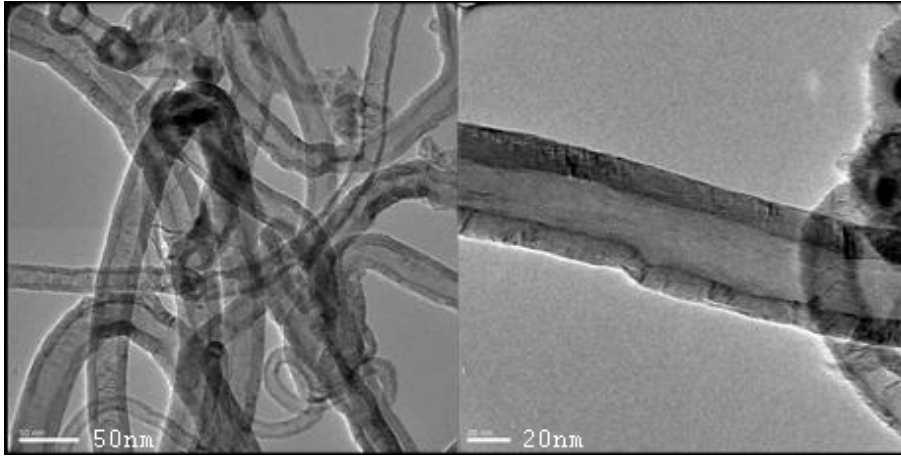

Figure A.2: *TEM micrograph of the N doped MWCNT. Nitrogen doped MWCNT were synthesized by 2% w/w cobalt catalyst (Co/SiO$_2$)calcined supported on silica at a deposition temperature 700 ^{0}C. Acetonitrile (CH$_3$CN) precursor was used under 120 sccm H$_2$ and 160 sccm N$_2$ [1].*

Acetonitrile (CH$_3$CN) precursor was used under 120 sccm H$_2$ and 160 sccm N$_2$. The average external diameter (D$_{average}$) of nitrogen doped carbon nanotubes is 24 nm and the distribution is large, ranging from 8 to 45 nm. The nitrogen doped in MWCNT by XPS and elemental analysis (E.A.) is 0.6% and 1.6%, respectively. Temperature of oxidation is 460 ^{0}C by TGA analysis.

Table A.1: *TEM analysis, XPS and elemental analysis of N doped CNF synthesized with Pyridine precursor [1]*

Sample	T$_{dep}$ (^{0}C)	T$_{ox}$ (^{0}C)	D$_{av}$ (nm)	XPS C (%)	N (%)	Elemental Analysis C (%)	N (%)	C/N
P3	600	530	8.8	100	0	85.6	0.6	142
P2	650	565	10	100	0	90.9	1.3	70
P1	750	575	9.6	100	0	92.5	1.5	61.6

Pure carbon nanofibres (CNF) were synthesized with Ni/Al$_2$O$_3$ catalyst MO-CVD at a deposition temperature 700 ^{0}C under the following conditions, 105 sccm C$_2$H$_4$, 160 sccm N$_2$, 120 sccm H$_2$, and m$_{catalyst}$ is 4 gram [1]. The external average diameter by the external diameter distribution is calculated as (D$_{average}$) 7.8 nm. Temperature of oxidation is 609 ^{0}C by TGA analysis. According to elemental analysis(EA) C is 91% and N is 0.02%.

Nitrogen doped CNF with pyridine precursor were grown over a 2.5% w/w Fe/Al$_2$O$_3$ catalyst under H$_2$ = 120 sccm and N$_2$ = 160 sccm. TEM micrographs revealed that the fibers were bamboo-like structure independent of the deposition temperatures. The diameter distribution calculated from the TEM micrographs is between 8.8 and 10 nm. TEM analysis, XPS and elemental analysis values of N doped CNF (Pyridine precursor) are shown in table A.1.

Nitrogen doped CNF with acetonitrile precursor were grown from pyridine over a 2.5% w/w FeAl$_2$O$_3$ catalyst under H$_2$ = 120 sccm and N$_2$ = 160 sccm. TEM micrographs show that the fibers were bamboo-like structure independent of the deposition temperatures. The diameter distribution from the TEM micrographs is between 7.7 nm and 19.5 nm.

Table A.2: *TEM analysis, XPS and elemental analysis values of N doped CNF (Acetonitrile precursor) [1]*

Sample	T$_{dep}$ (^{0}C)	T$_{ox}$ (^{0}C)	D$_{av}$(nm) (nm)	%C (%)	XPS %N (%)	C/N	Elemental Analysis %C (%)	%N (%)	C/N
A1	600	483	7.7	97.4	2.6	37.46	79.8	3.6	22.16
A2	650	487	19.5	98.3	1.7	57.82	80.4	7.1	11.32
A3	700	487	14.6	96.2	3.8	25.31	78.4	6.4	12.25
A4	750	503	15.3	96.8	3.2	30.25	80.9	5.9	13.71

The nitrogen determined by XPS (surface analysis technique) is much lower than that of the EA(global analysis technique). The depth of the XPS beam was less than 8 nm. This can be the reason why value of nitrogen percentage is less by XPS as compare to AE. This indicates that the doping is not limited to the surface of the fibers but to all the walls of the tubular structure. TEM analysis, XPS and EA values of N doped CNF (Acetonitrile precursor) are shown in table A.2.

The amount of nitrogen doping, in both acetonitrile and pyridine cases increases by increasing the temperature from 600 ^{0}C to 650 ^{0}C, but after that starts decreasing in the case of acetonitrile and tends to remain constant in the case of pyridine precursor [1]. This may be due to the thermodynamic stability of metal carbides over metal nitrides, because at higher temperatures, carbides being supported over nitrides [2]. Doped carbon nanostructures are less stable as compare to undoped nanostructures and oxidize at lower temperatures [3]. The nitrogen percentage in CNF synthesized with pyridine precursor is very low as compare to nitrogen percentage in CNF synthesized with acetonitrile precursor as shown by XPS and AE.

The oxidation temperatures of N doped CNF (pyridine precursor) 565 ^{0}C is

higher than N doped CNF (acetonitrile precursor) 487 ^{0}C [1]. This suggest the higher nitrogen concentration in the case of N doped CNF (acetonitrile precursor). This leads that acetonitrile may be a better precursor for nitrogen doping in CNT and CNF as compare to pyridine. Four different types of nitrogen bonding observed in CNF synthesized from acetonitrile precursor. These are N_p (pyridinic), N_{PYR} (pyrrolic), N_Q (quaternary) and N_{ox} (oxidized pyridinic). In nitrogen doped CNF synthesized from acetonitrile precursor, pyridinic N_p type dominates at 600 ^{0}C, pyrrolic N_{PYR} dominates at 650 ^{0}C and quaternary N_Q type at 700 ^{0}C. This agree with the findings of Bitter et al [4], who observed that the increase in temperature supports the quaternary nitrogen groups then the pyridinic nitrogen groups. Considering the toxicity of pyridine and low doping of nitrogen in CNF synthesized with pyridine, the option of using pyridine as a precursor for nitrogen doping can be excluded. Types of nitrogen species and their percentage amount present in CNF doped with acetonitrile precursor at different temperatures are shown in table A.3.

Table A.3: *Nitrogen type and % amount at different deposition temperatures in N doped CNF(Acetonitrile) [1]*

Sample	T ^{0}C	%N_p	%N_{Pyr}	%N_Q	%N_{Ox}	Dominant species
A1	600	77	0	15.6	7.4	Pyridinic
A2	650	28.8	31.3	12.3	27.6	Pyrrolic
A3	700	34.7	0	53.1	12.1	Quaternary
A4	750	24.8	34.8	19.2	21.1	Pyrollic

Bibliography

[1] J. Teddy, Ph.D. thesis, Institut National Polytechnique De Toulouse, Toulouse, 2009.

[2] S. van Dommele, K. P. de Jong, and J. H. Bitter, Tuning the activity of nitrogen-containing carbon nanotubes by controlled nitrogen incorporation, North American Catalysis Society (NACS) - 20th North American Meeting (NAM), 2007.

[3] S. R. Stoyanov, A. V. Titov, and P. Král, Coordination Chemistry Reviews **253**, 2852 (2009).

[4] S. van Dommele, K. P. de Jong, and J. H. Bitter, Chemical Communication 4859 (2006).